5-2023

DEVELOPMENT OF A LOW-DOSE RADIATION THERAPY DEVICE FOR ACUTE RESPIRATORY DISTRESS SYNDROME

Thomas Heath Davis
University of Tennessee, Knoxville, tdavi107@vols.utk.edu

To the Graduate Council:

I am submitting herewith a dissertation written by Thomas Heath Davis entitled "DEVELOPMENT OF A LOW-DOSE RADIATION THERAPY DEVICE FOR ACUTE RESPIRATORY DISTRESS SYNDROME." I have examined the final electronic copy of this dissertation for form and content and recommend that it be accepted in partial fulfillment of the requirements for the degree of Doctor of Philosophy, with a major in Nuclear Engineering.

Eric Lukosi, Major Professor

We have read this dissertation and recommend its acceptance:

Michael Howard, Lawrence H. Heilbronn, Dustin Osborne, Eric D. Lukosi

Accepted for the Council:

Dixie L. Thompson

Vice Provost and Dean of the Graduate School

(Original signatures are on file with official student records.)

DEVELOPMENT OF A LOW-DOSE RADIATION THERAPY DEVICE FOR ACUTE RESPIRATORY DISTRESS SYNDROME

A Dissertation Presented for the

Doctor of Philosophy

Degree

The University of Tennessee, Knoxville

Thomas Heath Davis

May 2023

ACKNOWLEDGEMENTS

Thank you to Dr. Eric Lukosi for his mentorship. He became my undergraduate research advisor in 2018, and without his guidance, a Ph.D. in Nuclear Engineering would have been an unthinkable achievement. For nearly five years, he has offered insight into not only research but life as well.

Dr. Michael Howard is the head of the medical physics department and a practicing medical physicist. Throughout my time at UT, he has offered career advice and insight into the medical physics profession. I want to thank him for taking the time to help me with experimentation and providing resources I would have otherwise not had access to at the university level. Thank you to my other committee members, Dr. Lawrence Heilbronn and Dr. Dustin Osborne, for their insights throughout this project.

Dr. Michael Liesenfelt has been another valuable mentor in undergraduate and graduate research. His mentorship greatly influenced my decision to pursue a Ph.D. in nuclear engineering. His insight and experience in modeling techniques were valuable in guiding much of this work. Without his help, this project would not have been possible.

Thank you to Brett Miller for his insight and advice about Medical Physics. I would also like to thank my family, Pam, and Sarah Ellen, for their support over the last few years of study. Finally, I thank my fellow graduate students, Jake and Corey, for their friendship and problem-solving skills.

PREFACE

This work is a continuation of my Master's Thesis titled Development of a Low-dose Radiation Therapy Device for Acute Respiratory Distress Syndrome. The first three chapters of this dissertation are from that document with some minor changes and additions.

ABSTRACT

This research focuses on developing a low-dose radiotherapy (LD-RT) device for treating acute respiratory distress syndrome (ARDS). This respiratory illness affects millions of people a year. Using orthovoltage (200 – 500 keV) X-ray energy provides many advantages over traditional radiotherapy delivery with linear accelerators, such as low cost and greater accessibility. In addition, X-ray tubes have been shown throughout history to provide good treatment outcomes for pneumonia, and research has shown LD-RT to be just as effective with ARDS. This proposal summarizes my efforts in determining the dosimetric properties of an LD-RT system to deliver treatment quickly and effectively. My research involves Monte Carlo transport simulations in MCNP to calculate a whole lung treatment's dose delivery and coverage. In addition, different setup geometries and beam modifications, such as filtration, are explored to optimize the treatment delivery. The development of such a system would greatly expand the treatment options for ARDS-type illness at a lower cost and greater accessibility than current radiotherapy options.

TABLE OF CONTENTS

LIST OF TABLES

LIST OF FIGURES

CHAPTER ONE
INTRODUCTION

1.1 Radiation Therapy in Medicine

Radiation therapy (RT) has been used for over a century to treat diseases using radioactive sources, X-ray generation tubes, and particle accelerators. While treatment methods have evolved with technology, the fundamental goal is to deliver energy through radiation to induce a biological effect. This effect has made radiotherapy a valuable tool, especially in oncology, for tumor control. Today, an estimated two-thirds of all cancer patients receive RT as part of treatment [1]. Recently, the use of RT outside of oncology has regained the medical community's attention. Studies early in the 20th century saw good results in treating pneumonia and other respiratory illnesses, warranting a modern approach for low-dose RT to treat disease [2-5]. This section discusses the technological developments and clinical procedures that have shaped radiotherapy over the past century.

The discovery of X-rays by Wilhelm Rontgen in 1895 marks the beginning of scientific research in RT [6]. Scientists quickly discovered that prolonged exposure created inflammation, redness, and tissue damage on the skin. Before understanding these biological effects caused by radiation, the first X-ray treatments were carried out on patients within a year, mainly for tumor control [7]. Around the same time, Marie and Pierre Curie started their research on natural radiation sources, leading to the emergence of brachytherapy with radium and other natural radioactive sources [8]. This discovery allowed for more diverse treatment options due to these isotopes' higher energy and intensity. Early Crookes cold cathode design X-ray tubes were limited in energy (<100 keV) and output, resulting in limited tissue penetration and energy deposition rate. While the therapeutic applications of X-rays were immediately recognized, their utility was initially limited to superficial skin cancers [1].

In 1905, reports from Musser and Edsall saw the potential for X-rays in low doses to treat pneumonia in a small study with five patients [9]. In their conclusion, they stated

that further research was needed to understand RT's effects properly. Almost ten years later, a separate group of researchers, Quimby and Quimby, successfully treated 12 cases of pneumonia with similar findings [10]. As was the case with Musser and Edsall, further research was warranted.

The introduction of orthovoltage (100 – 500 keV) and Coolidge (hot cathode) X-ray tubes in the 1920s allowed a wider variety of treatments due to the increased penetration depth and higher X-ray output [11]. Around the same time (1924), Heidenhain and Fried released a more extensive study on pneumonia treatment with X-rays with more detailed findings. They showed that low doses of X-rays reduce inflammation of all types regardless of their location in the body. Further, this proved the clinical utility of treating deeper penetrating infections, such as pneumonia [12]. This study is considered the beginning of low-dose radiotherapy (LD-RT) for pulmonary-type diseases, and many more pneumonia studies occurred in the following years. The authors McIntire and Smith, Scott, Solis-Cohen and Levine, Settle, Rousseau, et al., and many others had shown similar good outcomes for patients suffering from unresolved pneumonia between 1924 and 1937 [13]. With the arrival of penicillin outperforming almost all other treatments, LD-RT research lost popularity. The use of LD-RT as a treatment option for pneumonia would never achieve broad support or scientific standing and led to the use of LD-RT treatment for pneumonia all but disappearing from scientific studies in the early 1940s [13].

1.1.1 RT in the Megavoltage era (1940 - Present Day)

Many discoveries before 1940 are the foundation for what would be considered high-dose RT used in oncology today. Hermann Joseph Muller's 1927 paper first recognized increased cancer risk and other genetic effects of radiation exposure [14]. This discovery coincided with the work of Henri Coutard, a French radiologist, who first demonstrated in 1922 that X-ray doses that would be intolerable for a single treatment, when spread over multiple days, did not affect subcutaneous tissues [15]. This work led to a fractionated treatment process whereby the dose is divided into many smaller "fractions"

to promote healthy cell repopulation. The medical community adopted this method worldwide in 1935, and it is still the basis for most radiation therapy planning today.

By the end of the 1930s, technological advancements allowed X-ray tubes to produce energy in the MeV range, increasing the depth and uniformity of treatment and marking the beginning of the megavoltage era of RT [1]. These efforts of continually improving acceleration potential led to the research and development of other accelerator devices, such as the Van de Graaff generator. This device is an electrostatic generator initially developed for particle physics. It is capable of accelerating electrons in the 1-2 MeV range. The Van de Graaff generator was first installed for medical treatment in 1937 at Huntington Memorial Hospital in Boston [16]. Another accelerator device adopted from the physics community was the betatron which accelerated electrons to MeV energies by injecting them into a doughnut-shaped tube and using alternating magnetic fields to accelerate. These early betatrons could have electron acceleration potentials up to 50 MeV [17].

With the development of the nuclear reactor in the early 1940s, a new method of delivering higher energy radiation therapy was now possible due to Cobalt-60 and other isotopes. With X-ray tubes, Van de Graaff generators, and later linear accelerators (linacs), electrons are accelerated into a dense metal target to make X-rays. Unlike the other devices, betatrons are primarily used for direct beta (electron) treatment, not X-ray production. With isotopes, gamma rays, which are photons just like X-rays, come from the radioactive decay of the nucleus. The isotope Co-60 has a 1.17 and 1.33 MeV gamma ray, perfect for deep penetration. These gamma rays are used in high-energy RT by collimating large amounts of this isotope in a device. In 1948, the Atomic Energy Commission licensed the first cobalt therapy device, nicknamed the “cobalt bomb,” to Dr. Harold E. Johns, who would complete the first treatment in 1951 [18].

Another advancement during World War II was the invention of high-frequency, high-power microwave generators for radar systems. With the addition of a waveguide, this RF power is directed into this guide to accelerate electrons to high kinetic energies. Thus the first linear accelerator or linac was developed with the ability to create X-rays from 2 to 25 MeV, with the first medical linac installed in 1953 at Christie Hospital in

Manchester, United Kingdom. Later developments of the linac allowed for using electrons and X-rays at different energies from the same machine [19]. For these reasons, by the 1970s, the medical linac had become the workhorse of radiotherapy, offering a range of treatment energies from 2 MeV to 25 MeV.

The steady increase of treatment energy, well into the MeV range, after the 1940s presented many challenges, especially when it came to targeting structures and calculating the dose to a patient. This changed with the introduction of the CT scanner in the early 1970s [20]. Before this, treatment plans were calculated to single points in the body using physical measurements of the patient with a combination of radiographs to locate the treatment points. In the late ’60s, early computer programs calculated these 2D treatment plans, but with the CT scan, 3D visualization of the body and organs of interest was finally possible [21]. These treatment plans allowed for better patient alignment and dose optimization, but most importantly, the precise visualization of target structures and normal tissues in the patient to deliver high-dose rate therapy (HD-RT).

1.2 LD-RT Delivery for ARDS

Recently, the use of LD-RT for treating respiratory diseases became more attractive to healthcare providers worldwide due to the onset of the SARS-CoV-2, commonly referred to as the COVID-19 pandemic. Acute respiratory distress syndrome (ARDS) is a pulmonary condition that results in low blood oxygen levels in the affected patient. These symptoms are brought on by many factors, such as bacterial/viral infections, trauma, sepsis, and drug overdose. However, bacterial and viral pneumonia are the most common causes [5, 22]. Acute inflammation of the lungs results in low blood oxygen levels, and the influx of cytokines and other inflammatory compounds exacerbates this inflammation. This response can lead to multiple organ dysfunction syndromes with long-term physical and psychological effects. A 2016 study across 50 countries identified that 10.4% of ICU patients met ARDS criteria, and among the severe cases, the mortality rate was 46% [23]. These studies indicate that an alternative, generalized treatment of ARDS would benefit the medical community.

With COVID-19, the danger of ARDS-type illness received worldwide attention, with many treatment modalities investigated to suppress ARDS symptoms. The most severe complications leaned heavily towards those of advanced age and those with comorbidities [24]. Early in the pandemic, emergency use authorizations in the USA approved treatments with remdesivir and dexamethasone. However, World Health Organization Solidarity Trial negated the benefits of many commonly used anti-viral regimens. The initial lack of efficacy for drug-based treatments was akin to the pre-antibiotic days of the early 20th century. Many researchers looked at the historical treatment of bacterial/viral pneumonia with LD-RT, as discussed previously [13, 25].

Multiple groups have shown the efficacy of LD-RT for treating COVID-19-induced ARDS. One such group demonstrated that an acute X-ray dose of 150 centi-gray (cGy) to the bilateral lungs markedly improved the condition of four of the five patients treated, even with advanced age (median age 90). They noted that low-dose whole-lung radiation led to rapid improvement without acute toxicity [2, 3]. Data from Tehran indicated similar results with patients receiving 0.5 Gy whole lung irradiation resulting in an 80% recovery rate with no acute toxicity [26]. A study from Madrid also noted good results, with seven of the nine patients being discharged [27].

These studies have demonstrated that LD-RT has an anti-inflammatory effect by altering the function of various inflammatory cells. Cytokine Release Syndrome (CRS) or "cytokine storm" is the rapid increase of pro-inflammatory cytokines, and in COVID-19, macrophages are an essential component of this immune system response [4]. The release of macrophages promotes recovery by fighting infection and stimulating other immune cells. With CRS, the sudden influx of macrophages can overwhelm the lungs with inflammation caused specifically by the M1-like phenotype, a pro-inflammatory macrophage. One reported mechanism suggests that LD-RT polarizes macrophages towards M2-like anti-inflammatory phenotypes [4, 25]. Adjusting the ratio of pro-inflammatory M1-like phenotypes towards the anti-inflammatory M2-like phenotypes can improve this auto-immune response. Clinical data suggest that a whole lung dose of 0.3 – 1.5 Gy can induce the desired effect in limiting the cytokine storm and neutralizing inflammatory factors in CRS. These proposed mechanisms involving the modification of

cytokines, the historical treatment of pneumonia, and preclinical mouse studies all suggest that LD-RT is a viable, general treatment for ARDS-type illness [28].

In all the studies of LD-RT for ARDS treatment, medical linear accelerators (linacs) were used for treatment delivery [2-4, 22, 25]. Today, they are the most common RT device found in nearly every radiation oncology department in the country [29]. While they can deliver precise whole-lung LD-RT for ARDS promptly, their large-scale adoption of this treatment has some logistical and financial drawbacks.

In nearly all cases, ARDS patients are first admitted to the intensive care unit (ICU). If immediate treatment is necessary, these patients would be transferred to the radiation oncology department, where they would likely need a CT scan for planning before treatment. Moving patients to the radiation oncology department is a rare but expected process today when patients receive palliative treatment with little to no notice. However, if general LD-RT were to become more common, the increased workload could strain the RT department. The influx of patients would exacerbate this issue if the department operated at maximum capacity. With severe cases of ARDS, LD-RT may be needed immediately, before the worsening of the cytokine storm [25]. LD-RT may be required during nighttime and weekends when most RT departments are typically not staffed.

Adding another linac could meet this increased demand; however, linacs are extremely expensive (millions of dollars). Due to their high X-ray energies, they require radiation vaults with many feet of concrete for shielding the staff and public. Shielding increases the associated costs and puts a logistical strain on hospitals with limited space. Whole lung LD-RT is also a simple treatment protocol. The upper limit of the dose required for LD-RT is 1.5 Gy, approximately equal to 1 fraction of the typical 40 prescribed for lung cancer [30]. The low-dose and simple setup would not warrant many of the features available with a modern linac, such as intensity-modulated radiation therapy (IMRT), volumetric modulated arc therapy (VMAT), or image-guided radiation therapy (IGRT) [31]. Therefore, the cost of LD-RT using a linac would be financially unjustifiable.

The biggest problem facing linac-based delivery of LD-RT is that most hospitals in the country do not have a radiation oncology department. A 2006 study identified that only 20% of U.S. hospitals have a medical linac [32]. Small rural hospitals do not have the

financial incentive or patient load to necessitate investment in radiation oncology. In this case, patients who could benefit from LD-RT for ARDS treatment would need to be transported to a different hospital which may cause further deterioration of their condition. In the case of the COVID-19 pandemic, patient transport was not an option due to the overfilled status of the hospital system worldwide.

Looking at history, the X-ray tube was more than adequate to deliver LD-RT to treat pneumonia before 1940. While modern medicine has relegated its use to imaging, orthovoltage tubes can produce sufficient energy and fluxes for LD-RT. Because of their simplicity and lower operating potential, they are orders of magnitude cheaper than medical linacs (tens of thousands of dollars). Their much lower beam energy further reduces shielding requirements and associated costs. We propose a modern radiotherapy device using orthovoltage X-ray tube energies to deliver LD-RT for ARDS. This system would benefit from greater hospital availability for treatment, regardless of a radiation oncology department with traditional RT systems.

1.2.1 LD-RT Risks

One concern about using LD-RT for respiratory illness is the potential for developing cancer later in life. The occurrence of radiation-induced second malignancies (RISM) depends on factors such as lifestyle, treatment modality, and genetic predisposition [33]. How each factor contributes to RISM is challenging to differentiate, but age is a good indicator of the total risk. Children and younger adults are more likely to survive for a more extended period following RT due to their young age; therefore, they have the most significant risk of RISM. The Childhood Cancer Survivor Study has shown that after 30 years, treatment-related mortality attributable to secondary tumor formation does increase [34].

Other epidemiological studies have determined the increased risk of RISM lung cancers following HD-RT treatment of Hodgkin Lymphoma. With a median age of exposure of 49-50 years, the estimated Excess Relative Risk (ERR), defined in Equation 1, per gray, was found to be 0.15 [35].

$$ERR = \frac{R_e}{R_u} - 1 \quad (1)$$

ERR defined as the rate of the radiation-induced disease R_e, divided by the rate of the disease in the unexposed population R_u, minus 1. While this risk is normalized to Gy received during treatment, cumulative doses may reach 15 to 70 Gy, which may not accurately represent the ERR of LD-RT.

Another epidemiological study following the health effects of low-level radiation is the Million Person Study (MPS). It has been underway for the last quarter century following the health effects of radiation workers and veterans [36]. The ERR per 100 mGy for radiogenic lung cancer over 915,543 people is 0.042. This result would indicate that the general population lung cancer rate of 7% would increase to 8.47% following 0.5 Gy LD-RT treatment. The upper bound treatment dose of 1.5 Gy would result in a cancer rate of 11.41% [37].

Both studies suggest that the ERR of lung cancers following the administration of LD-RT is low. The highest single fraction dose of 1.5 Gy would only increase the lung cancer rate from 7% to 11.41%. However, further research on LD-RT for ARDS may suggest that lower clinical doses may achieve the desired effect. An even lower dose that 1.5 Gy would further reduce the ERR of tumor formation from treatment. Evidence from the COVID-19 pandemic indicates that patients of advanced age or with comorbidities often suffered the most severe ARDS symptoms when drug treatment methods failed. As previously suggested, older patients have a lower chance of RISM due to their shorter projected life span; therefore, the benefits of LD-RT may outweigh the small increased risk of long-term cancer formation.

CHAPTER TWO
RADIATION PRODUCTION, TRANSPORT, AND INTERACTION

2.1 Radiation Interactions in the Body

It is important to understand how radiation interacts in the body to determine the effectiveness of a treatment modality. When ionizing or indirectly ionizing radiation interacts with tissue, it delivers energy that can weaken or kill cells. This is defined by the dose unit Gray (Gy) in Equation 2, which represents the energy delivered to a particular mass of tissue or material.

$$D = \frac{Energy\ Depostion}{Mass\ of\ Medium} \tag{2}$$

In this function, the amount of energy delivered is in Joules (J) and is divided by the mass of the medium in kilograms (kg) [38]. If the volume and density of a particular tissue are known, then the mass can be calculated.

The dose delivered from a MeV linac or an orthovoltage X-ray tube is the same if the energy deposited in a given mass is the same. This function provides a convenient method for comparing the treatment performance of different sources since the biological response of cells is related to the amount of dose given. For X-ray sources, dose-response depends on the individual atomic interactions between incoming X-rays and the atoms composing the cell. When an incoming photon interacts in a medium, it deposits energy in one of three main ways depicted in Figure 1.

The first method is through the photoelectric effect process, where incoming photons strike an electron in the shell of an atom. If the photon energy exceeds the electron binding energy, it will be ejected from its orbital shell with the incident photon's energy. In this interaction, the photon is completely absorbed [39]. The photoelectric effect is considered a low-energy phenomenon and is more prevalent with high-Z materials such as metals.

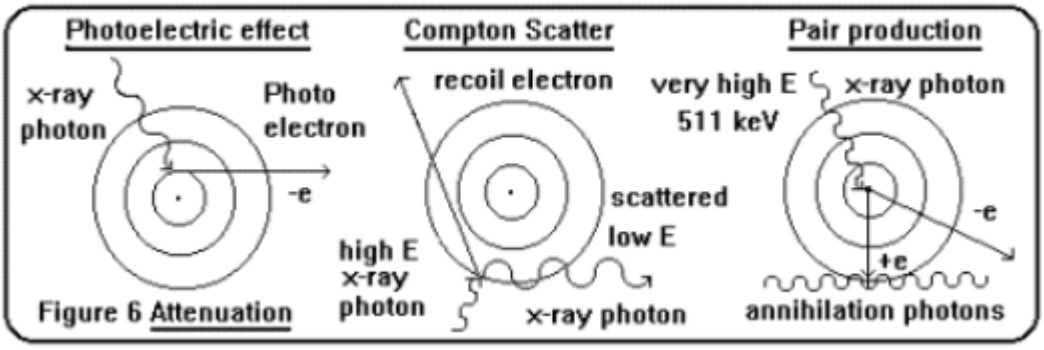

Figure 1. Illustration of the three main modes of photon interactions resulting in energy deposition in the body [40].

The second interaction type is Compton scattering which occurs when the incoming photon is scattered off a free electron in the tissue. The scattered electron energy is a function of the incoming photon energy and the angle at which it is scattered [41]. The energy transferred to the electron is maximum when the angle between the scattered photon and the direction of travel is 180° (scattering directly backward). Compton scattering is the most common interaction with orthovoltage to MeV photon energies.

The last method of interaction is through pair production. This happens when an incoming photon energy has more than two times the rest mass of an electron, 1.022 MeV. The photon is absorbed by the nucleus of an atom, creating an electron/positron pair. The photon's energy is reduced by 1.022 MeV, and when the electron/positron pair annihilate, two 0.511 MeV gamma-rays are produced. This cannot occur below the 1.022 MeV threshold and does not become common inside human tissue until the photon energy reaches the multiple MeV range. At very high photon energies (above 10 MeV), photonuclear interactions are possible where the nucleus absorbs the proton, and a proton or neutron is ejected. However, this reaction is rare and usually ignored.

The photoelectric effect and Compton scattering are the dominant modes by which photons interact in the human body. Both cause an electron to ionize or break out of the orbital shell. If this electron is involved in a bond between two atoms, it will break this bond by ejecting the electron. Secondary effects are caused by the ejected electron striking other bonded electrons and freeing them. This cascade of electron ejections from a primary interaction is called delta electrons and can cause many more bond breaks than the initial interaction. With orthovoltage energies, the range of these secondary electrons is relatively short.

If the break occurs in the DNA strand, this can trigger a wide range of effects. Depending on the cell type and where the break occurs, this can either be repaired or, in other cases, trigger apoptosis, where the cell intentionally dies. Another potential outcome following a DNA break is the reproductive failure of the cell [42]. The radio sensitivity of the cell chiefly determines the likelihood of one outcome versus the other.

Another outcome of radiation exposure is the production of free radicles inside the tissue. The most damaging is the hydroxyl radicle (OH^-) which can break multiple bonds

(especially DNA bonds) over its very short lifetime of 10^{-5} seconds. These are formed by the primary interaction of X-rays or the cascade of secondary delta electrons. Nearly two-thirds of radiation-induced damage from X-rays and gamma-rays are from indirect, free radicle formations [43]. The probability of any of these effects weakening or killing cells increase as the dose increases. They also increase with the energy of the primary X-ray due to the differences in delta electron track structures. High-energy X-rays create many more delta electrons, even with the same dose delivered as low-energy X-rays. However, this is outside the scope of this discussion. In RT, the dose delivered is the driving factor in achieving the desired cellular response.

These interactions strongly affect RT delivery other than determining energy deposited in tissue. As a photon beam passes through tissue, these interactions absorb photons and change their energy through scattering. The mass attenuation coefficient quantifies the combination of these effects as a function of distance in a material [44]. This value relates to how quickly photons are attenuated due to absorption, scattering, etc., as a function of energy and distance. Figure 2 shows that in water, an analogous material to human tissue, the attenuation decreases with energy. This explains why MeV beams increase the uniformity of dose at greater depths. The mass attenuation coefficient is lower, and the penetration of these X-rays is higher, leading to decreased dose drop-off.

The poly-energetic nature of radiation from X-ray tubes and linac sources means that the attenuation of an X-ray beam is a convolution of the X-ray output energy spectrum and the mass attenuation across all energies of that spectrum. Because of the higher attenuation of low-energy photons, the output energy spectrum changes as the X-rays pass through a material. Initially, low-energy X-rays with high attenuation coefficients stop shallower in the material, resulting in higher dose rates closer to the surface. This shifts the average energy of the X-ray spectrum towards higher energy as the X-rays pass through the body. This issue is less pronounced in MeV beams due to the high average spectrum energy and lower attenuation coefficient. This effect must be accounted for in dose calculations with orthovoltage X-ray tubes.

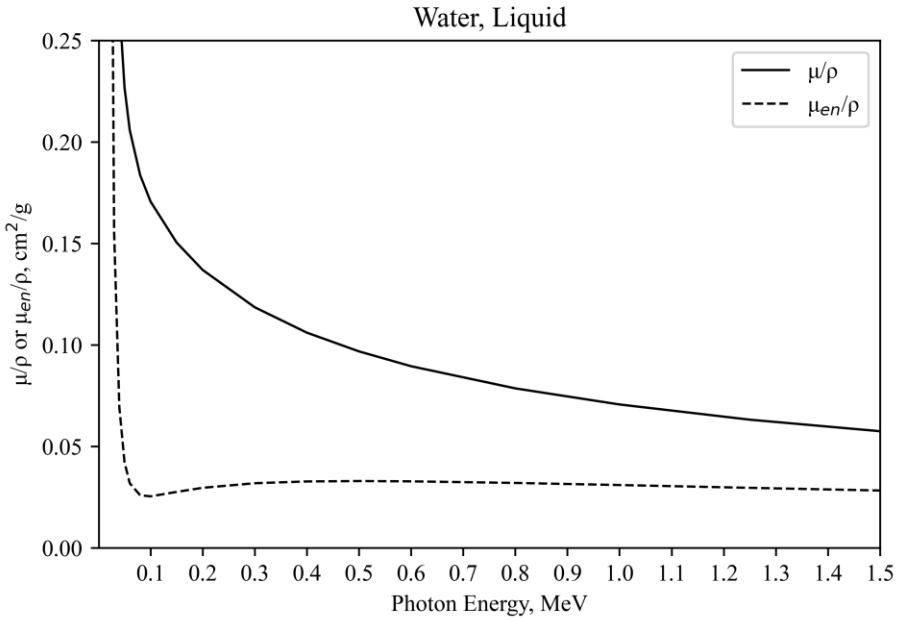

Figure 2. A plot of the mass attenuation and energy attenuation coefficients as a function of photon energy in MeV [45].

While these factors make understanding the X-ray intensity (flux) and energy spectrum through a material challenging, the beam's divergence is another compounding factor. If the area in which X-rays are produced in the target is considered a point source, the total X-ray intensity across all energies decreases proportionally to the distance to this point, squared. These effects determine the photon flux available to deliver energy to tissue at a given depth. Further, the energy of the photons determines the type of interaction they undergo based on the cross-section (photoelectric, Compton scattering, pair production) and how much energy these interactions deposit into the medium.

To accurately determine the dose to the lungs, we must calculate the photon flux, photon energy, and how much energy is deposited through the body. This is complicated, given that each of these variables changes as a function of depth. Further, the human body is comprised of many different tissue types, all with varying probabilities of interaction and densities, which alter how each of these variables changes along each path length.

2.2 Fundamentals of Radiation Production

Since we are interested in delivering LD-RT with an X-ray tube instead of a medical linac, it is important to understand how they produce X-rays. With any medical X-ray-producing device, the principle of operation is largely the same. Electrons are accelerated until they possess very high kinetic energy and are directed into a dense, high-Z material. Inside this material, X-rays are produced through two interaction mechanisms [46]. The first and most common interaction is bremsstrahlung radiation or “braking radiation.” Bremsstrahlung arises from the acceleration or deceleration of a free electron in the field of a nucleus. The loss of kinetic energy by the free electron is in the form of electromagnetic radiation, i.e., photons, thus satisfying the law of conservation of energy [47]. High-Z materials are chosen because bremsstrahlung yield is proportional to the material's atomic number, as described by Equation 3.

$$Y \sim ZT^2 \tag{3}$$

In this equation, Y is the relative radiation yield, T is the kinetic energy of the incoming free electron, and Z is the atomic number of the target material. It is common for the target in any X-ray-producing machine to be a heavy, dense metal such as tungsten or a similar alloy. This increases the proportion of X-rays produced for a given number of incoming free electrons. The kinetic energy, T, of the electron is determined by the accelerator design and the amount of energy the device can transfer to the electrons. The maximum output X-ray energy from the device is equal to the kinetic energy, T, of the electron. This is the potential difference of an X-ray tube, usually referred to as kVp, the peak acceleration voltage in units of kilo electron volts (kV). It is important to note that not all the electron's kinetic energy converts into X-rays. Even in MeV accelerators, only a few percent of the total electron flux is converted into photons. This conversion is even lower for low-energy accelerators like X-ray tubes. Most of the energy is released into the target through heating [46].

Some important features of bremsstrahlung radiation are the strong directional dependence and poly-energetic nature of the X-rays produced. As higher electron energies are used, the higher energy X-rays become more forward-directed. This has a direct effect on the design of radiotherapy devices, as well as their limitations. Figure 3 illustrates the angular dependence as a function of energy for different electron energies. X-rays generated in the lower end of orthovoltage energies (100-500 keV) have a nearly equal distribution in all directions (4π distribution) relative to the electron beam; however, this becomes skewed forward at the higher end [48]. In the MeV range, the X-ray production is nearly all in the forward direction. This phenomenon is explained by the conservation of momentum of the electron/nucleus/X-ray. The higher the kinetic energy of an electron, the higher the momentum in the forward direction. In a three-body problem such as this, the more forward-directed the X-ray must be to satisfy the laws of conservation of energy and momentum [49].

The poly-energetic nature of these X-rays stems from how electrons slow down in a material. While all incoming electrons possess the same kinetic energy, they each undergo different interactions. Electrons traveling closer to the target material's nucleus experience a stronger force.

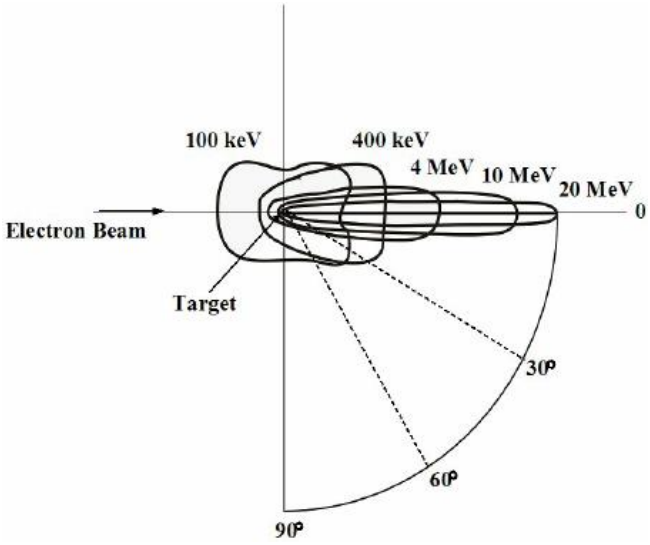

Figure 3. This illustration represents bremsstrahlung X-rays' angular dependence as a function of angle and energy from an incident electron beam [48].

This causes a greater deflection toward the nucleus and a change in kinetic energy [46, 49]. The resulting X-ray will possess this change in electron kinetic energy. Rarely will electrons lose all their energy in one interaction, resulting in X-ray energy equal to T. In most cases only a portion of its energy is lost as an X-ray leaving the electron with a fraction of its initial energy. It is then free to continue interacting with another nucleus, repeating the process. Most electrons undergo multiple interactions before stopping, and this statistical nature of interaction leads to a characteristic poly-energetic X-ray spectrum seen in Figure 4. It shows a decrease in X-ray intensity from 0-50 keV, a product of the anode and tube design [50].

The intensity of the X-rays produced would match that of the blue line. However, since electrons penetrate the anode a short distance, low-energy X-rays produced there do not possess enough energy to exit the material. This X-ray spectrum represents a device with a 150 kVp acceleration potential where the maximum photon energy matches this at 150 keV. The trend of this spectrum would be the same regardless of the acceleration potential of the device, with the maximum photon energy equal to the acceleration potential.

The second form of X-ray production inside a target is characteristic X-rays, as seen in Figure 4. These are emitted from high-Z elements when their orbital electrons transition between atomic energy levels [46]. These occur when there is an electron vacancy in the atom's K shell or n=1 energy level. This is caused by the incoming electrons ejecting these inner shell electrons. It can also be caused by photoelectric ejection or Compton scattering from X-rays of these K-shell electrons. Subsequently, electrons in the n=2 and n=3 energy levels can transition to the n=1 state emitting an X-ray equal to the energy difference of the levels. These are referred to as K-α and K-β characteristic X-rays, and their energy depends on the target's nucleus (energy level separation).

2.2.1 X-ray Tube Operating Principles

Early X-ray tubes, from the early Crooks tube to modern rotating anode tubes, all operate using an electrical potential difference from the cathode (-) to the anode (+) [51].

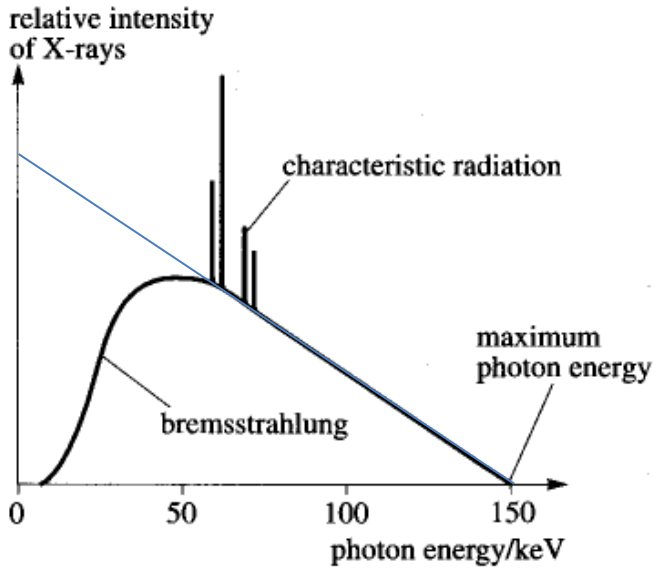

Figure 4. Illustration of bremsstrahlung X-ray Spectrum as a function of energy and intensity. The characteristic X-rays are a product of the target material's electron orbital energies. The maximum energy in this representation is 150 keV, but the spectrum shape would be the same at any acceleration energy [50].

The potential difference between the two is measured in electron volts (eV), and the kinetic energy of the electrons accelerated between the two is equal to this potential difference. A 100-keV tube has an electron energy of 100,000 eV when it strikes the target anode. This takes place inside a vacuum chamber or tube (hence the name X-ray tube) so the electrons can accelerate unimpeded by air or other gases [51]. Early designs generated electrons through the ionization of residual gases inside the tube or trapped in the cathode for acceleration and are referred to as cold cathode tubes. Later designs, such as hot cathode tubes, use thermionic emission of electrons from a tungsten filament heated with electrical current [52]. Thermionic emission is the release of electrons as an effect of high temperature and dramatically increases the number of free electrons to be accelerated [53].

The number of electrons accelerated in a tube is referred to as tube current and is limited primarily by the thermal heating of the target anode [51]. These targets can quickly reach thousands of degrees Celsius, and unless steps are taken to cool the target or the tube current is reduced, the target will melt. Small electron focal spot sizes for imaging are necessary for good image quality, further increasing the heat load per unit area. More complex cooling systems and anode designs have been developed to overcome this while increasing the current and X-ray output. Rotating anode tubes utilize larger, disk-shaped targets that are rotated at very high speeds to spread the heat load from the electron beam over a larger area. The cooling liquid, typically oil, is also used to draw heat from the anode further to be dissipated through radiators or other heat exchangers away from the X-ray tube [51]. Rotating anode tubes are commonly used in CT scanners, radiography, and fluoroscopy machines where size is limited, the focal spot sizes are small, and high electron beam current is necessary for faster imaging times. When focal spot sizes are larger, heat dissipation can be handled sufficiently by air or water-cooled heat sinks with fixed, non-rotating anode targets.

The X-ray output window of these tubes is typically 90º to the electron beam. At orthovoltage energies, the angular distribution of X-rays is still mostly symmetrical around the target, with some forward biasing at higher energies. This means that the X-ray intensity at 90º is nearly the same as the forward direction. However, the anode itself is a dense piece of metal that can self-shield the X-rays produced since they then would have

to travel through the target. The target must be incredibly thin with X-ray tubes, reducing the headload capabilities. For variable energy tubes, different target thicknesses would be needed for each energy, increasing cost and complexity. Locating the beam port perpendicular to the electron beam is a simple way to overcome this limitation with little complexity. Angled anodes are also utilized to increase X-ray beam uniformity along the beam axis. By angling the anode toward the beam port, X-rays produced shortly inside the anode face have less anode material in their path toward the port. However, this does not entirely resolve the issue. As the angle of the X-ray becomes closer to parallel with the anode face, it travels through more material. This creates an effect referred to as the heel of the beam, where the X-ray intensity decreases toward the front of the beam, parallel with the anode face.

Another design consideration for X-ray tubes is the use of beam filters. Filters can be used to increase the effective energy of the X-ray beam by blocking low-energy X-rays. This is called beam hardening, and while it decreases the total output intensity across all energies, it biases the spectrum toward the higher end, which is very useful in imaging and LD-RT therapy with X-ray tubes [54]. Characteristic X-ray peaks can also be "filtered." This is accomplished with layers of low-Z metals or alloys that will block the characteristic X-rays of the previous material until they are no longer present in the spectrum [55].

2.3 Dose Calculation Methods

In radiotherapy, many different algorithms are used to calculate the dose delivered to a patient. This process begins with a CT-scan of the target region, which approximates the electron density and, therefore, attenuation coefficient for each voxel. The simplest calculation methods involve point calculation of dose by approximating pencil beams moving through the voxels [56]. More complex algorithms use a method known as convolution-superposition. This involves many beamlets simulated moving through each voxel where primary beam dose and scatter fractions from surrounding voxels are calculated [57]. These methods involve multigroup energy and tissue calculations to solve the dose delivered to a patient analytically. They depend on accurate beam data to match

the expected output from the RT device [58]. Lookup tables supply many factors, such as beam profile, X-ray attenuation coefficients, and X-ray scattering factors, to approximate the complex physics of radiation interaction.

These analytical methods are employed to simplify the dose calculation and to speed up RT planning. However, they are only an approximation of true radiation transport and may still contain errors. Monte Carlo simulations of the dose delivery result in the highest dose calculation accuracy. This dose calculation method is very computationally expensive, but it has its uses in modern RT planning [59].

Monte Carlo simulation is a valuable tool in nuclear engineering, high-energy physics, and RT dosimetry. These simulations utilize probabilistic calculations of many discrete, random events, which in aggregate forecast useful results. In the case of dosimetry, Monte Carlo methods can simulate individual particles with random trajectories traveling through a defined material. At each point in the material, the probability of a particle event is calculated and assigned to the simulated particle based on cross-section tables, equations, and many other sources of nuclear data [60]. Monte Carlo simulations are considered the closest approximation of true radiation transport and are the most accurate method of determining dose. These models are computationally expensive since particles must be simulated as moving through the material with calculations performed at each step.

The Monte Carlo program MCNP6.2 (Monte Carlo N-Particle) from Los Alamos National Laboratory was selected for its familiarity and long-standing history inside the nuclear engineering and medical physics communities. For complex dosimetry simulations, many particles must be simulated for the desired result, dose, to converge. Convergence in MCNP means that the specified tally region/volume/tissue has had enough particle interactions such that the tally result approaches the mean [61]. For dose calculations, MCNP uses a point kerma (kinetic energy released in mass) calculation to approximate the energy deposited in the region or material. This common calculation technique is used in Monte Carlo simulation and analytical dose calculation programs.

2.3.1 Phantom and Beam Modeling

The method for determining the treatment capabilities of the LD-RT system utilizes MCNP simulation of the entire particle transport process. A working model can be developed by simulating every step in the X-ray generation process, from electron to X-ray interaction in the body. This is used to calculate the dose delivered to a human phantom accurately. MCNP cannot import CT-scan data directly as a reference body for dose calculations. Instead, the VIP-man phantom is used, a voxelized (tomographic) phantom developed from segmented cadaver images obtained from the Visible Human Project [62]. This phantom is composed of 5,941,740 voxels, each 4 × 4 × 4 mm in size. These voxels contain a material composition closely approximating over 60 different tissue types and are placed inside the simulation space to make a standard adult male phantom.

To deliver 1.5 Gy to the isocenter of the lungs, a working beam model must first be developed in MCNP. All X-ray tubes of this energy range have similar operational characteristics with similar anode (target) materials and X-ray ports 90 degrees to the electron beam. They differ in beam port size, acceleration potential (kVp), and tube current (mA), all affecting dose uniformity and treatment times. The acceleration potential (tube energy) has the greatest effect on dose uniformity due to better penetration with energy and must be determined to meet treatment protocols. Our beam simulations are based on the COMET EVO300D, capable of 300 kVp at 3 mA, which should result in good treatment times and dose uniformity. However, should a different tube design or acceleration potential be needed, only a few parameters would need to be changed to develop a new beam model.

The value of VIP-man for evaluating LD-RT lies in the user's ability to specify regions to calculate energy deposition. MCNP delivers energy deposition in MeV/g, which can quickly be converted to Joule/Kg or Gy. By specifying the organs of interest, such as skin, heart, bone, and especially lung, within the treatment field, the dose delivered can quickly be determined in a simulation run. Alterations to the beam can be made by adding filters or using alternate setup geometries to adjust the dose distributions for better coverage and uniformity.

CHAPTER THREE
DOSIMETRY SIMULATIONS

3.1 Simplified Beam Modeling

The first dosimetry simulations are conducted with a bremsstrahlung X-ray source. We found early on that simulating the electron beam/target/X-ray system with the VIP-man model required run times lasting multiple days to a week to get good dosimetry results. This is worsened by introducing filters that further reduced the X-ray flux across the phantom. The complexity of the phantom model, with the increased computational expense of tracking electrons and photons in the same simulation, drastically reduced the computational speeds. This is compounded by the bremsstrahlung X-ray conversion rate of less than 1%. Both factors resulted in a low number of electron simulations per hour and orders of magnitude lower X-ray generation rates, therefore, long dose rate convergence times. This made iteration of the model slow, and any mistakes made with a setup or positioning would waste far too much time. For this reason we decided to model the beam outside the phantom simulation and create an X-ray source for use with VIP-man.

The beam model started with the MCNP simulation of a simplified X-ray tube. This consisted of a target anode made of tungsten and a 1mm Ø electron beam incident on the anode in a vacuum. The anode is many cm thick and angled 20 degrees to the electron beam, as shown in Figure 5, so that: 1) electrons will not penetrate through the anode and 2) the bremsstrahlung X-rays can escape due to the angled face. This design is the same as the source used in the original electron/target/phantom simulation but without any other structures. Figure 5 shows a tallying surface utilizing an FMESH placed at 100 cm, perpendicular to the point at which the electron beam strikes the target. The area of this round surface is 6,962 cm^2 corresponding to an X-ray beam half-angle opening of 27 degrees. This is chosen to roughly match the solid angle of the COMET EVO300D with a 40° × 60° opening angle. The X-ray flux in particles/cm^2 and energy in 1 keV bin is recorded on the tally surface, as seen in Figure 5.

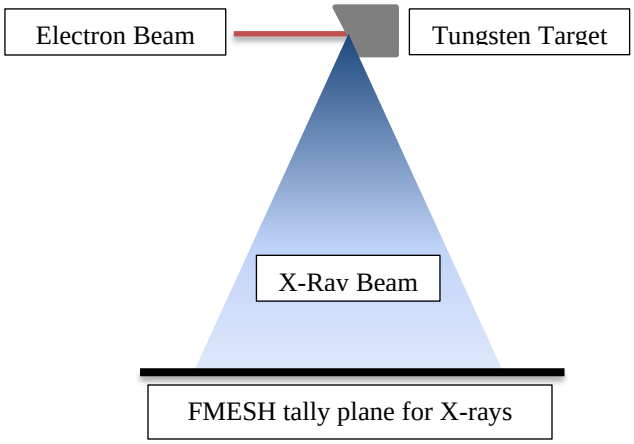

Figure 5. An illustration of the X-ray simulation with the electron beam, tungsten target, X-ray beam, and the tally surface is depicted. While not illustrated, the beam extends from the target to the tally surface in all three dimensions.

The total fraction of X-rays that cross this surface divided by the number of electrons generated in the beam gives the bremsstrahlung X-ray production factor of 0.002448 X-rays/electron. This method is referred to as the photon cone simulation and has the benefit of simplicity. However, many features, such as beam heel and energy/angular dependence of bremsstrahlung X-rays, are lost by producing a photon source with equal energy and flux distribution across the beam's opening angle.

With this electron/target/photon simulation, a new X-ray source is made by normalizing the flux per 1 keV energy bin to act as the emission probability for each energy. The source is set so that every X-ray is generated at a single point with a random vector bounded by the 27º half-angle cone, further increasing calculation efficiency by only simulating photons traveling toward the chest of the phantom. The weight of each photon generated is increased by the inverse of the solid angle, 18.05, since MCNP normalizes to 4π sr by default. The main goal of this new source is to increase simulation speed which it accomplished, shortening the run time from days to hours.

The output spectrum of this new X-ray beam can be seen in Figure 6, and the documented spectrum from the manufacturer. Above 75 keV, the spectra shape matches relatively well. However, below this, the intensity of the simulated spectrum is slightly higher. The characteristic X-ray peaks near ~10, ~60, and ~70 keV match between both simulations. The higher overall intensity in this low-energy region is due to the 4 mm of inherent aluminum filtration present in the manufacturer spectrum. Filters are included in the main VIP-man simulation, where different filters and collimation/tube head designs are iterated. This low-energy region is filtered out to flatten the beam profile.

The main benefits of the photon cone simulation are the speed at which different iterations of beam energy and field size can be created. Detailed modeling of the beam heel, collimation, and even filtration requires many hours of simulation and iterative problem-solving to reproduce an X-ray beam's finer features accurately.

In Chapter Five, an improved beam model is discussed that includes these finer beam features developed from experimental data and beam measurements. The photon cone model discussed in this chapter is sufficient for the initial dosimetry study to prove that a 300 kVp source can achieve the desired dose.

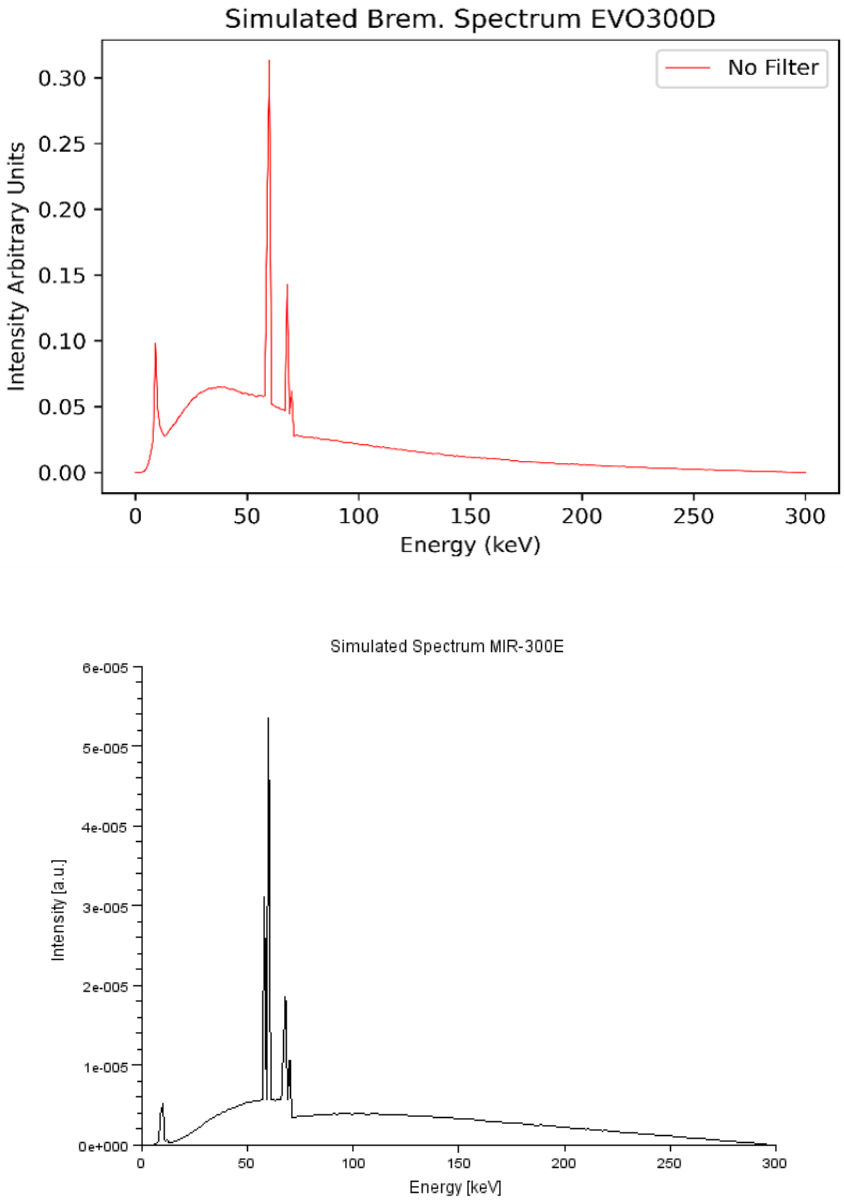

Figure 6. The top image is the MCNP simulated X-ray spectrum the bottom image is the simulated X-ray spectrum from the manufacturer. Both spectra are plots of intensity in arbitrary units versus energy in keV.

3.2 Photon Cone Dosimetry

To calculate the dose, we used an F6 tally to determine the energy deposition in MeV/g for a given tissue of interest. Due to some limitations of MCNP, it is unable to sum the mass of all voxels with the same tissue type, leaving the results in MeV/g/single voxel. Dividing by the number of voxels of each tissue type resolves this issue. However, in MCNP, the tally results are also normalized to one source particle. The number of photons produced depends on the number of electrons striking the target in the simple X-ray tube simulation. The number of electrons depends on the X-ray tube current, in this case, 3 mA. Equation 4 relates the number of electrons to the number of photons produced in the VIP-man simulation, while Equation 5 relates the number of photons to the dose rate in Gy/s. These two equations allow the conversion between the known electron production rate and the simulated X-ray output simulation.

$$nps = Tube\ Current \times Ampere \times Xray\ Production\ Factor \tag{4}$$

$$Dose\ rate = \frac{nps \times F6\ tally \times MeV\ to\ Joules \times Kg}{Number\ of\ Voxels} \tag{5}$$

Tube current is given in mA, and one ampere is 6.242×10^{18} electrons per second. The X-ray production factor describes how many X-rays are produced in the 27º half-angle cone per electron. This product gives nps the number of photons the X-ray tube produces per second. The dose rate (Gy/s) is found by multiplying nps with the F6 tally results in MeV/g/single voxel and converting to Joules with the conversion factor 1.602E-13. Multiplying by 1,000 converts this result from grams to kilograms. The dose rate to any tissue can be determined by dividing by the number of voxels.

To quantify the dose as a function of depth in the lungs, some modifications are made to the VIP-man phantom. We used a custom python script to parse lung voxels' (X, Y, Z) position values in the VIP-man input deck. The Y-axis corresponds to the axis parallel to the beam, the X-axis lateral to the body, and the Z-axis runs superior/inferior.

For each Y position starting at the anterior of the lungs, all lung voxels in the X and Z directions were given a new cell ID number in the simulation. Then a new cell ID is created corresponding to that layer and a new F6 tally. The number of voxels corresponding to each layer is also determined so the dose calculation could be normalized. This modification divided the lungs into 49 layers in the Y direction, as shown in Figure 7, so that dose as a function of depth can be determined. Figure 8 shows the dose vs. depth in the lungs as a function of distance into the body for both the simulated X-ray cone and a full electron/target/X-ray source.

The slight variation in the curves can be attributed to less-than-ideal convergence for the full bremsstrahlung simulation, with some statistical checks for the tallies not passing. Still, the two curves match very closely with these issues, verifying that the bremsstrahlung conversion factor from Equation 4 and the weighting factor in the X-ray cone simulation is correct. The improved simulation speed also improves iteration time with different collimators or filters.

3.2.1 Secondary Electron Dose

One concern with the F6 tally measurement tracking the photon dose is the omission of delta electron tracking. The F6 tally uses a point Kerma deposition calculation to determine the kinetic energy, therefore dose, released in the material. This assumes that any delta or free electrons from a photon interaction release their energy in the same tally volume. However, in a small tally volume, these electrons can possess enough kinetic energy to escape the tally volume. This could artificially increase the dose deposition in the material by assuming all of the kinetic energy is deposited in the original volume.

We can investigate this issue in two ways: 1) using the NIST ESTAR program to determine the maximum range of any secondary electrons and 2) MCNP simulation of small volumes tracking the photon and electron dose in neighboring materials [63].

Using ESTAR, with the ICRP soft tissue material composition, the continuous slowing down approximation (CSDA) range for 300 keV electrons is calculated as 0.084 cm or 0.84 mm.

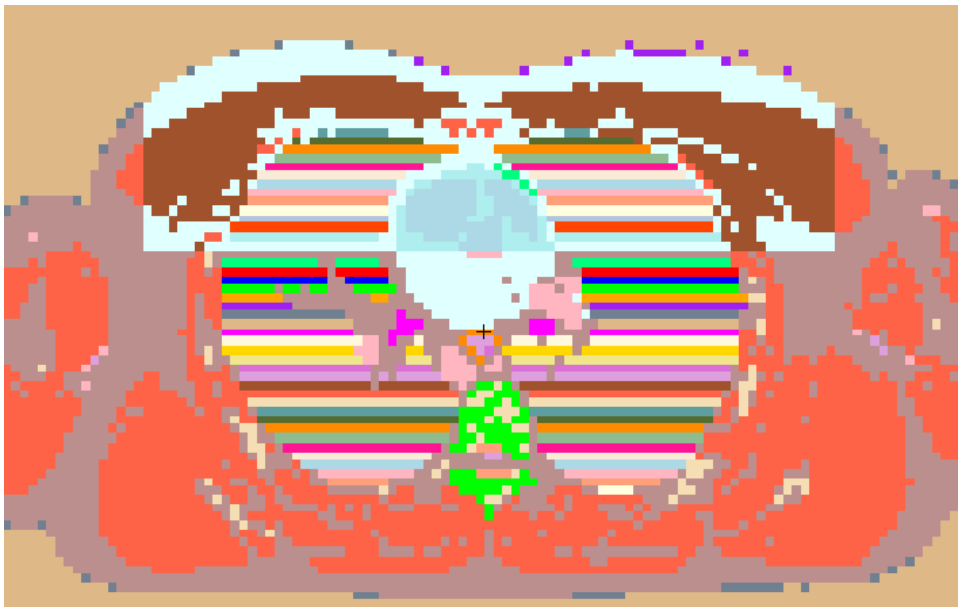

Figure 7. VIP-man transverse cross-section at the mid-chest level. The color scheme is randomly assigned by the MCNP built-in visualization tool. The heart (center white) and chest wall (dark and light red around the peripheral) are distinguishable. The left to right, equally spaced stripes correspond to each lung tissue layer for depth curves. The X-ray source is located out of the frame to the top and directed downwards toward the chest wall.

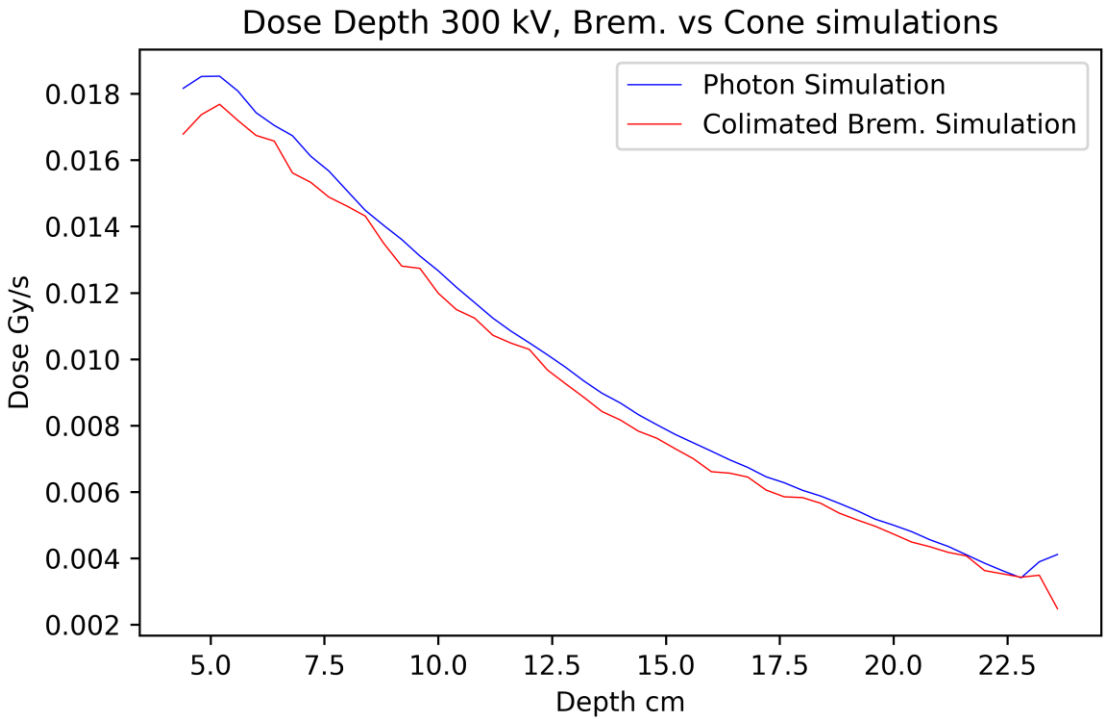

Figure 8. Dose rate versus depth curves as a function of depth into the body in cm for the X-ray cone simulation (Blue) and the full electron/target/X-ray simulation (Red). The slight variation with the collimated bremsstrahlung spectrum can be attributed to poor convergence, and some failed statistical checks even after long simulation times.

This calculation is for the maximum X-ray energy of 300 keV deposited in the electron. A more reasonable approximation would use the average X-ray energy after filtration of 150 keV. This gives an electron range of 0.028 cm or 0.28 mm. These calculations assume that all of the energy of the incident X-rays are transferred to the electron. While this is possible and does happen, it is much more common for only a fraction of the energy to be deposited through Compton scattering, the predominant X-ray interaction mechanism above ~100 keV in the body. Assuming an equal probability of Compton scattering at each angle from 0-180 degrees at 300 keV, the average electron energy is ~96 keV. The CSDA range for this electron energy is ~0.014 cm or 0.14 mm.

The probability of Compton scattering is not equal at all angles, which may underestimate the average electron energy. This calculation also ignores the photoelectric effect, which would result in all the photon energy being deposited in the electron. However, given that the average X-ray energy is closer to 150 keV, a large portion of the X-rays will scatter. It is reasonable to assume that the average electron energy would be lower than the average energy of the X-ray beam and most likely less than ~100 keV from the Compton scatter calculation. With a 4 mm by 4 mm by 4 mm voxel size in the VIP-man simulation, the average 0.14 mm range of secondary electrons is many times smaller than the size of these voxels. This suggests that the effects of secondary electrons leaving the tally volumes are negligible.

This is verified with a simple MCNP simulation with voxels equivalent to the 64 mm^3 voxel size of the VIP-man phantom. An array of 27, 4 mm by 4 mm by 4 mm water voxels is arranged in a Rubik's Cube configuration. The photon and electron flux is tallied for the central voxel to track the electrons moving into and out of the volume. The electron flux for the central voxel is 0.0223% of the photon flux. This suggests that a minimal number of electrons are shared between neighboring voxels. The difference in dose for the F6 tally with photons and F6 tally with electrons is 0.8% suggesting that F6 tallies of the photon dose are sufficient for calculating the dose rate to internal structures.

Furthermore, the in-scatter and out-scatter for neighboring voxels will be approximately equal since the X-ray flux locally is the same. Therefore, the average dose from secondary electrons would be equal to the photon dose using a point kerma deposition

in regions with a low dose gradient. The only region this would not hold is at the body's surface, where electrons would scatter into the air and not into neighboring tissue regions. Omitting electron tracking improves the computation time and efficiency by tracking only one particle type.

3.3 Filter Design

The unfiltered X-ray spectrum shows a steep dose gradient from the front to the back of the lungs. Not shown in Figure 8 is the higher dose rate to the front of the chest wall, skin, and other tissues. By hardening the beam with the addition of a filter, the dose rate is more uniform with depth. Material selection is important for a filter due to characteristic X-ray production and attenuation. A Thoraeus filter is comprised of tin, copper, and aluminum [55]. This hardens the beam while each successive layer attenuates the characteristic X-rays of the previous layer. Typical material thicknesses for 200 – 400 keV X-ray tubes are 1.2 mm of Tin, 0.25 mm of copper, and 1 mm of aluminum. Figure 9 compares the Thoraeus filtered spectrum with the unfiltered photon beam spectrum showing a slight decrease in high energy X-rays with a substantial reduction in X-ray intensity below ~100 keV.

It is important to note that increasing filter thickness decreases the total X-ray intensity, therefore, the dose rate. Figure 10 shows how this filter compares to a 4 mm solid Copper filter in flattening the dose depth curve. Another factor contributing to the steep dose gradient with distance is the short source-to-surface distance (SSD) of 35 cm. This is chosen due to the large opening angle of the collimator, allowing us to take advantage of the $1/r^2$ relationship between dose rate and distance to the source, r. This shortens the treatment time but increases beam divergence through the body.

To calculate the treatment time and total dose delivered to the lungs, skin, and heart, lung plane 26 is chosen as it is roughly the center of the lungs. The prescribed dose at the isocenter of 1.5 Gy divided by the dose rate at this layer gives the treatment time in seconds for each setup. Table 1 contains the dose, dose rates, and treatment times for filtered and unfiltered anterior-posterior (AP) beams.

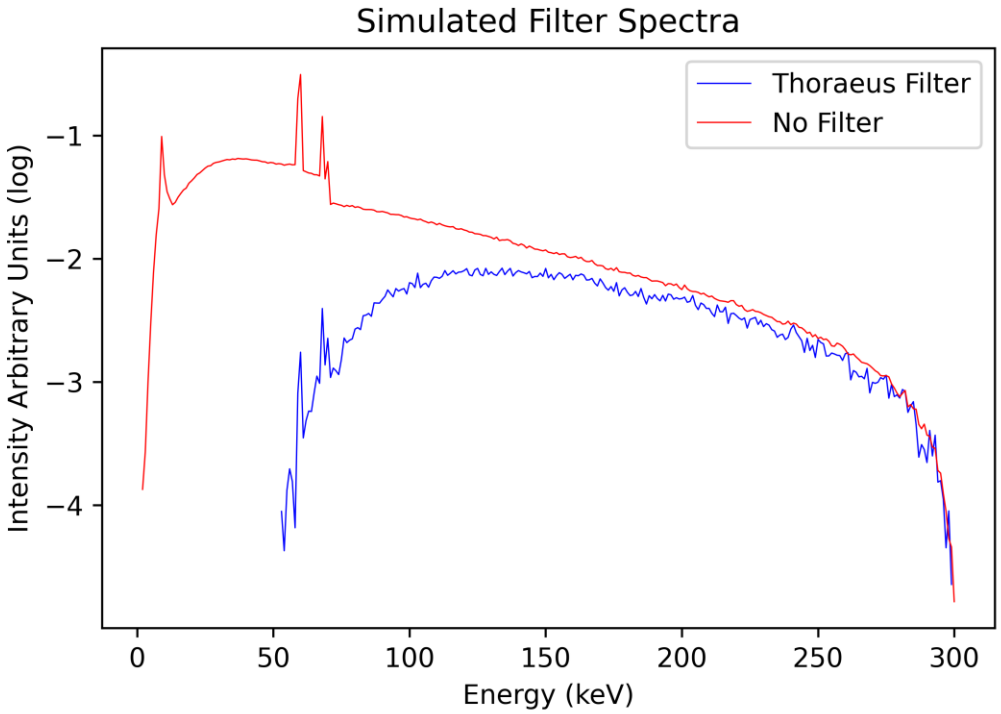

Figure 9. Log scale of X-ray intensity vs. X-ray energy in keV for an unfiltered photon beam and a Thoraeus-filtered photon beam. The intensity below ~130 is many times lower with the filter while only slightly lower at the higher energies.

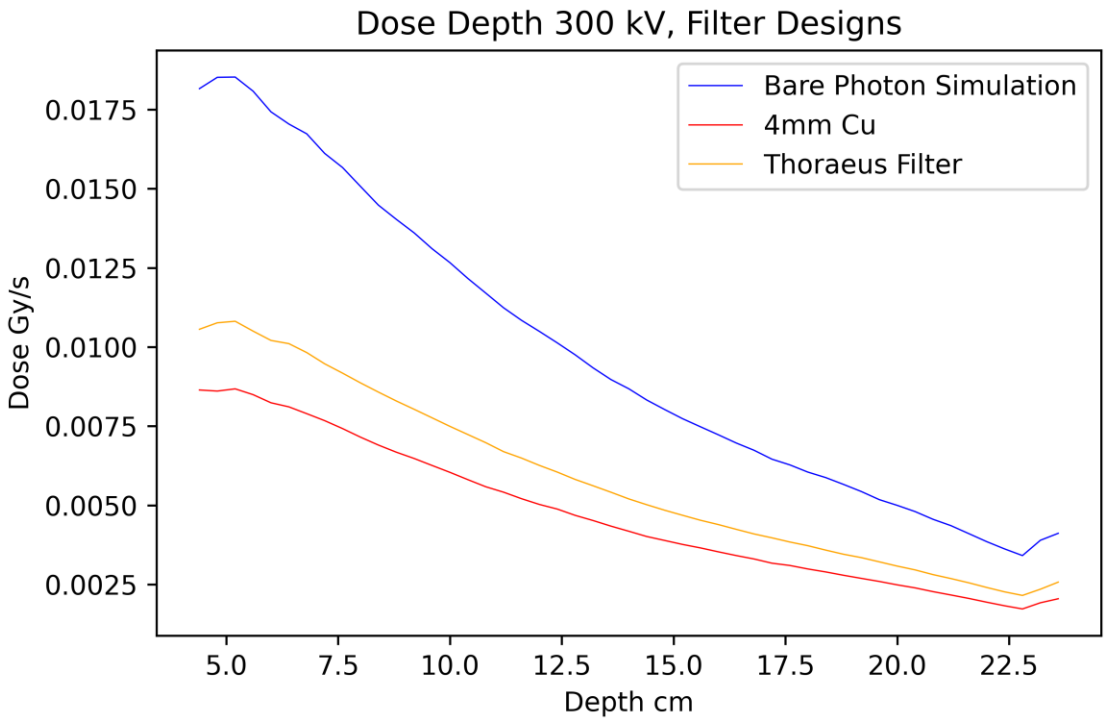

Figure 10. Dose rate vs. depth in lungs for an unfiltered photon beam, a Thoraeus filtered beam, and a 4 mm Copper filtered beam for comparison. Note the shallower slope of the filtered beams compared to the unfiltered beam shows improved dose uniformity.

Table 1. Dose, dose rate, and treatment times for organs of interest.

Filter Type	**Skin Rate**	**Skin Dose**	**Heart Rate**	**Heart Dose**	**Lung Rate**	**Lung Dose**	**Time**
Photon simulation	1.77 cGy/s	297 cGy	0.84 cGy/s	140 cGy	0.84 cGy/s	140 cGy	167 s
Thoraeus filter	1.0 cGy/s	288 cGy	0.5 cGy/s	137 cGy	0.50 cGy/s	140 cGy	277 s
4mm Cu filter	0.84 cGy/s	292 cGy	0.4 cGy/s	138 cGy	0.41 cGy/s	140 cGy	345 s

The addition of filters nearly doubled the treatment time due to the decrease in beam output across all energies. The marginal improvement of the skin dose suggests that the low energy X-ray flux is still high enough to cause a substantial entrance dose. However, the shallow slope of the filtered lung dose curve shows improved uniformity with depth.

3.4 Parallel Apposing Fields

A two-field setup is a common technique to spread the entrance dose across a larger body area. However, understanding the dose distribution to the lungs and skin will require a different visualization method. As shown in Figure 7, the MCNP visual representation of VIP-man cross sections is unable to display dose information in a useful way. To solve this, a Python script is used to parse the input deck and determine the voxel material type, ID, and density for each (X, Y, Z) position. With this, cross-sectional views of each plane can be plotted for better visualization with custom color maps. With commercial treatment planning software, dose overlays are placed on CT scans of the anatomy represented in Hounsfield Units or HU. These are calculated with Equation 6 and depend on the measured attenuation coefficient of X-rays through a given voxel in the body in reference to the attenuation coefficient of water [64].

The attenuation coefficient of a material is equal to the electron density times the cross sections for photoelectric, coherent, and incoherent scattering. If we assume that all tissues' electron density and cross sections are roughly equivalent, then mass density can be substituted for the attenuation coefficient in Equation 7.

$$HU = \left(\frac{\mu_{tissue} - \mu_{water}}{\mu_{water}}\right) \times 1{,}000 \tag{6}$$

To calculate the HU or CT number, the attenuation through a voxel μ_{tissue} is subtracted from the attenuation coefficient for water μ_{water}, and finally divided by the attenuation coefficient for water, μ_{water} and it is multiplied by 1,000. This means pure

water would have a HU value of 0, with all other tissues scaling from that value proportional to their attenuation coefficient.

$$HU' = \left(\frac{\rho_{tissue} - \rho_{water}}{\rho_{water}}\right) \times 1{,}000 \quad (7)$$

By replacing μ with density, ρ, any tissue with a density equal to the density of water would still have a HU´ of 0. With this correction, applying a grayscale to the HU values gives roughly the same contrast as a CT scan.

Now the corresponding (X, Y, Z) tally results for lung tissue must be determined in simulation to represent the dose distribution at different cross-sectional layers. Again, due to some memory limitations of MCNP, the entire lung volume could not be read out in a single simulation. So, F6 tally results could be generated for a single cross-sectional plane at a time in each simulation run. Once simulated, the positional dose per voxel is calculated using Equation 5 and overlaid with the approximated CT scan for the 2-D dose distribution seen in Figure 11. The same process is repeated for the coronal plane in Figure 12.

Next, a posterior-anterior (PA) beam is simulated with the same SSD distance of 35 cm to the back of the phantom with the same isocenter. This gives another dose distribution map for comparison with the previous beam geometry, which can be seen in Figure 13. This distribution leads shows that a PA field setup performs slightly better due to the location of the heart when compared to the anterior-posterior (AP) field. With most lung tissue posterior to the heart, the PA beam is less attenuated through the centerline.

These two fields were combined and weighted individually to achieve the most uniform dose distribution through the lung volume, increasing dose uniformity. The resulting weights are 0.35 AP and 0.65 PA, meaning that weighting the beam towards the back improved the lung dose coverage shown in Figure 14. If we consider the attenuation of the beam to be similar through the chest and the back walls, the heart would be the major contributor to this difference in weighting. Figure 15 also shows improved dose uniformity over the coronal plane at the isocenter. It is apparent from Figures 14 and 15 that opposing AP and PA fields, weighted correctly, further improve the dose distribution to the lungs.

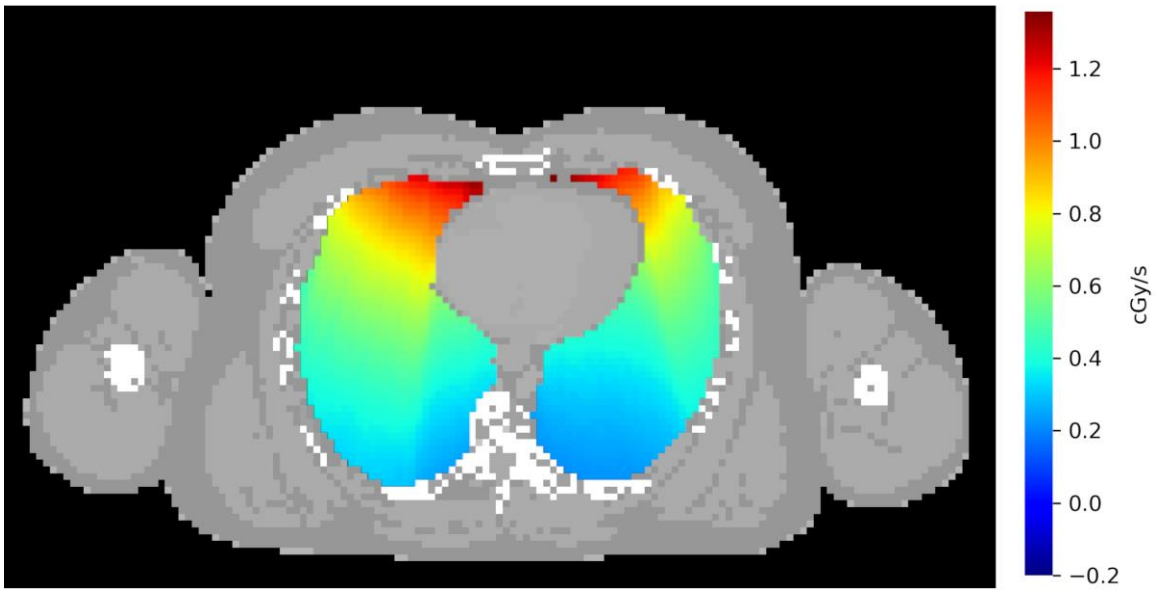

Figure 11. A transverse plane view at the isocenter with an AP beam and a lung dose overlay.

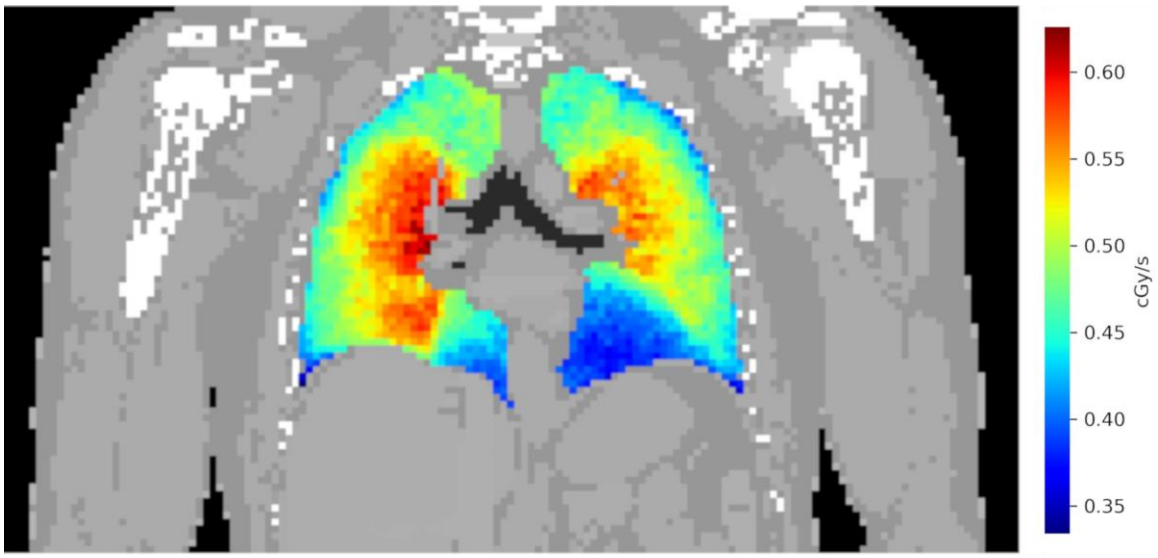

Figure 12. A coronal plane view at the isocenter with the dose to the lungs overlaid.

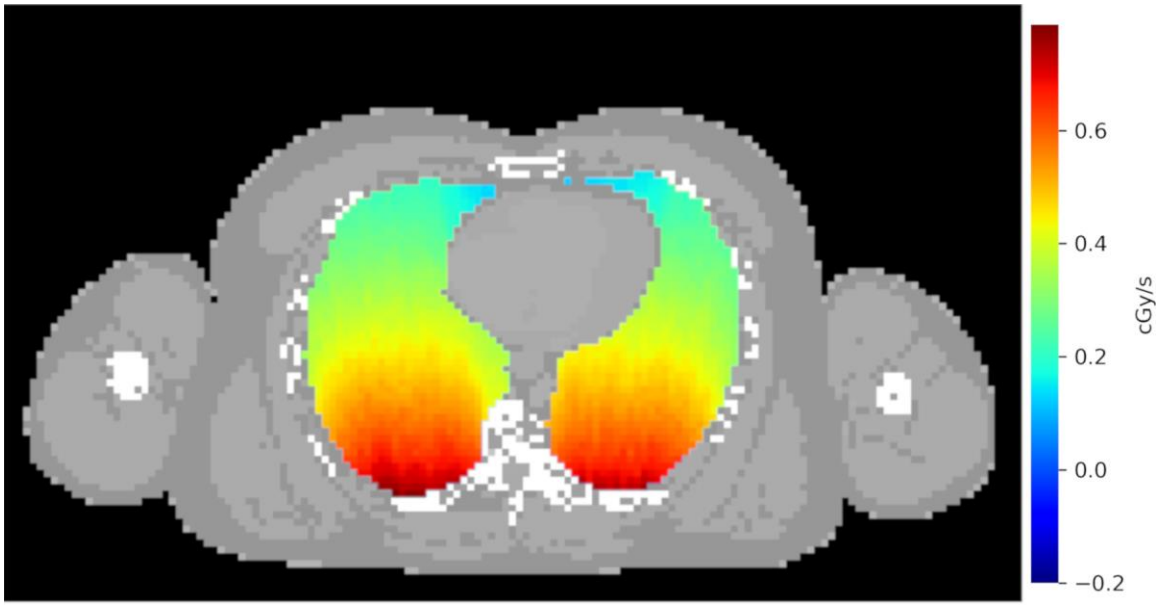

Figure 13. A transverse plane view at the isocenter of the dose to the lungs with a PA beam setup.

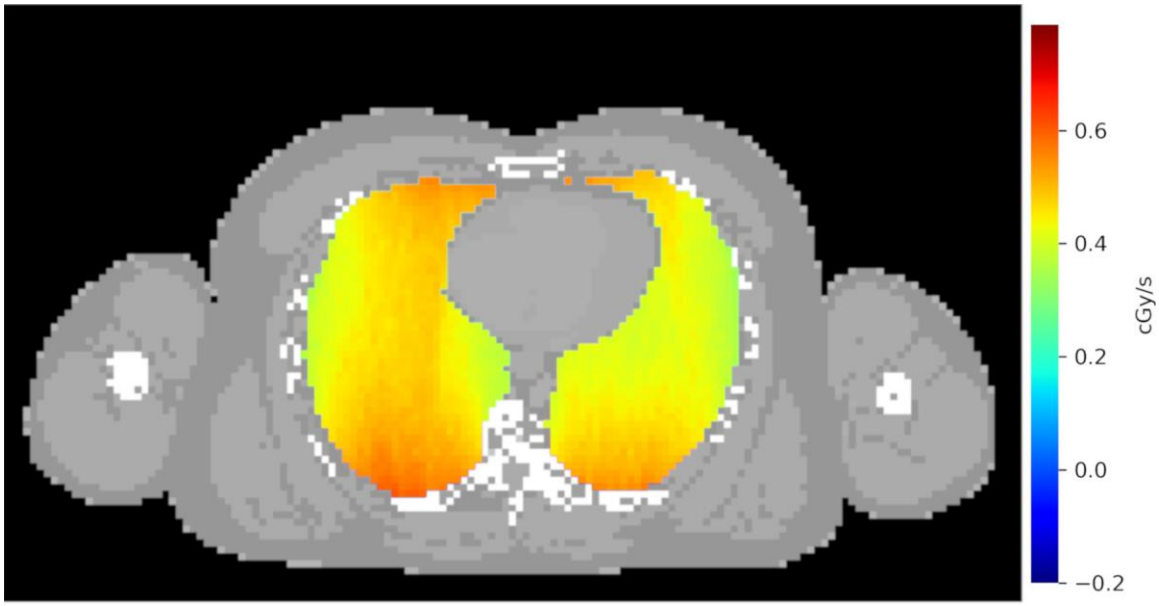

Figure 14. A transverse plane view at the isocenter with a 0.35 AP and 0.65 PA beam weighting results in a uniform dose distribution.

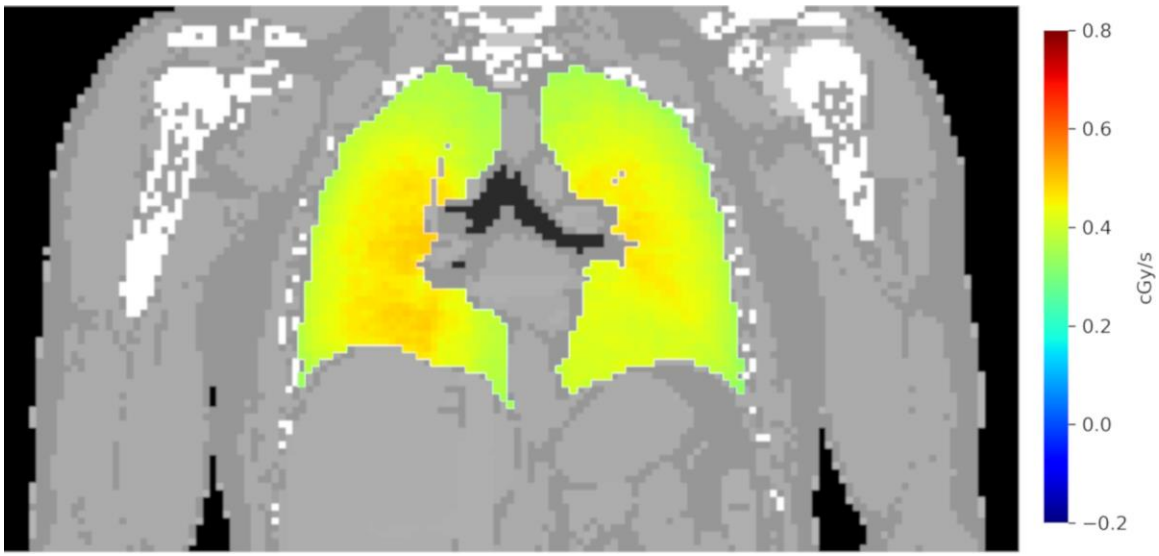

Figure 15. A coronal plane view at isocenter with a 0.35 AP, 0.65 PA beam weighting.

Unfortunately, the skin entrance dose is not tallied correctly for the PA beam and reported total skin dose across the entire body. To accurately determine the dose to the chest and back, the VIP-man phantom would need to be further modified. This is because the dose is tallied across the total skin volume, not just the area in the beam. However, by applying the beam weights to the skin dose from the AP beam, we can estimate that the back and chest would receive approximately 1.8 and 1 Gy, respectively.

Additional field setups could be investigated to spread the entrance dose over a greater area. Focusing the beam on one individual lung at a time from orthogonal directions could further improve dose uniformity. This would also allow for tighter beam collimation, improving the dose depth profile due to less beam divergence. This would come at the cost of prolonged treatment time, past the ~5 minutes of the current method.

The photon cone simulation, while simplified, proves that X-ray coverage of the lungs is possible with a 300 kVp X-ray source given the right field setup and filtration, hardening the beam. Futher investigation of the non-uniformity of the beam and the effects this may have on dose coverage with respect to depth as well as axial and lateral coverage due to the heel effect and other profile non-uniformities in Chapter Five and Chapter Seven.

CHAPTER FOUR
RADIATION ENCLOSURE

4.1 Design Specifications

To improve our beam model and incorporate the finer features of the profile, experimental data specific to the X-ray tube must be gathered for validation. To collect this data with the X-ray tube at 300 kVp @ 3 mA (maximum output), a radiation enclosure must be utilized to adequately protect the experimental personnel and members of the public from radiation exposure. The final location for this radiation enclosure is in a machine shop/high bay in the basement of the nuclear engineering building. This area has uncontrolled access by students, faculty, staff, and visiting personnel from outside the university. With this in mind, the radiation safety committee at The University of Tennessee set a maximum dose rate of 0.5 mR/hr, 5 cm from the surface. With this goal, two methods of shielding calculation were used. The National Council on Radiation Protection reports (NCRP reports) and MCNP simulation [65].

NCRP reports are commonly used to design and implement shielding for various applications, from X-ray imaging rooms to MV Linac vaults. A second calculation with MCNP is also used since the tube model and dosimetry simulations are all produced in MCNP. This secondary, independent calculation method verifies that adequate shielding is in place with the radiation enclosure. This provides an additional level of safety and reassurance that the design is adequate. After completion of the shielding design and construction of the X-ray enclosure, survey meters are used to ensure the dose rate meets the design goal. Any adjustments or modifications to the construction of the X-ray cabinet will be made if any point exceeds the dose limit.

During this design process, we were made aware of an X-ray cabinet from National X-ray in the process of removal from a laboratory on campus, as seen in Figure 16. It was previously used as a small animal irradiation cabinet with a 160 kVp X-ray tube.

Figure 16. Image of the national X-ray radiation cabinet used as the basis for the NCRP calculations and the MCNP shielding simulations.

The interior dimensions are roughly 3 by 3 by 3 ft., providing adequate space for our experimental purposes. Because it was originally designed for a 160 kVp tube, the walls were made of 1/4 in. lead plate between two sheets of 1/8 in. steel sheet. This was verified by measuring the layers in the door cutout, as seen in Figure 17. The cabinet door is made of the same steel/lead sandwich with an 8 by 12 in. leaded glass window in the center of the 24 by 30 in. door. The glass lead equivalent is 1/4 in., equal to the lead in shielding. The floor of the cabinet, which acts as the primary beam stop for the X-ray tube, has an unknown thickness of lead. Primary beam stops are usually thicker than the secondary surfaces, such as the walls, ceiling, and door. The beam stop is the most critical shielding surface because the beam is aimed at this surface. We assume that the thickness incorporated in the original construction is inadequate for the beam stop calculations and add additional shielding equal to the total beam stop thickness calculated.

4.2 NCRP Shielding Calculations

Several NCRP reports cover shielding design for X-ray systems, spanning various energies and setups. NCRP report no. 49 covers structural shielding design for medical use of X-rays up to 10 MeV [66]. NCRP report no. 151 supersedes report no. 49 and covers shielding design for megavoltage X-ray and gamma radiotherapy facilities while ignoring orthovoltage energies [67]. NCRP report no. 147, issued in 2004, covers shielding design for medical X-ray imaging facilities. However, the X-ray energies discussed in the document reach a maximum of 150 kVp, half the maximum energy of this system [68]. These reports share many commonalities in the calculation methodology, symbols, and equations for determining the necessary shielding for a facility. The main differences between each document are the energy of the primary beam, attenuation profiles for different materials, and scattering profiles for different energies and materials.

From NCRP report no. 49, Equation 8 is used for primary barrier thickness, and Equation 9 calculates the secondary or scatter barrier thickness.

Figure 17. Measurement of the sandwiched lead shielding in the X-ray cabinet before modification. 1/8 in. of steel, 1/4 in. of lead, and another 1/8 inch of steel are shown. The 1 in. steel piece at the end of the tape measure is a structural steel tube.

Both equations rely on several factors that must be known or estimated before calculating the primary and secondary barrier thicknesses [66].

$$K_{ux} = \frac{P(d_{pri})^2}{WUT} \tag{8}$$

$$K_{ux} = \frac{P}{aWT} (d_{sca})^2 (d_{sec})^2 \frac{400}{F} \tag{9}$$

The variable, d_{pri}, is the distance from the X-ray source to the measurement location 5 cm beyond the primary barrier. d_{sca} is the distance from the X-ray tube to the phantom or the SSD. d_{sec} is the distance from the phantom to the secondary barriers (the walls of the cabinet). U is the use factor, a value between 0 and 1 corresponding to how often the beam is pointed in this direction. P is the maximum dose rate per hour at the location of interest. T is the occupancy factor, representing how often a person would be at this location. W is the workload factor in mA-min. F is the X-ray field size at the surface of the patient. Variable a is the scatter factor 90° to the patient. Table 2 shows the values used for each variable with a brief description. The result K_{ux} is an attenuation factor that can be used in Figure 18, which is Fig. 2 in Appendix D of NCRP no. 49, to find the thickness of lead needed to reach this reduction in intensity. Several curves are included at 200 kV, 250 kV, and 300 kV for pulsed X-ray tubes and 300 kV and 400 kV constant potential curves. The curve used is the 4th from the left, with 300 kV constant potential, which matches our tube the closest [66].

From equation 8, the attenuation value K_{ux} for the primary beam is 1.55e-6. Using the curve in Figure 18, this represents a primary barrier thickness of ~27 mm of lead. This seems reasonable given the tube energy and the assumption of occupancy and use factors equal to 1. From equation 9 the K_{ux} value for the secondary scatter barrier is 2.67e-5, corresponding to ~17 mm of lead for the secondary barriers.

NCRP no. 151, which supersedes NCRP no. 49, uses Equations 10 and 11, which have the same form as Equations 8 and 9. However, they are used with Equations 12 and 13 to calculate the barrier thickness.

Table 2. The variables, their values, and their descriptions for use in equations 8 and 9.

Variable	Value	Description
d_{pri}	0.7 m	Distance from the X-ray source to a point 5 cm beyond the primary barrier.
d_{sca}	0.35 m	Distance from the source to the front of the phantom. SSD of 35.
d_{sec}	0.56 m	Distance from the center of the phantom to a point 5 cm beyond the walls.
U	1	Use factor of 1 suggests that the beam will always face the beam stop.
P	0.0005 mR	This is the dose rate in mR/hr converted to R/hr.
T	1	An occupancy factor of 1 suggests that a person may always be present beside or around the cabinet in an uncontrolled area.
W	180 mA-min	The workload factor is calculated by multiplying the tube current of 3 mA by 60 minutes.
F	1000	Field size is calculated using the 40° by 60° opening angle at 35 cm SSD. This represents an area of roughly 25 by 40 cm.
a	0.0019	This is the scatter fraction which indicates the fraction of radiation scattered 90° from the phantom at 300 kVp.

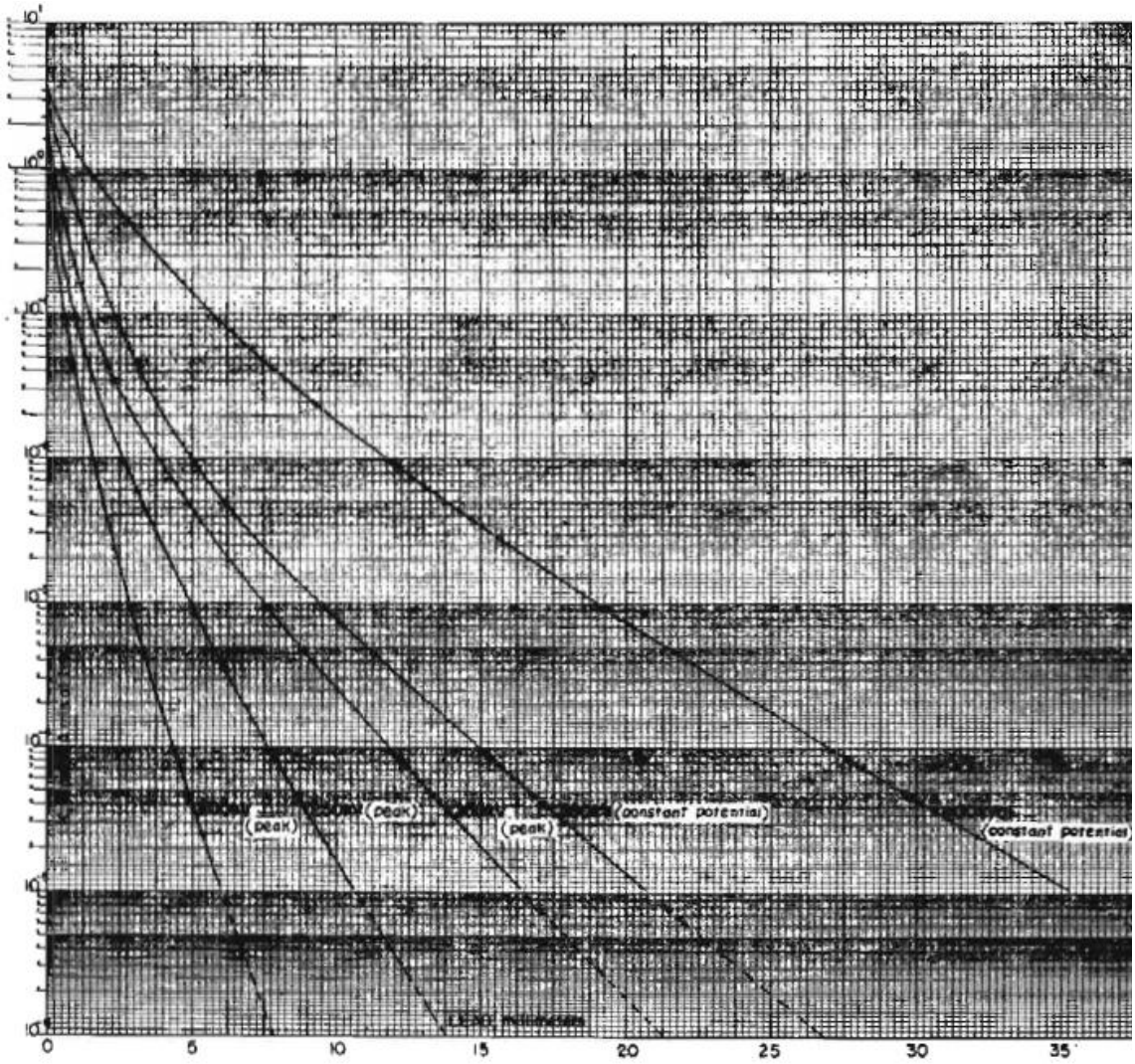

Figure 18. This table is the transmission factor curve, Fig. 2 of Appendix D from NCRP report no. 49. The lines from left to right are 200 kV pulse, 250 kV pulse, 300 kV pulsed, 300 kV constant potential, and 400 kV constant potential. The transmission values calculated for the primary and secondary values are matched with the Y axis and the 300 kV pulsed curve. The X-axis at this point is the lead shielding required in mm [66].

$$B_{pri} = \frac{P\, {d_{pri}}^2}{WUT} \tag{10}$$

$$B_{ps} = \frac{P}{aWT}\,(d_{sca})^2\,(d_{sec})^2\,\frac{400}{F} \tag{11}$$

$$n = -\log(B_x) \tag{12}$$

$$t_{barrier} = TVL_1 + (n-1)TVL_e \tag{13}$$

The values used in these equations vary slightly from the units outlined in Table 3. By taking the log of B_x corresponding to the primary or secondary barrier transmission factor (equation 12), n represents the number of tenth value layers or TVL needed to reduce the transmission factor to the prescribed dose limit. Equation 13 calculates the thickness of the barrier using TVL_1 and TVL_e (equilibrium). The two different tenth-value layers of the desired material are used to account for spectral changes of the radiation as it penetrates the barrier (beam hardening). Because NCRP no. 151 was written for MV beams, the spectral changes of the beam are significant with depth. However, this data is not available for kV orthovoltage sources. We can assume that the beam does not shift as it penetrates the barrier and uses the same TVL for TVL_1 and TVL_e in equation 13. This would conservatively overestimate the shielding thickness required, adding more shielding. The scatter factor, a, is not available for orthovoltage beams in NCRP report no. 151. It was reused from NCRP report no. 49 [67].

With a TVL value of 0.22 cm determined from the tube voltage scale in Figure 19, the primary beam stop thickness calculation with NCRP report no. 151 is 15.5 mm. The secondary thickness is calculated as 12.4 mm. These two factors differ from the values calculated with NCRP report no. 49, which were 27 mm and 17 mm, respectively. The difference in these two calculation methods can be attributed to the average tube energy scale used in report no. 151.

The scale suggests the TVL layers are selected based on the tube energy's average X-ray energy, corresponding to about ~120 kV with a 300 kVp source. Using this value reduces shielding for both the primary and secondary barriers. Report no. 49 has explicit calculations for X-ray tube energies of 300 kVp. For this reason, the primary beam stop thickness of 27 mm would be more reliable. However, this report assumes that the energy of the scattered X-ray spectrum is equal to the primary beam in the secondary shielding calculations.

Table 3. Variables, values, and descriptions for use in equations 10 and 11.

Variable	Value	Description
d_{pri}	0.7 m	Distance from the X-ray source to a point 5 cm beyond the primary barrier.
d_{sca}	0.35 m	Distance from the source to the front of the phantom. SSD of 35.
d_{sec}	0.56 m	Distance from the center of the phantom to a point 5 cm beyond the walls.
U	1	Use factor of 1 suggests that the beam always faces the beam stop.
P	0.000005 Gy	This is the dose rate in Gy/hr converted to resulting in a dose of 0.5 mR/hr.
T	1	An occupancy factor of 1 suggests that a person may always be present beside or around the cabinet in an uncontrolled area.
W	15	Workload factor is the output in Gy/hr
F	1000	Field size is calculated using the 40° by 60° opening angle at 35 cm SSD. This represents an area of roughly 25 by 40 cm.
a	0.0019	This is the scatter fraction which indicates the fraction of radiation scattered 90° from the phantom at 300 kVp.
TVL	0.22 cm	The TVL was taken from Figure 19 for a tube energy of 300 kVp.

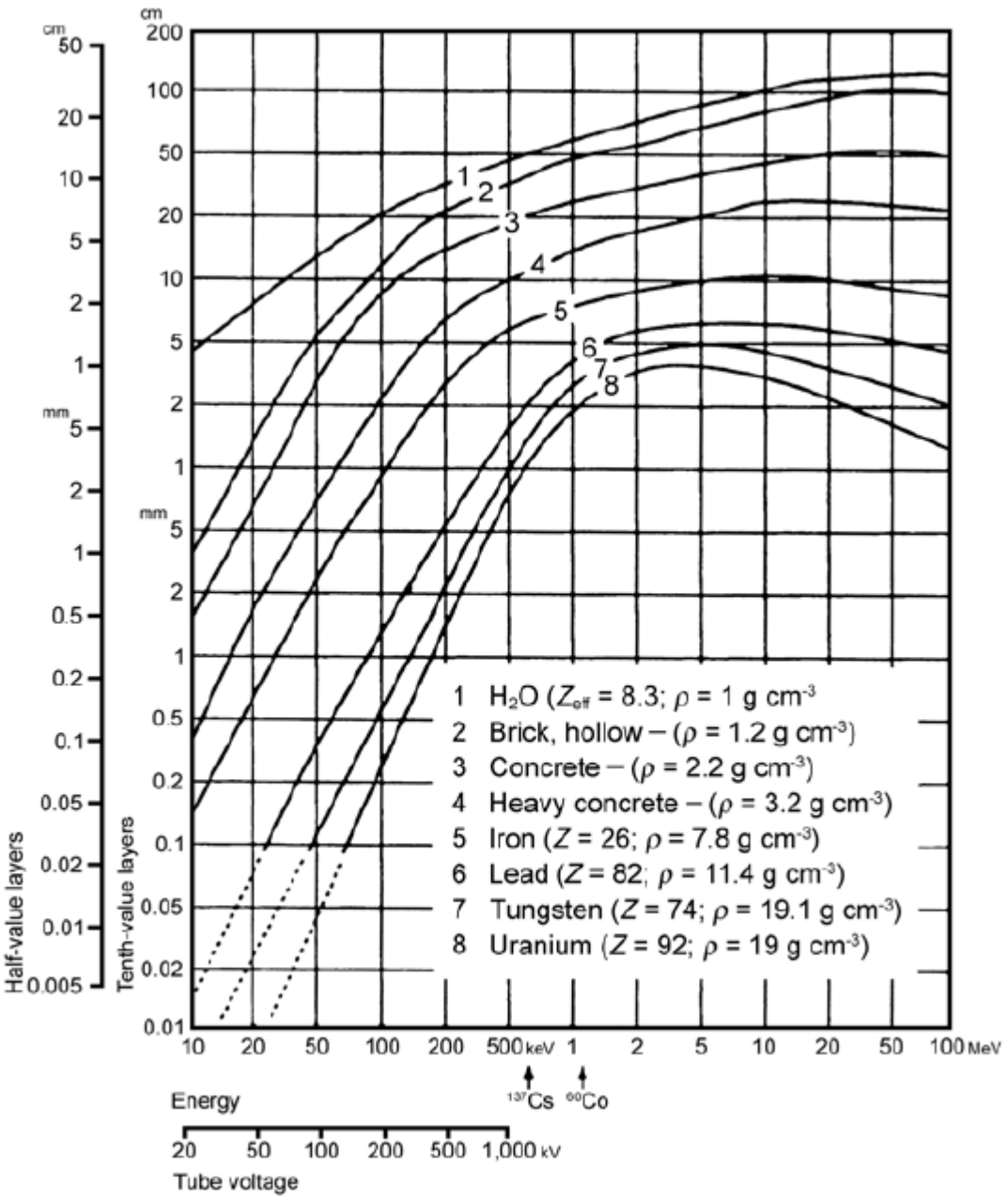

Figure 19. Tenth-value layers versus energy for different shielding materials, Fig. A.1a from NCRP report no. 151. The TVL value for the 300 X-ray tube is interpolated from the scale on the bottom left and its intersection point with the line labeled 6, which is lead. The TVL at this tube energy for this material can be read on the Y axis [67].

Due to the physics of Compton scattering, this is not possible. A 300 keV X-ray Compton scattering 90° is less than 190 keV. Therefore, the X-ray spectrum striking the secondary barriers would be at much lower energy. For this reason, using the average tube energy TVL from Figure 19 in report no. 151 would better estimate the secondary barrier thickness.

Furthermore, both report no. 49 and no. 151 are for the shielding design of rooms. This involves much larger distances where the primary and secondary barriers are multiple meters away. Neither report was specifically written for shielding calculation of a small cabinet with the primary and secondary barriers close to one another. This could affect the accuracy of these calculations.

4.3 MCNP Shielding Calculations

From work done in Chapter Three, the X-ray beam model has been shown to accurately reproduce the X-ray spectrum and flux of the COMET EVO 300D in MCNP. The shielding requirements calculated using the NCRP reports can be tested using this model by modeling the entire system. By modeling the X-ray tube and the radiation enclosure, we can ensure that no errors were made in the NCRP calculations and prove that the assumptions made are valid. Given the high output of the X-ray tube, ensuring the shielding design is adequate is vital for the safety of the operators as well as meeting state and federal regulations for exposure limits.

Modeling the X-ray cabinet began with building a lead box with the same outer dimensions as the radiation enclosure, 40.5 by 40.5 by 40.5 in. This lead box has a wall thickness of 1/4 in. to match the original shielding thickness of the box. Inside each face, 1/8 in. of steel is included to match the original design. The outer layer of steel is not included for two reasons: 1) iteration of the lead shielding is easier when dealing with one continuous layer of material, and 2) by not including this additional 1/8 in. of steel, it acts as a safety margin with slightly more material included on the actual X-ray cabinet. The internal square steel tubing acting as structural bracing in the corners and around the door is not included for the same reasons. The bottom floor of the cabinet acts as the beam stop.

As discussed prior, 1 in. of lead bricks will be added. This additional 1 in. of lead is included on the floor of the simulation, making the beam stop many times thicker than needed.

The X-ray cone source is placed inside this box at the approximate mounting location, 55 cm off the floor and ~35 cm from the door's front wall. This is because the beam opening of the tube is offset from the center, forcing the beam off-center in the cabinet. On the cabinet floor, in line with the beam, a human-sized water cylinder is placed with a radius of 15 cm to act as a scattering center. Outside the box, planar water phantoms 5 cm by 100 cm by 100 cm are placed on each face of the box, 5 cm from the surface shown in Figure 20. These act as dosimetry volumes, and an F6 tally is used to calculate the dose rate at each point.

One challenge with using Monte Carlo simulations for shielding design arises from the statistical nature of particle transport through materials. When determining the dose rate outside the shielded box, enough particles must interact with the tally volumes for statistical convergence. The goal of shielding is to stop particles from exiting the box. Still, paradoxically particles need to exit the box to evaluate the shielding performance and calculate a dose rate. This requires more particles to be simulated, drastically increasing the run time of the simulations. To assess the shielding design in a fast and efficient manor, different techniques must be utilized.

Variance reduction is a term that encompasses different methods of improving the speed and efficiency of Monte Carlo simulation. There are many different techniques to achieve this. The method used in these shielding simulations is known as importance weighting. In MCNP, particles are assigned importance when they enter a cell. In analog transport, the importance of the particle is set to 1. This means that each particle is tracked through each interaction process, and the weight is modified based on these interactions. When the importance of a particle type in a cell is increased above 1, this effectively splits the particle into multiple particles equal to the importance number. The weight of each of these new particles is then divided by the importance number. If importance is set to 2, the particle entering this cell is split into two particles whose combined weight equals the original particle.

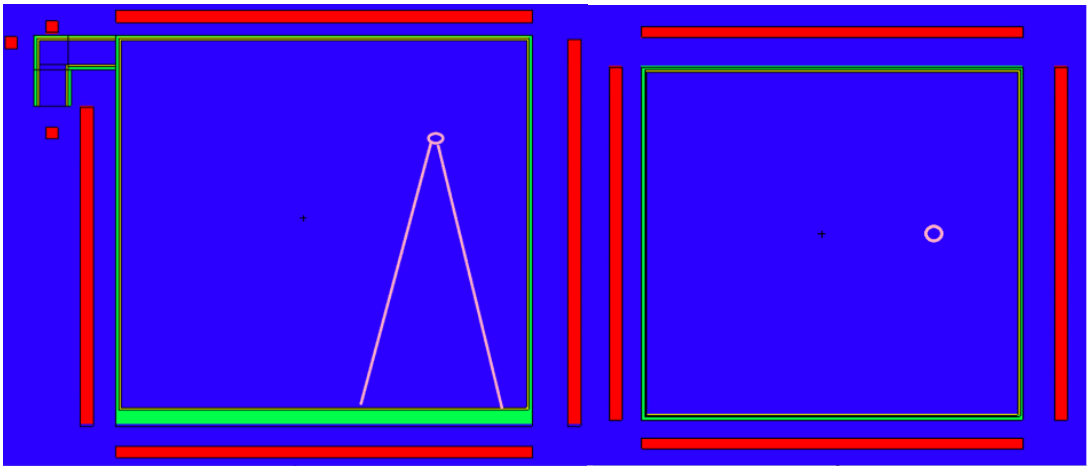

Figure 20. A cross-sectional view of the MCNP model of the X-ray cabinet with the X-ray beam outline for visualization. The green volumes are lead, the blue represents air, and the red volumes are the water tally volumes 5 cm from each face of the box.

Since there are now two particles, the probability of these particles making it through the material is doubled. However, due to the lower weight, the statistical results would remain as if analog transport were still followed. This allows for much faster convergence since the probability of particles making it through the shielding is significantly increased.

The shielding must be split into multiple layers to employ importance weighting effectively. This is so each layer can be a different cell with different importance. The original 1/4 in. shield is split into four 1/16-inch-thick layers of lead. The importance for each layer is then increased to 5, 25, 125, and 625. Care must be taken so that the importance is not increased too much. This can cause errors, crashes, or the simulation to take longer than pure analog transport. With this variance reduction method, convergence is much faster (hours), and dose rates can be calculated in a reasonable amount of time. Through iteration of different shielding thicknesses, we found that ~1 cm of lead would be sufficient in reducing the dose rate outside the box to below 0.5 mR/hr for an uncontrolled area.

4.4 Cabinet Construction

The results of the two different NCRP report calculations and the MCNP simulations suggest that 1 cm to 1.7 cm of lead is needed for the secondary beam stop. Given the 1/4 in. or 0.635 cm of lead already inside the cabinet's walls, another 0.4 cm to 1 cm of additional lead shielding needed to be added to the secondary barriers. The result of the MCNP simulation proposes a total lead thickness of ~1 cm. This is the minimum amount of shielding to reduce the dose to the entire tally volume below 0.5 mR/hr. This does not consider the non-uniformity of lead thickness that may be present after modification of the cabinet. It also averages the dose over the entire tally surface, not considering that the dose through the barriers perpendicular to the beam are highest. The MCNP simulation provides an independent calculation that differs in methodology from the NCRP-based shielding calculations and is in the ballpark of these calculations.

To be conservative, an additional 1/4 in. of lead or 0.635 cm would put the total secondary lead barrier thickness at 1.27 cm, slightly more than the 1.24 cm calculated with

report no. 151. This small margin of lead thickness plus the 1/4 in. of steel would allow for any non-uniformity in material thickness and an added safety factor.

Due to the ease of placing lead bricks on the cabinet floor when compared to attaching the lead to the cabinet walls, a full 1 in. or 2.54 cm will be added for the beam stop. The bricks, plus the shielding already inside the cabinet, exceeds the most conservative calculation of 2.7 cm from report no. 49. If the dose survey finds that additional lead is needed on the cabinet walls, additional lead will be added.

The dimensions of the X-ray cabinet require roughly 42 by 42 by 1/4 in. lead plate to be added to each face, weighing 180 pounds each. This can be pretty unmanageable, making the construction of the box difficult. We decided that adding two layers of 1/8 in. lead sheet to each face would be easier for two people to lift and put into place. A thinner lead sheet would also allow additional 1/8 in. layers to be added if needed. Using two thinner layers also allows for overlapping corners by alternating the order in which sheets are attached. This is an essential feature of the design to limit streaming points. When two pieces of material come together at a corner, even with exact measurement and fitment, it is still possible for tiny gaps to be present. For this reason, many shielding designs incorporate overlapped joints, so the next layer covers these small gaps. In this design, we accounted for 1.5 to 2 inches of overlap between each face of the cabinet.

We must also consider how the lead sheet is attached to the box to ensure shielding does not come off or the overlapped seams do not open, resulting in radiation streaming points. Construction adhesive was selected due to its relatively low price and adherence abilities. However, given that each lead side in contact with the outer layer of the box weighs ~180 pounds, relying solely on adhesive does not seem adequate. The lead sheet, 1/8 in. thick, is relatively stiff, and with lateral support, roughly 40 by 40 in. pieces can stand on end as long as it is not allowed to bow. With this in mind, attaching a shelf to the box's perimeter would allow the lead sheets to sit on the bottom edge, and the adhesive would provide the lateral support keeping the sheet from bowing out in the center. With this solution, the weight of the lead is supported by the shelf, not placing the adhesive interface under sheer force.

Before construction, 11 sheets of 4 ft. by 4 ft. by 1/8 in. lead sheets and 36 12 by 4 by 1 in. interlocking lead bricks were ordered from Pure Lead Products allowing for two sheets on each side and the top. If additional lead is needed at any point, one extra sheet is available for remediation. The interlocking bricks for the beam stop limit streaming between each other by fitting together male and female V grooves along each edge.

The fixture points used to attach the X-ray on light, cable chases, door hinges, and latch were removed to make each face flat and flush mount the lead sheet shown in Figure 21. The shelf supporting the lead sheets on each side of the box is mounted to the 2 by 2 in. steel tube that structurally supports the sides of the box. The paint is ground off along this perimeter, and 1 in. angle iron is welded to the bare metal, as shown in Figure 22.

Once the steel shelf is attached to the cabinet, the lead sheet is attached to each face. Each sheet is cut to size with enough extra material for ~1.5 to 2 inches of overlap with the adjacent faces. This is done using tin snips. After cleaning both the lead and the surface of the cabinet, the adhesive is applied to the surface of the cabinet. The lead sheet is lifted, placed against the side, and supported on the ledge. Large pieces of plywood and 4 by 4 in. wood posts were used along with large clamps to tightly press the lead sheet to the cabinet, as seen in Figure 23.

In order to provide sufficient overlap between the cabinet and the door, the lead sheet is placed on the inside surface. When the door is closed, the original 1/4 in. of lead and the new 1/4 in. of lead sheet on the outside of the cabinet line up. However, the gap is not perfect, and there is still a ~1/8 in. gap between the shielding on the door and the cabinet. The door design has a 2 by 1 in. steel tube covering this gap, acting as the door jamb that tightly fits against the outside of the cabinet shown in Figure 24.

Before adding shielding, this overlap at the door jamb was sufficient to stop leakage around the door at 160 kVp. During testing, this area would be closely monitored with handheld dosimeters to determine if leakage is present. The back side of the cabinet has a steel cable chase composed of a 4 by 6 in. steel channel for routing data and power cables to the X-ray tube and other experimental devices in the box. As shown in Figure 24, this chase is also wrapped in a lead sheet and overlapped with the sheet covering the back wall of the X-ray cabinet and cables were routed prior to mounting the X-ray tube.

Figure 21. Images of the X-ray cabinet with the door removed and the paint removed from the 2 by 2 in. steel tube at the bottom of the left image. The hinges seen here were also removed.

Figure 22. Image of 1 in. angle iron being fixtured with clamps on each face before welding.

Figure 23. Image of the X-ray cabinet with the lead sheet held in place with wood 4 by 4 in. posts and plywood to apply even pressure. Notice the overlapping seams along the edges.

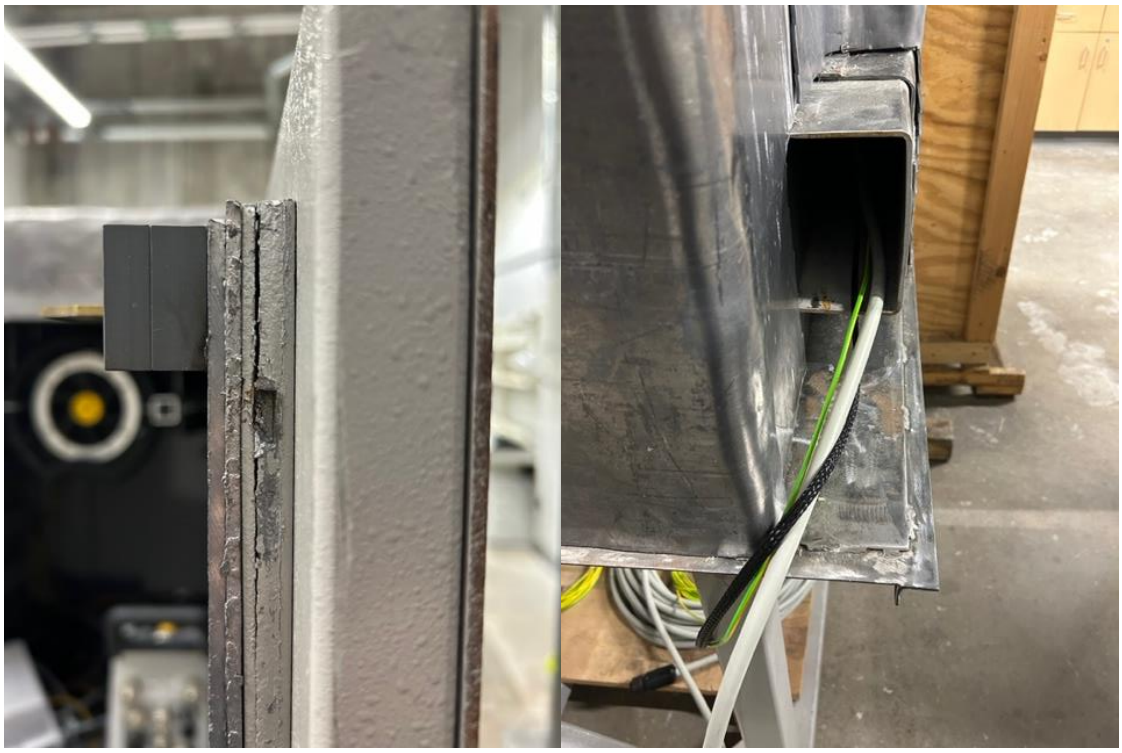

Figure 24. Images showing the addition of lead sheets to the inside face of the door with the interlock blade installed. The right image shows the cable chase and cables routed to the inside of the cabinet.

The X-ray tube came with a mounting bracket designed to attach to the round carry handles on each end of the tube. This bracket is too large and did not position the tube in the correct location inside the cabinet. Instead, square aluminum tubes were attached along each side of the X-ray tube to the carry handles to mount the X-ray tube. These tubes had many mounting holes spaced 1.5 inches on center the entire length of the aluminum tube. These tubes allowed pieces of all-thread to run through these holes, suspending the tube from the roof of the cabinet. 4 pieces of 14 in. all-thread were selected, allowing for leveling and height adjustment. Holes were drilled and tapped to mount the all-thread to the ceiling of the cabinet. They were located in the 2 by 2 in. steel tubes that act as structural support for the top of the cabinet. By a stroke of luck, these structural steel tubes were spaced perfectly at each corner to line up with the holes in the aluminum bars mounted to the X-ray tube. The X-ray tube is mounted on each piece of all-thread with a nut suspending the tube from the ceiling of the cabinet shown in Figure 25.

With the tube mounted, the nut on each piece of all-thread could be adjusted to level the X-ray tube front to back and left to right. The power and ground cables were attached to the back of the X-ray tube, and the door interlock connected to the cable run through the chase before tube mounting. The door interlock and X-ray light on the outside of the X-ray tube were tested with the tube in safety mode. This test ensured all safety features operated as designed before X-rays were produced.

With radiation safety staff present and with multiple dosimeters and Geiger counters, the shielding of the X-ray cabinet is ready for testing. The first test is conducted with the 12 mm lead plug installed, blocking most of the X-rays at 300 kVp and 3 mA of beam current. After surveying the cabinet, only background radiation levels were detectable, and the beam block is removed. At full power, a survey of each side of the box is conducted, again paying close attention to the areas surrounding the door, the cable chase, and the areas directly adjacent to the X-ray tube. The left and right sides of the cabinet parallel to the X-ray beam were very close to the 0.5 mR/hr exposure limit. One small area at the top of the door jamb also exceeded the 0.5 mR/hr exposure limit. The door is the highest reading, with the detector indicating ~1 mR/hr from the center and the top.

Figure 25. Image of the X-ray tube suspended from the ceiling of the cabinet on all-thread rods that attach to the square aluminum tubes. U-bolts attach the square aluminum tube to the round handles at the front and back of the X-ray tube.

The leakage rate from the X-ray tube is documented as 5.0 mSv/hr. This leakage rate plus the scatter inside of the X-ray cabinet is enough to raise the exposure rate at the two sides of the box to be near the 0.5 mR/hr exposure limit. The leakage area above the door jamb is likely due to door fitment causing a small streaming point. The leakage through the door is likely a combination of the tube and door designs. Because bremsstrahlung X-rays are slightly forward-directed at 300 kVp, the X-ray leakage through the front of the tube is likely higher than at other angles. Combined with the fact that the tube is slightly off-center and closer to the door, this limits the $1/r^2$ decrease in dose at this surface. The cabinet was originally designed with a leaded glass window in the center of the door. This is covered with an additional 1/4 in. of lead. It is possible the window provided slightly less protection than 1/4 in. of lead at 300 kVp. These factors contributed to a higher than allowable dose rate at this location.

These hotspots were mitigated by adding more lead shielding to each of these locations and around the tube itself. Another layer of 1/8 in. lead sheet is added to the left and right sides, covering an area larger than the hotspots identified with the survey meter. A lead belt is wrapped around the X-ray tube head to further limit the lateral leakage. Attaching a lead strip inside the doorjamb mitigated the streaming point at the top of the door. Another lead sheet is added to the inside of the door. After these modifications, the cabinet is surveyed again. At full power, the cabinet achieved a dose rate well below the 0.5 mR/hr limit. Figure 26 shows the completed X-ray cabinet before painting to prevent contamination from the exposed lead sheet.

Figure 26. Finished X-ray cabinet with the door mounted and all shielding requirements met.

CHAPTER FIVE
BEAM VERIFICATION

5.1 Improved Beam Model

As discussed in Chapter Three, a new beam model that accurately reproduces the X-ray profile is needed to simulate the dose distribution in VIP-man better. The new X-ray beam production method is called the nested cone model. This simulation begins like the photon cone simulation in Chapter Three with an angled tungsten anode 20 degrees toward the beam opening. However, this method differs in the way the tally surfaces are generated. Due to the angular distribution of bremsstrahlung X-rays with respect to the direction of the incident electron beam, this is leveraged to create a double-dependent source where energy and flux are dependent upon the angle. The tally surface, in this case, is a sphere centered at (0,0,0), the location at which the electron beam strikes the tungsten anode. From this point (0,0,0), cones with half-angle openings from 1 to 179 degrees are placed with respect to the electron beam. These cones intersect the sphere surrounding the simulation space creating 180 concentric rings to tally the energy and flux at each emission angle, as shown in Figure 27. This geometry construction method, while complex, ensures that the surface normal of each ring points to the interaction location of the electron beam in the tungsten target at the position.

This method presents an issue when normalizing the emission probability for each 1-degree emission angle. First, the probability of emission from each angular bin must be proportional to the total area of the ring. Second, attenuation of the beam by the target reduces the tally results for rings that are partially blocked by the target. The first issue is resolved by multiplying the weight of each angular bin by the area of the ring where the photons are tallied. The second issue requires a simulation where the bremsstrahlung X-rays are restricted to only interact with the rings in areas without attenuation. The tally results for each interaction area can then be normalized to 1 so that the photon emission probability for each angle is equal to that of the actual X-ray tube.

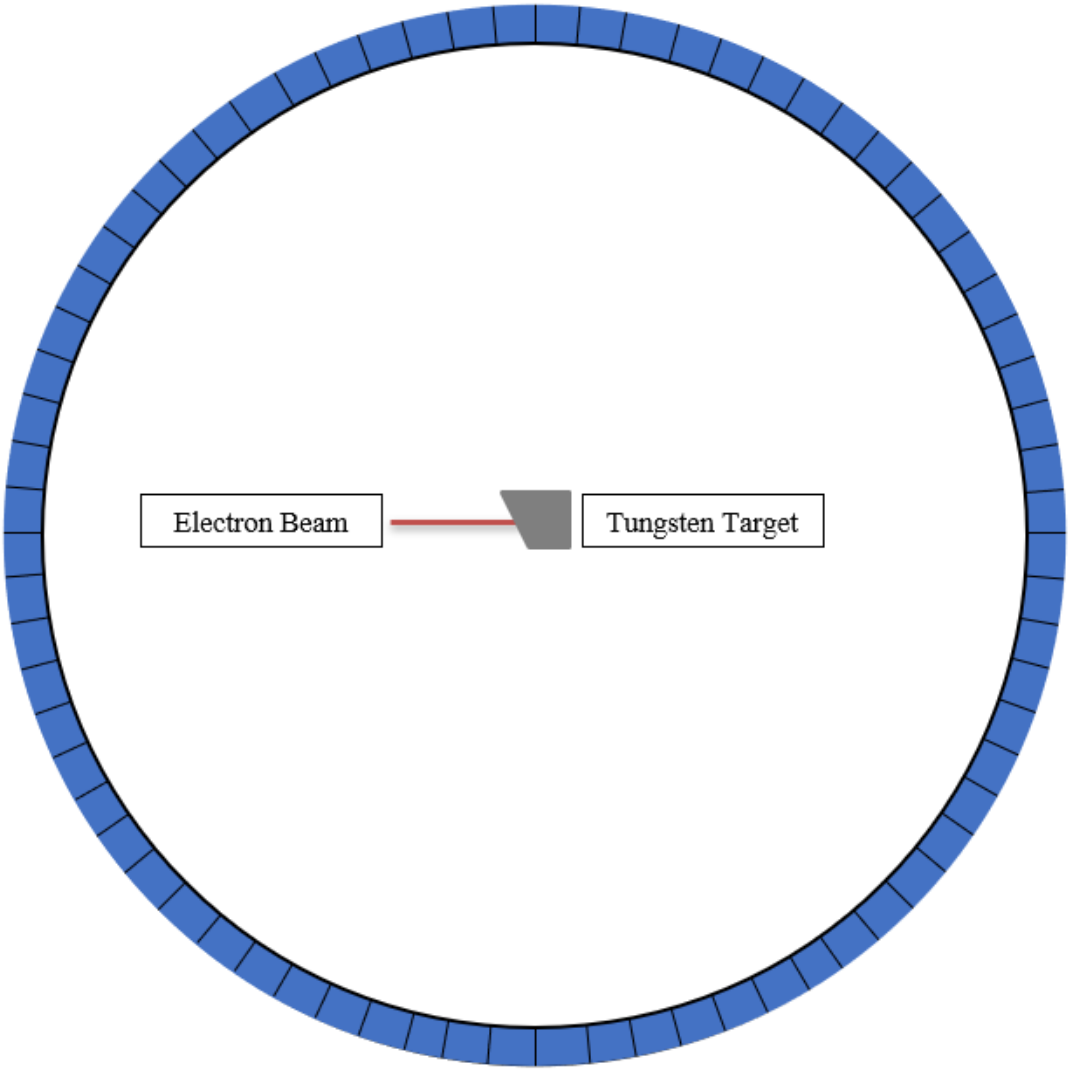

Figure 27. Nested cone bremsstrahlung simulation showing the electron beam interacting with the tungsten target. The blue region is the F4 tally volumes with 1-degree emission angles. Each section of the blue tally volume corresponds to a ring-like tally volume coming out of the page. This image shows a cross-section of the X and Y plane only.

This second restricted emission angle simulation could produce the energy flux relationship without using the entire ring simulation. However, with 1 keV energy bins and each ring having a relatively small solid angle, the entire ring allows the statistics for each energy bin in each angular bin to converge much faster. To match the output of the X-ray tube, a tally region is placed 35 cm from the target on the central axis in the electron/bremsstrahlung X-ray simulation. This region uses an F6 tally to determine the photon dose per source electron. Once the angularly dependent (nested cone) X-ray source is produced, a simulation with an identical tally volume 35 cm from the target location along the central axis is tallied for photon dose. The ratio of the tally results between the two simulations allows for scaling the dose rate to the tube current in mA.

The filter design with this X-ray tube model is also redesigned with this simulation compared to the photon cone model. The original design used 1.2 mm of tin, 0.25 mm of copper, and 1 mm of aluminum. The 1.2 mm of tin is replaced with 1 mm of cadmium sheet metal in the new filter. This change is due to an international shortage of tin, resulting in difficulties sourcing the material at the time of experimentation. Cadmium is close to tin in Z number, Z of 48, and a density of 8.65 g/cm^{3,} and tin's Z number 50 with a density of 7.3 g/cm^3. 1 mm of cadmium is chosen to account for the difference in density and attenuation by the denser metal. The filtered and unfiltered X-ray spectra are shown in Figure 28. The relative intensity of each spectrum is normalized to highlight the differences. In reality, the intensity of the filtered spectrum is much lower due to the attenuation of photons across the entire energy spectrum. This figure highlights how much harder the filtered spectrum is compared to the original causing a much higher average photon energy and improving penetration.

5.2 Beam Measurement

The X-ray beam profile along the central axis is an important feature that must be modeled accurately. This dimension corresponds to the beam profile parallel to the electron beam inside the X-ray tube head.

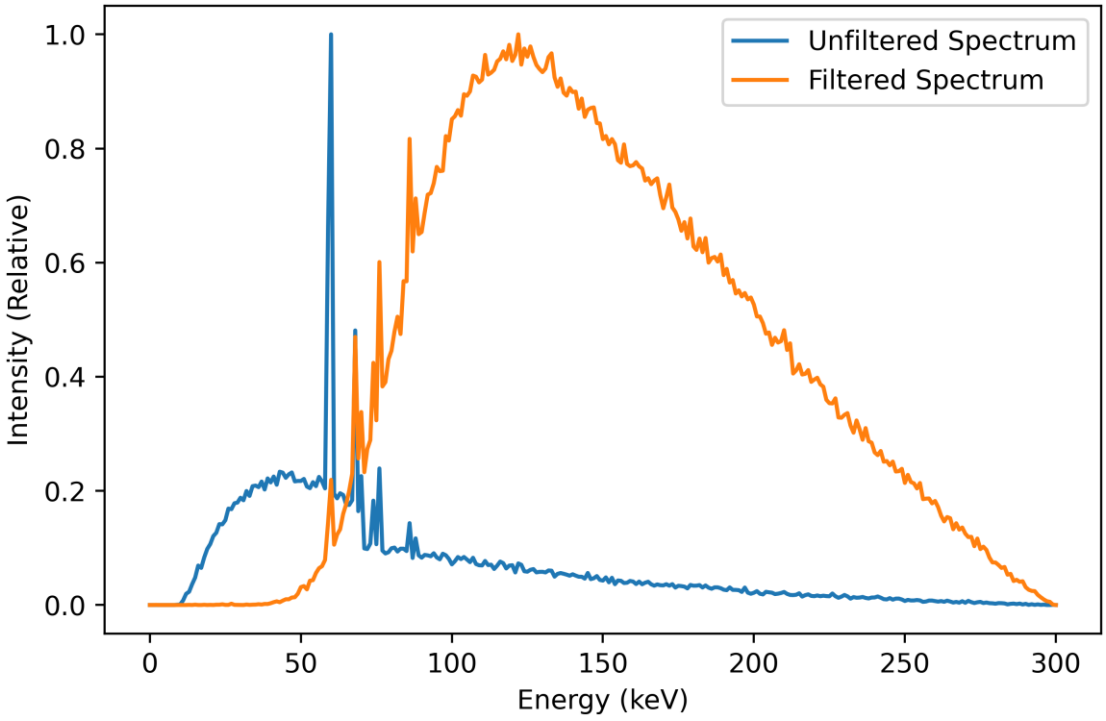

Figure 28. Overlay of the filtered and unfiltered spectra simulated in MCNP. The intensity of each spectrum is normalized to 1 to show the relative spectrum shapes. The actual intensity of the filtered spectrum is many times lower than the unfiltered spectrum.

Within the target, photons experience different amounts of attenuation based on the path length out of the target towards the X-ray beam port. Towards the front of the X-ray beam, photons generated in the target anode travel a path nearly parallel to the anode face, causing more attenuation, which can be seen along the X-ray beam profile. This heel must be accurately modeled since the lower beam intensity due to attenuation leads to lower dose rates. The lateral profile perpendicular to the electron beam must also be measured. The intensity decreased with distance from the central axis with a slight dependence on the path length through the target; however, this profile should be symmetric on both sides of the central axis. With both profiles, the intensity decreases with an r^2 dependence toward the edges of the field.

To verify the accuracy of the nested cone beam profile, measurements were taken with a Sun Nuclear IC PROFILER shown in Figure 29. This device contains 251 parallel plate ion chambers: 63 on the X-axis, 65 on the Y-axis, and 63 along each diagonal. The chambers are arranged in a 32 by 32 cm array, with 5 mm spacing between each detector. Each detector has a volume of 0.046 cm^3. The front plane of the device is made of PMMA acrylic with an inherent buildup layer of 0.94 g/cm^2, roughly equivalent to 1 cm of water. The MCNP simulated profiles in the X and Y direction were produced with an *FMESH at 35.9 cm SSD with a simulated buildup layer from 35.9 cm to 35 cm to match the inherent buildup within the IC profiler. This tallies the energy flux per voxel. A detailed simulation of the IC profiler is created with ion chambers embedded into PMMA, matching the specifications from Sun Nuclear. F6 tallies were used to calculate the energy deposited in each detector volume. This is compared to the results of the *FMESH covering the same area as the detector. There is no discernable difference between the two profile shapes. Therefore, due to its simplicity, the *FMESH profile method is used for all further simulations.

With this device, the X-ray beam profile is plotted along the X and Y dimensions and compared to the simulated profile for the same dimensions, as shown in Figure 30 and Figure 31. These measurements were also conducted with the cadmium multilayer Thoreus filter shown in Figure 32 and Figure 33. Each profile is normalized to the intensity of their respective central axis to compare their shape.

Figure 29. Pictures showing the Sun Nuclear IC profiler used to generate the beam profiles and PDD curves with the central axis.

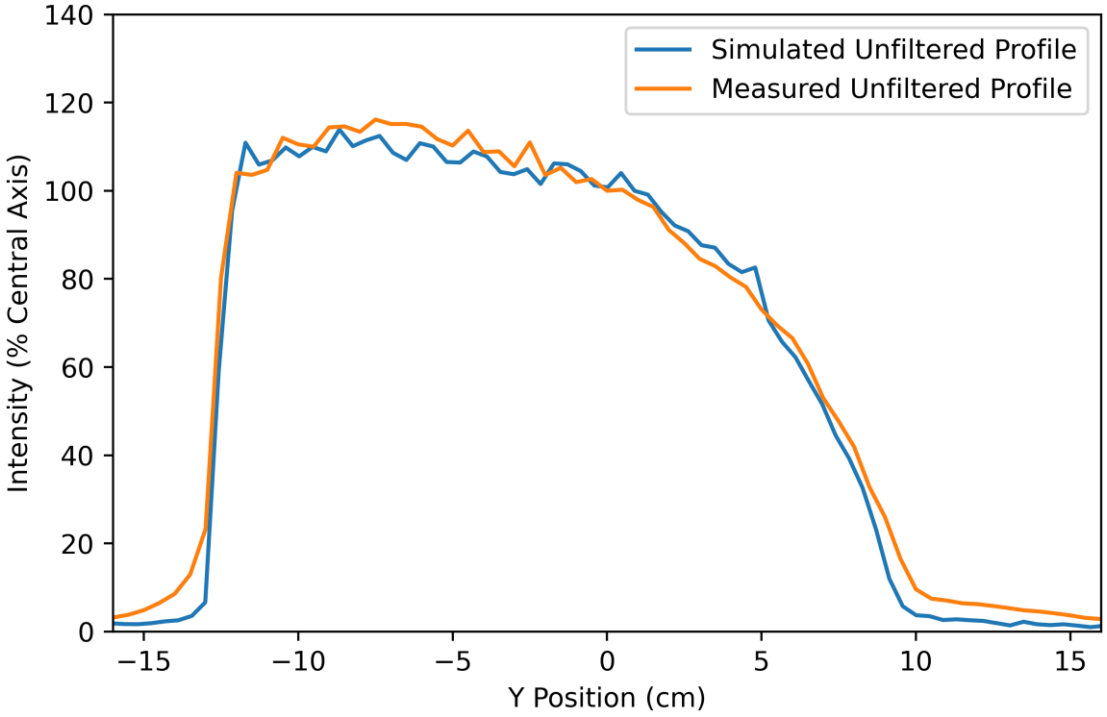

Figure 30. Simulated beam heel plotted versus the measured profile in the Y direction, parallel with the electron beam within the X-ray tube.

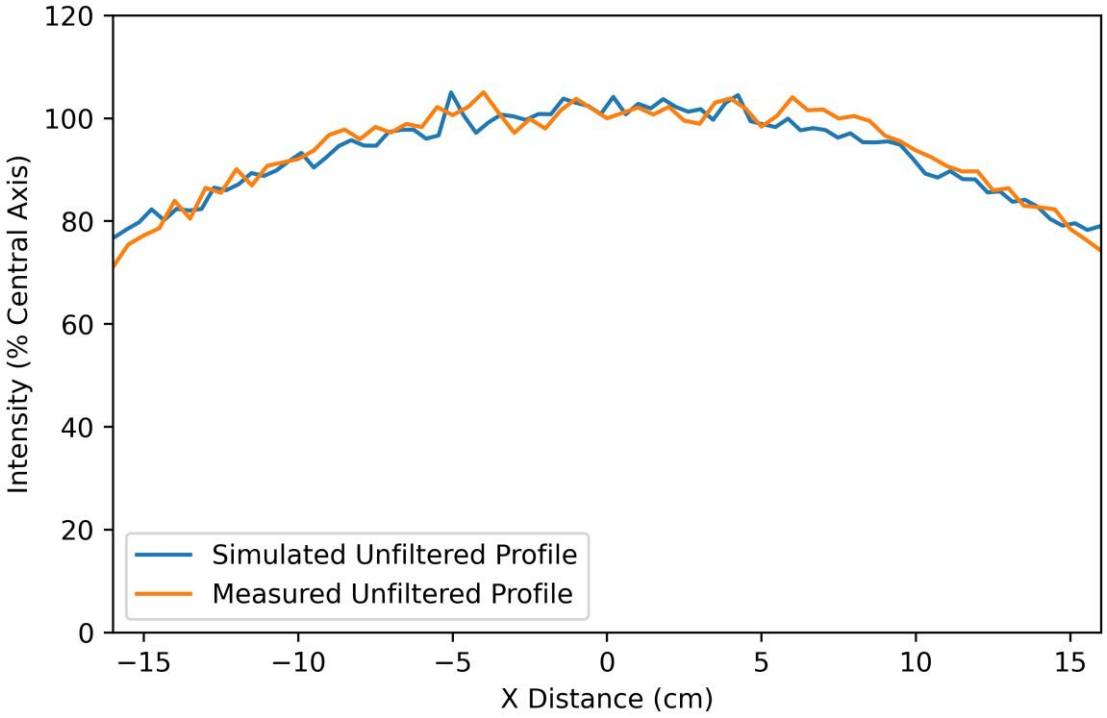

Figure 31. Simulated beam profile versus the measured profile in the X direction, perpendicular to the electron beam.

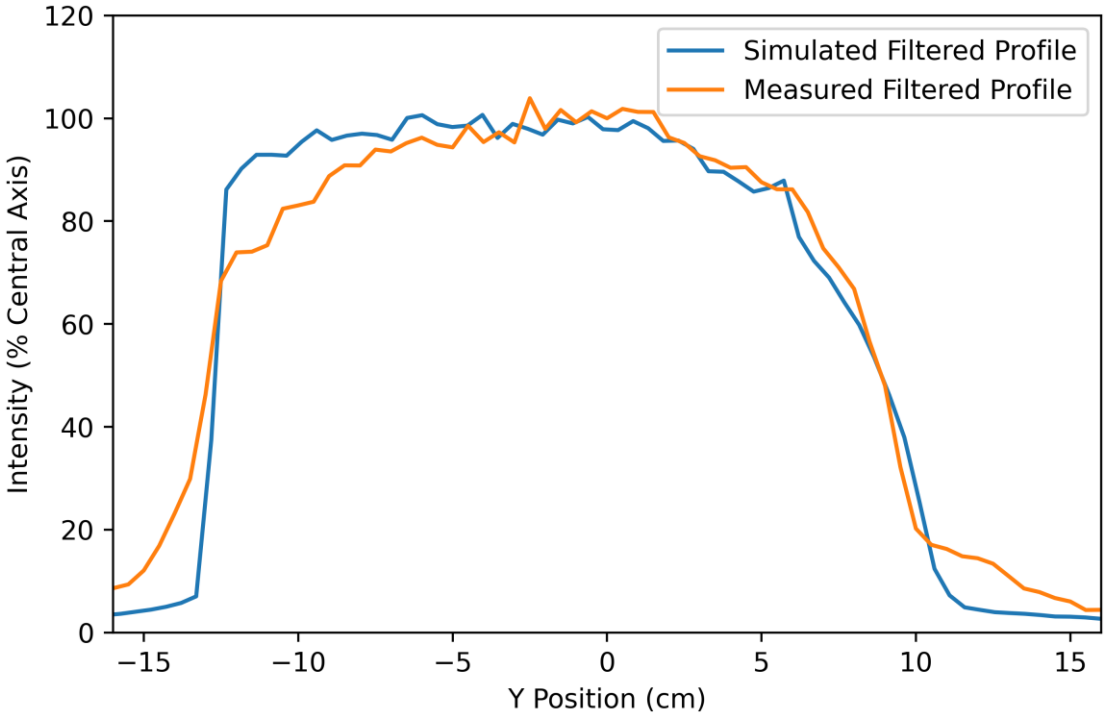

Figure 32. Simulated beam heel plotted versus the measured profile in the Y direction, parallel with the electron beam within the X-ray tube with the multilayer filter.

Figure 33. Simulated beam profile versus the measured profile in the X direction, perpendicular to the electron beam with the multilayer filter.

The unfiltered Y direction profile shows good agreement between the measured and simulated beam heel. This suggests that the normalization method between each 1-degree emission bin correctly adjusts the output intensity of the real beam. The same can be said for the X direction profile, closely matching the measured output intensity. There are no angular dependence differences in the X direction of the profile due to the physics of bremsstrahlung production relative to the electron beam direction. Because this profile is within the same angular distribution bin, the change in intensity towards the edges of the field can be attributed primarily to the r^2 relationship between the beam emission angle and the distance to the detector points on a flat plane. There is a small effect of X-ray path length differences through the target anode towards the edges of the field; however, these contribute much less to the profile shape than in the Y direction due to a much smaller emission angle with respect to the normal from the anode face.

The filtered X-ray profile in the X-axis shows good agreement, similar to the unfiltered X-ray profile. The Y profile shows good agreement on the beam heel, Y of 12 to Y of -5. From Y of -5 to Y of -13, the intensity of the simulated profile is 10 to 15 % higher than the measured profile. This slight difference is likely due to the filter implementation. The cadmium sheet used is not perfectly flat or uniform in thickness. It is possible that the filter is slightly thicker towards the back of the beam port, causing more attenuation. Precisely machined filter layers would likely smooth out this subtle reduction in intensity towards the back of the beam. These filter features are discussed in more detail in Chapter Six.

5.3 Percent Dose Depth Curve

Percent dose depth curves were also generated with the IC profiler and with layers of solid water to act as an analogous of human tissue. With MV beams, PDD curves are made with an ion chamber connected to a stepper motor inside of a water tank. However, this is impractical with our radiation enclosure. These measurements are made by exposing the profiler at an SSD of 35 cm, containing an intrinsic layer of 1 cm of solid water. The profiler is then stepped down in 1 cm or 2 cm increments to a total thickness of 7 cm of

solid water, as seen in Figure 34. By scaling the response of the central detector to the maximum dose rate at 1 cm and multiplying by 100, the PDD curve is normalized to 100 % along the central axis. These results are compared to the simulated results in Figure 35. The process is repeated with the filtered beam shown in Figure 36.

The simulated vs. measured PDD curves with the filter installed show the same general trends and match very closely. The slight variations are due to 2 cm solid water sheets being used instead of each cm, causing the measured curve to not be as smooth. Because the dose vs. depth of an orthovoltage X-ray system is a convolution of the flux and energy spectrum of the beam as it becomes attenuated through the body, the closeness of these two curves suggests that the nested cone model accurately simulates the X-ray beam as measured with the IC profiler.

The unfiltered PDD curve does not match as well as the filtered data. Since the filtered beam is hardened, there were very few photons below ~60 keV, as seen in Figure 28. This energy difference suggests that the response of the IC profiler changes depending on the mean energy distribution and becomes more linear with higher energy X-rays. The *FMESH method of generation PDD curves assumes a 100% efficient detection efficiency and linearity across all energies making the curve flatter. The response of the ion chambers within the profiler is likely non-linear across the lower energy range. This non-linear response is discussed later.

5.4 NanoDot Verification

The results gathered with the IC Profiler are valuable in determining the beam model profile accuracy. However, the IC Profiler response is not calibrated and does not report the true dose rate. The IC Profiler only provides the relative exposure rate across its active sensing area. In order to calibrate these values to a real dose rate, Landauer nanoDot optically stimulated luminescence (OSL) dosimeters were selected, which are composed of aluminum oxide with a carbon dopant (Al_2O_3:C). These devices trap charge emitted by radiation interactions within the aluminum oxide. The charge trapped is proportional to the energy deposited, which is proportional to the dose.

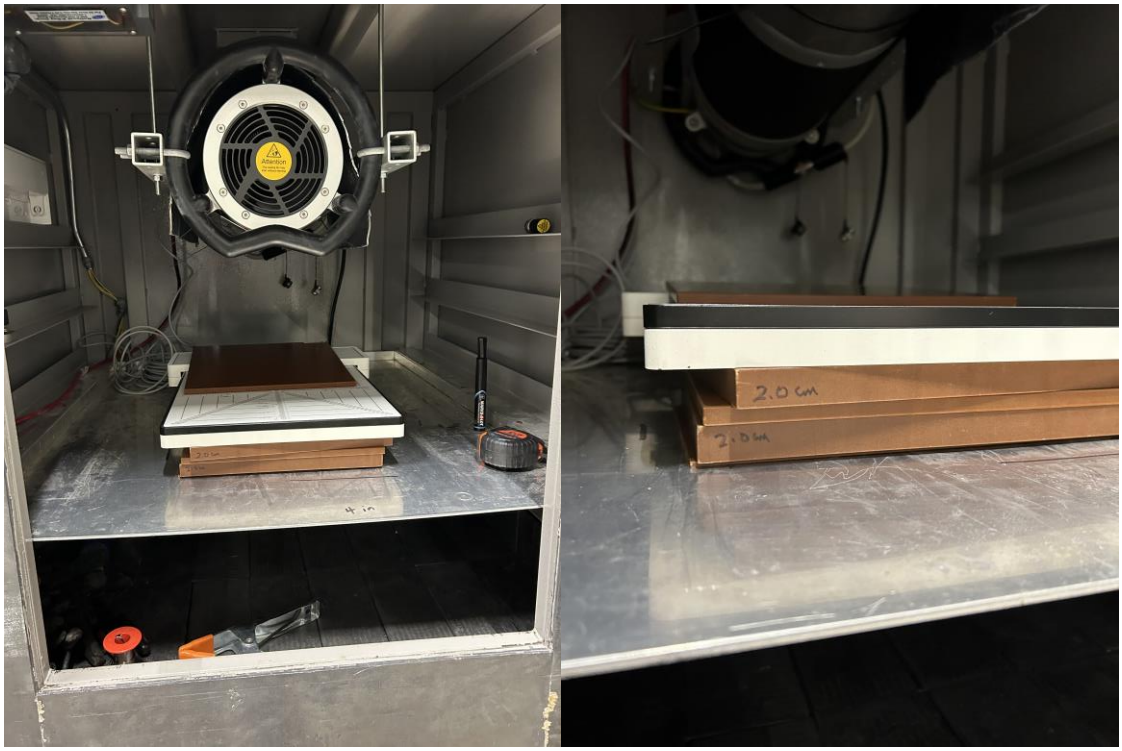

Figure 34. Picture showing the IC profiler location for field profile measurements and 7 cm of solid water (brown squares) used to produce the PDD curve by stacking each layer on the front face. The SSD to the surface of the solid water is held constant at 35 cm.

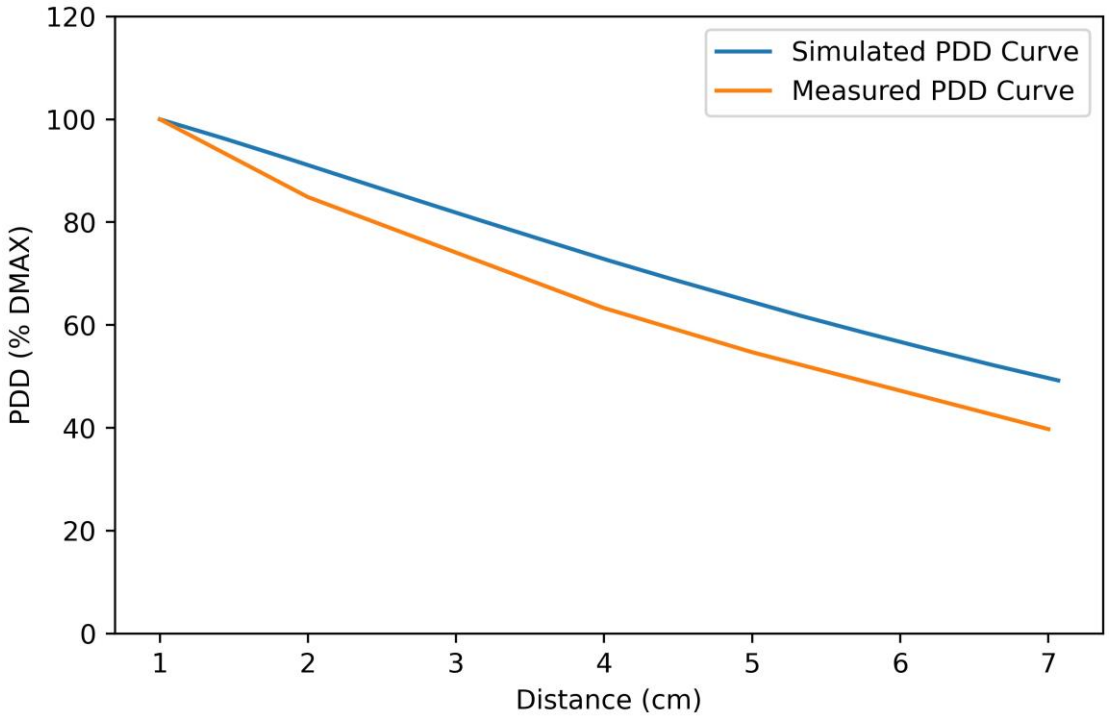

Figure 35. Unfiltered PDD curve comparing the simulated dose deposition within PMMA plastic to the measured response with 1,2,4,5 and 7 cm of PMMA plastic with the IC profiler. The non-uniform solid water thicknesses are due to some pieces being 2 cm thick. The different response with depth is likely due to the different response of the ion chambers of the IC Profiler as the unfiltered beam becomes hardened in the solid water.

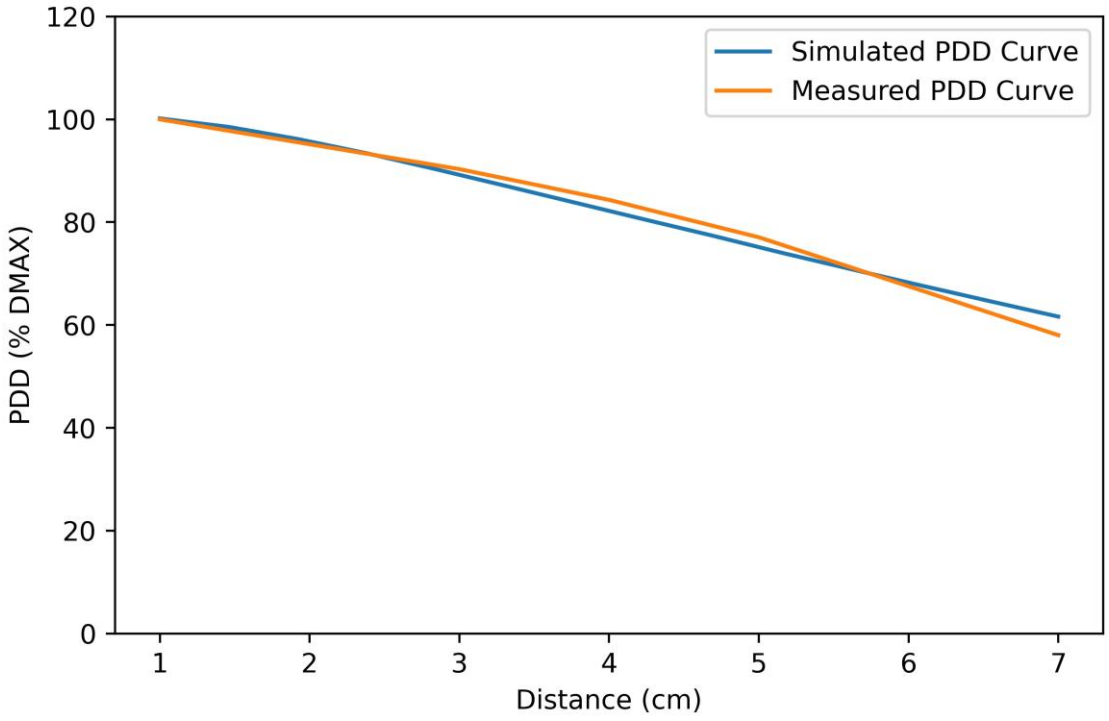

Figure 36. Filtered PDD curve comparing the simulated dose deposition within PMMA plastic to the measured response with 1,2,4,5 and 7 cm of PMMA plastic with the IC profiler. The non-uniform solid water thicknesses are due to some pieces being 2 cm thick. This could be the reason for the nonlinearity of the measured PDD curve from 2 to 5 cm.

Landauer Special Services offers calibrated readout standards for nanoDots where the trapped charges are released, counted, and a calibration standard is applied depending on the radiation environment. The standard chosen for this experiment is the CT, 120 kVp, 8.3 mm Al HVL because our system is a poly energetic bremsstrahlung spectrum device, the same as the X-ray tubes used in a CT scanner. However, the peak energy of our orthovoltage tube is nearly double at 300 kVp, which has some effects on the true calibration of the X-ray tube dose rate.

The linearity of the dose rate with time is measured with and without 1 cm of buildup (solid water) at 35 cm SSD. This is done with the ramp time (time to reach full energy and current), which is about 10 seconds, then time intervals of 30, 60, 90, 120, 150, and 180 seconds. Figure 37 shows the dose rate versus time for an unfiltered beam and again with 1 cm of solid water as a buildup layer in front of the nanoDot. The dose at t=0 is non-zero and represents the dose accumulated during the tube ramp to operational energy. The dose rate vs. time for the unfiltered beam, with no buildup layer, shows a linear response with some slight deviation at 30 seconds and again at 120 seconds. The deviation can be attributed to non-proportional energy response or trapping within the dosimeter. There is also an inherent error with these devices reported as 10% of the actual dose, which could cause this deviation. The device is reported to be linear for medical dosimetry applications up to 300 cGy. The dose response with the buildup layer shows a more linear trend but with a cumulative dose of about half that of the no-buildup experiment. This is due to the poly energetic bremsstrahlung spectrum, which is a majority low-energy X-rays. The buildup layer behaves as an X-ray filter for many of these low-energy X-rays reducing the dose rate response with time. Another nanoDot is exposed with the X-ray filter, and no buildup for 30 seconds.

For dosimetry comparison between the simulations and the experimental data, the nanoDot is also modeled in MCNP with the nested cone bremsstrahlung simulation and the nested cone photon simulation as a method of validating the simulated beam output between the different simulations. The nanoDot is modeled according to the specifications given by Landauer, a roughly 1 mm thick cylinder with a diameter of 5 mm.

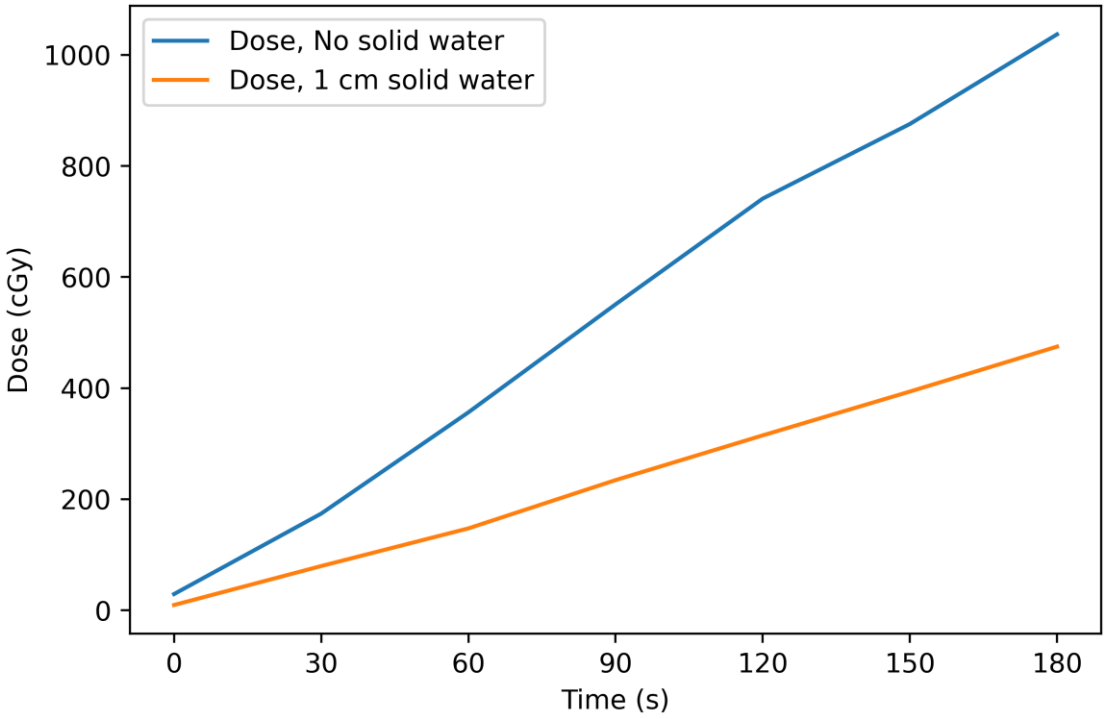

Figure 37. Dose versus time given 1 cm of solid water buildup and without solid water buildup. The trend suggests that the dose-response with buildup is very linear with time. The non-zero dose value at t=0 is due to the tube ramp and contributed 29.2 and 9.4 cGy of dose to the measurement of the without buildup and with buildup curves, respectively.

The material is simulated as Al_2O_3 and given a density of 3.95 g/cm^3, typical of aluminum oxide. This is placed at an SSD of 35 cm with and without a filter and 4 cm of buildup behind the nanoDot. No buildup is placed in front of the beam.

The nanoDot is then tracked with an F6 tally and converted to dose per second in cGy. The unfiltered simulated dose rate is 12.2 cGy/s, while the nanoDot reported a dose rate of 4.8 cGy/s, a factor of approximately 2.5 times lower. The filtered simulation reported a dose rate of 1 cGy/s, while the nanoDot reported a dose of 0.247 cGy/s, ~4 times lower. This trend of nanoDots reporting doses approximately 2.5 to 4 times lower is seen in other experimental results discussed in Chapter Seven. Upon evaluation, two possible reasons exist for these rather large discrepancies: a scaling factor in the simulations over-reporting the dose per electron or the calibration standard applied to the nanoDots underreports the true dose delivered.

The output of the bremsstrahlung nested cone experiment is scaled according to the manufacturer's reported tube current, 3 mA times the number of electrons per coulomb, 6.24×10^{18} electrons, to get the photon dose per second. The discrepancy between the nanoDot and simulation is about 2.5 times. In order to scale the dose rate with the photon-only simulation, with and without the filter, the tube current and number of electrons per coulomb are scaled according to the ratio of electron dose to photon dose to account for the bremsstrahlung production factor. For the unfiltered bremsstrahlung nested cone simulation and the unfiltered photon rings simulation, this gives a dose rate of 12.2 cGy/s. This suggests that the scaling factor between the two simulations is correct since they give the same dose rate. With the filtered simulation, with the same scaling factor as the photon rings simulation, the dose rate is 1 cGy/s. This value is approximately 4 times higher than the experimentally measured nanoDot.

The larger discrepancy with the filtered data suggests that the hardening of the spectra above 100 keV, seen in Figure 38 and Figure 39, would cause differences in the photon interactions within the nanoDot. In the unfiltered spectrum, the average photon energy is 83 keV. Below 40 keV, the probability of photoelectric interaction is greater than Compton scattering. A significant portion of photons are below 40 keV, so there will be a considerable number of photons that undergo photoelectric interactions prior to scattering.

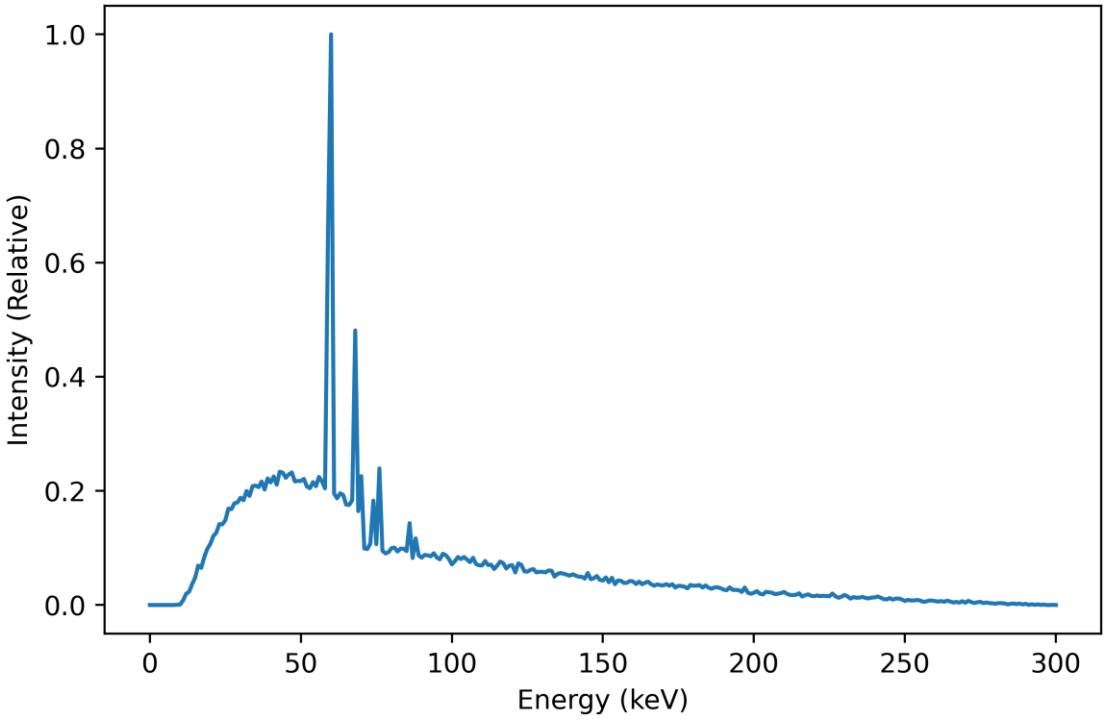

Figure 38. Unfiltered 300 kVp X-ray spectrum with an average X-ray energy of 83 keV. The spikes between 50 and 80 keV are due to K and L shell X-rays from the tungsten target.

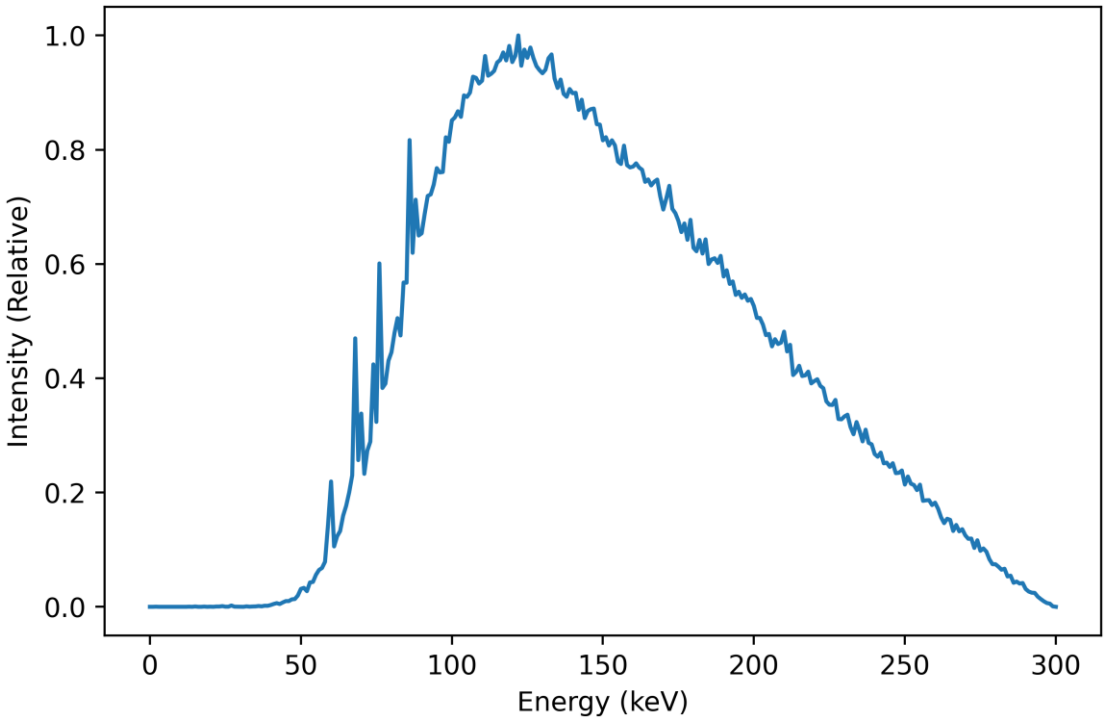

Figure 39. The filtered 300 kVp output spectrum normalized to 1. The filter near blocks out all X-rays below 50 keV and raises the average X-ray energy to 151 keV at a much lower overall intensity.

However, most of the spectrum is above 40 keV, where Compton scattering is more likely to occur prior to photoelectric absorption. At the average energy of 83 keV, the probability of photoelectric vs. Compton interaction is reduced to approximately 0.15. The region of the spectrum below 40 keV is almost completely removed in the filtered spectrum and the lowest energy photon is about 50 keV. At this energy, the ratio of photoelectric to Compton interaction is 0.68, showing that Compton scattering is more likely than photoelectric absorption. At the average photon energy of 151 keV, this ratio is reduced to 0.004. This shows that the ratio of photoelectric to Compton scattering reduces dramatically as energy increases, especially at the average photon energy and above.

With an average beam energy of ~151 keV, the filtered beam has higher average energy than the peak energy of the 120 kVp CT calibration tube. The average energy of the CT standard is between 40 and 60 keV (depending on filtration), which, as previously discussed, has a high probability of photoelectric interaction. It is even higher than the unfiltered 300 kVp spectrum due to the much lower average energy. This suggests the under-response of the calibrated nanoDots with the 300 kVp X-ray source is due to the over-representation of the photoelectric interactions in the calibration standard when compared to the 300 keV X-ray tube. This is supported by the energy response curves supplied by Landauer, which show a response of about 1/2-1/3 in the 120 to 300 keV range.

The PDD data in Section 5.3 also revealed different detector responses concerning the mean spectral energy. The PDD curves for the filtered simulation and measured data matched very closely, likely due to the high (~150 keV) average energy of the spectra being more penetrating and highly dominated by Compton scatter, not photoelectric interaction. The Unfiltered PDD curve showed a sharp falloff in the measured dose in the first few centimeters matching the slope of the simulated data. This difference suggests that the ratio of photoelectric to Compton events in the ion chambers while measuring the PDD curve can cause a non-linear response with depth. The overresponse to a lower average energy beam would suggest that the nanoDots calibrated with 120 kV CT beam would report a lower than expected dose when exposed to a majority higher energy beam.

CHAPTER SIX
IMAGING

6.1 Field Imaging

X-ray imaging with a digital radiography panel is another method of determining the field profile. Imaging also conveys information about the filter design and collimator edges when looking at images of the raw beam. These images also allow for better alignment of the phantom for exposure experiments. The Varex 4343HE flat panel detector in Figure 40 is an industrial radiography panel with a wide energy range (20 kV – 16 MV) made of amorphous silicon. The total pixel area is 42.7 by 42.7 cm with a pixel matrix of 3,072 by 3,072 and a pixel pitch of 139 μm^2.

In order to create quality radiographic images with a new X-ray tube that has not been characterized, a few steps must be taken to improve the image quality and remove noise from the system. First, we must understand the contribution of signal to each pixel prior to X-ray exposure. This is achieved by taking a dark field image. With a frame rate of 1 fps, the panel recorded 100 images with the X-ray tube off. This gives 100 dark field images. The intensity value at each pixel is averaged for all 100 frames. The resultant image in Figure 41 shows the average pixel value due to background radiation, but mostly electronic noise and other intrinsic signals generated within the detector panel itself.

After collecting this data, a flood field or bright field image is taken. With no object in front of the panel, this image records the maximum value of each pixel and is used to ensure the dynamic range of the panel is high enough so that no pixel data is lost or "clipped." Again, 100 images are averaged to create the image. The flood field shows a reduction in intensity toward the imaging plate's periphery due to the X-ray field's shape and the $1/r^2$ relationship of X-ray flux. This is conducted at 120 kVp, 3 mA, and 300 kVp 0.5 mA and can be seen in Figure 42 and Figure 43. These images show areas of changing attenuation, most prominently in the top left corner that looks like ripples of fabric. This is due to the cadmium sheet used in the filter's construction.

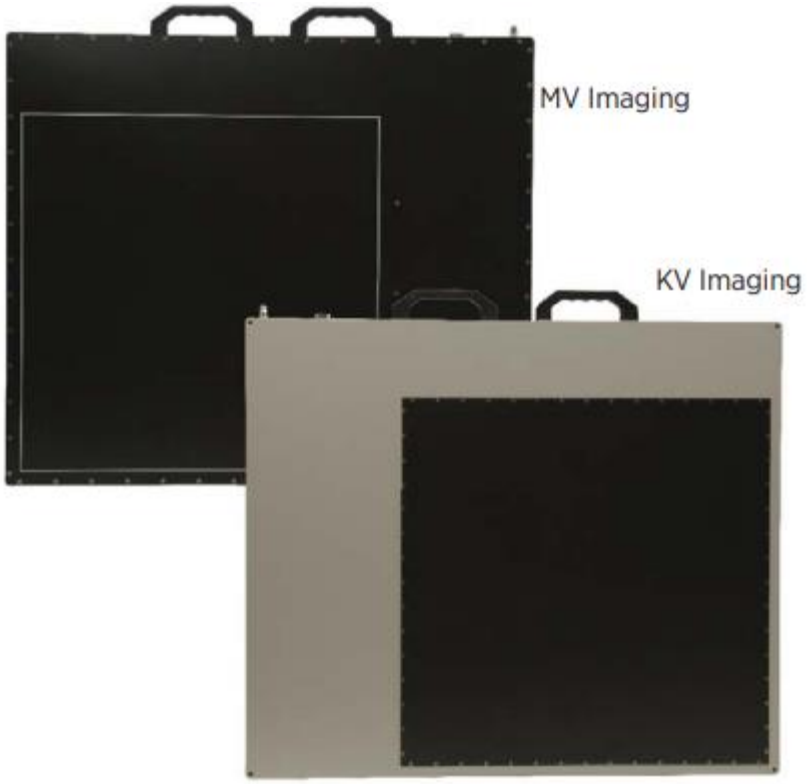

Figure 40. Varex 4343HE industrial imaging plate. Each side can be used for different energy ranges and contain different amounts of material for buildup. For kV imaging, the smaller black square region is used.

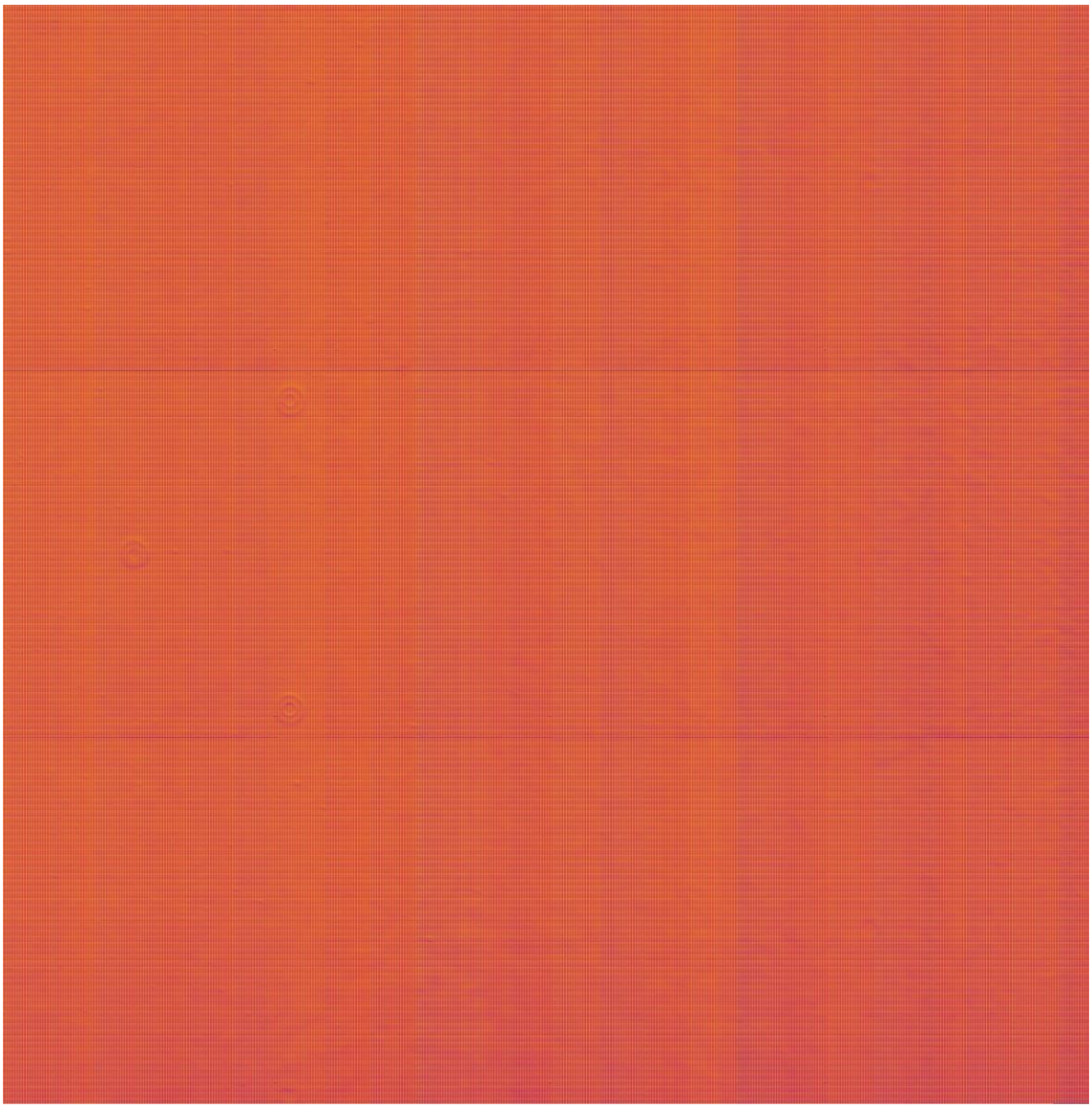

Figure 41. A dark field image of the 4343HE panel averaged across 100 images. This image is taken without exposure to the X-ray beam to determine each pixel's associated electronic and background signal. The image is windowed, and a fire color scale is applied to highlight the local differences and some of the structures inherent to the plate construction.

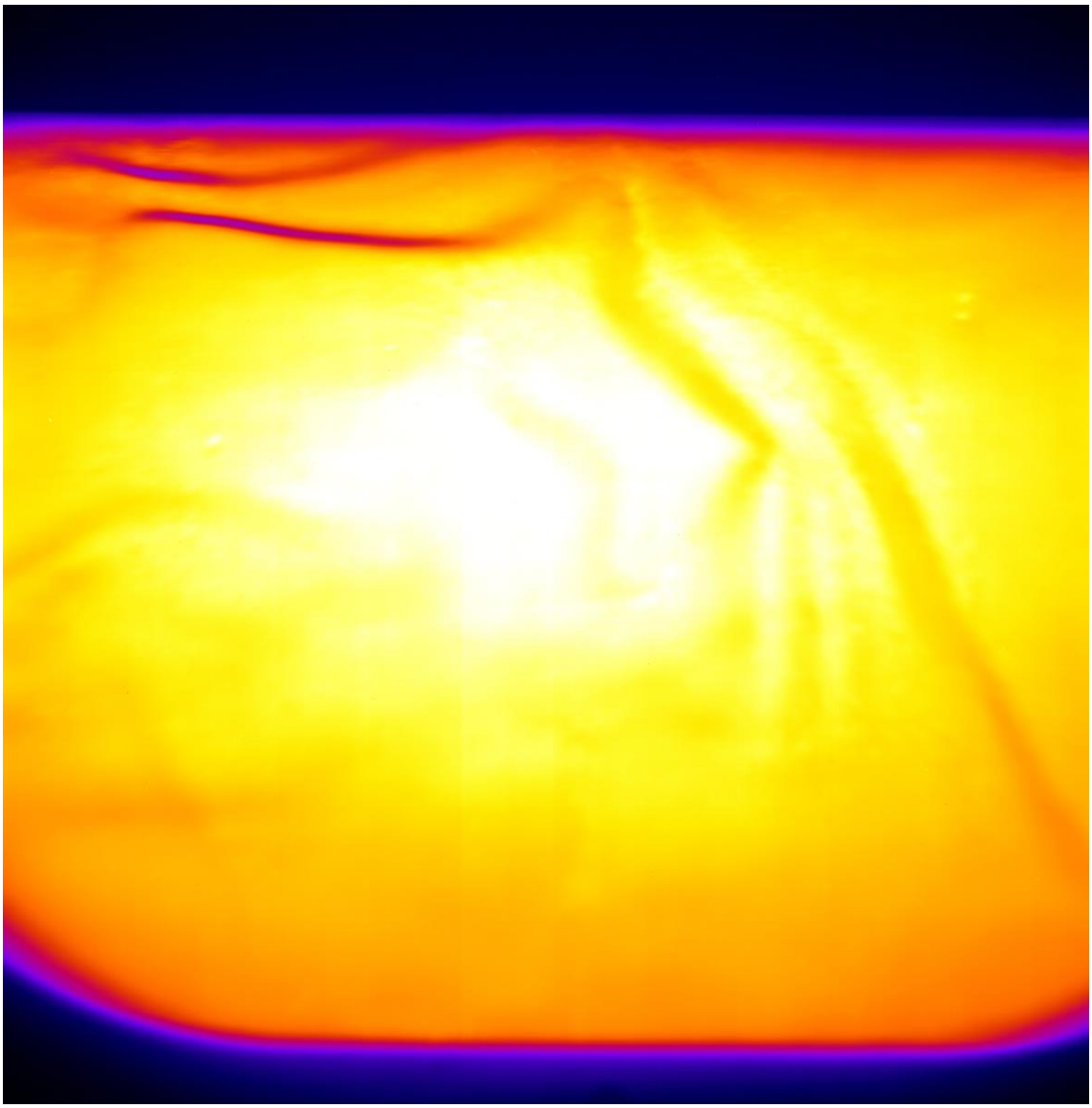

Figure 42. A bright field image with the 4343HE at 120 kVp and 3 mA of tube current. This image is used to correct the different intensities across the imaging plate and to ensure that the maximum signal output is not higher than the dynamic range of the detector plate.

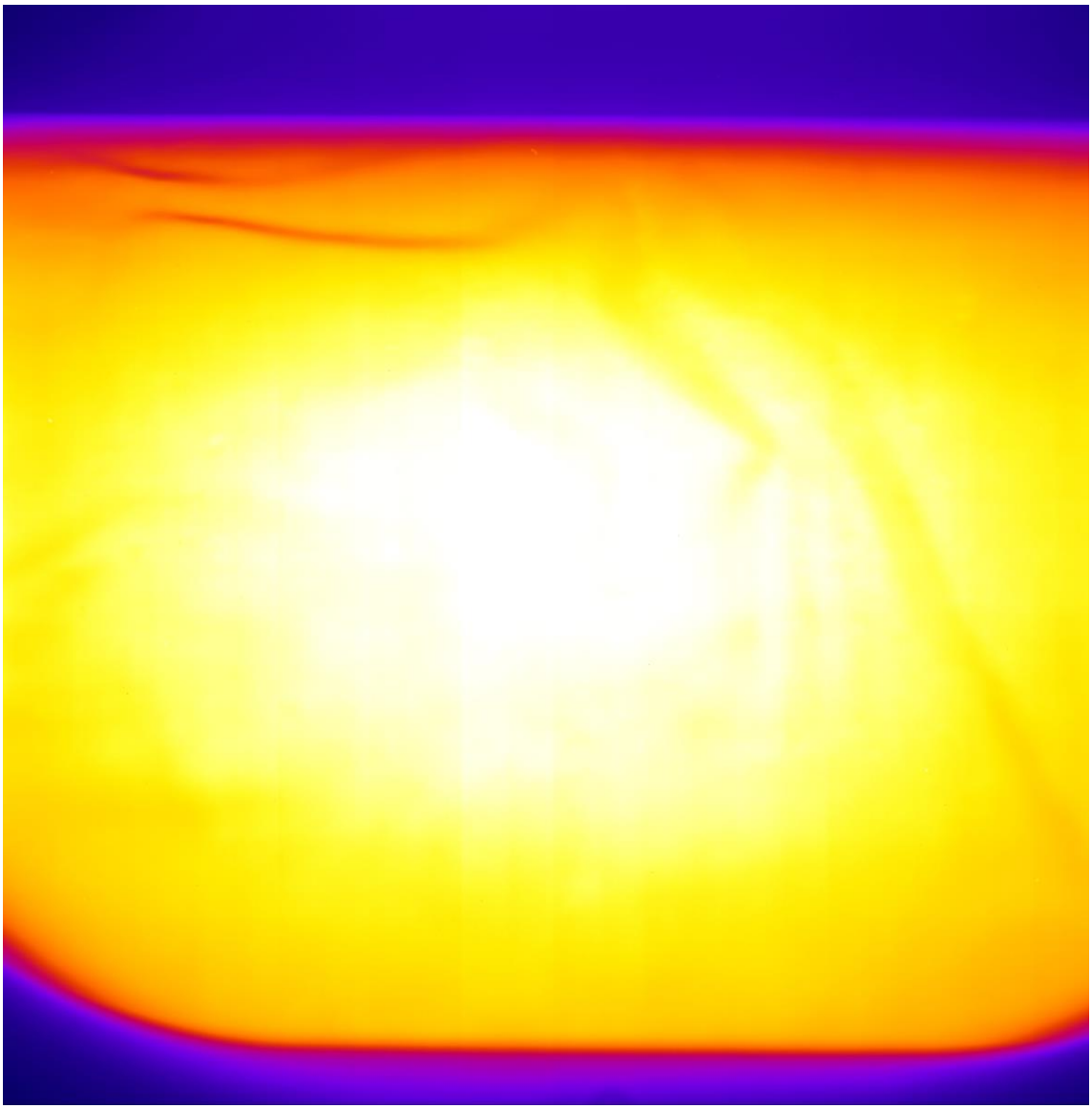

Figure 43. Another bright field image at 300 kVp and 3 mA of current. Like Figure 42, this is to ensure the dynamic range of the imaging plate does not lose data from the highest intensity areas of the field, as seen in the center of this image.

The cadmium sheet is not smooth and contained ripples which caused areas of higher attenuation due to increased local thickness. These features are present in all of the subsequent images. Line profiles also show the X-ray profile in the axial direction to see the dynamic range of the output. The 120 kVp line profile in Figure 44 shows the range to be ~16,000 with no clipping. The lower tube current of 0.5 mA at 300 kVp is chosen so that the pixel values stay within the maximum ~64,000 dynamic range of the panel, seen in Figure 45. The slight reduction in intensity towards the back of the filter is present in the line profiles and the flood field images, which match the IC PROFILER profiles.

6.2 Phantom Imaging

The RSD phantom is placed inside the radiation enclosure and suspended with wood strips ~1 inch above the front surface of the imaging plate. This is to ensure that the weight of the phantom would not cause damage to the internals of the imaging plate. Images were taken at the same energy and tube current as discussed previously, 120 kVp @ 3 mA and 300 kVp @ 0.5 mA. Again, 100 images at each energy are averaged, creating a single composite image.

To improve the image contrast, the background average is subtracted from the image average to remove any intrinsic signal contribution from the final image. However, this does not account for the different intensities of the raw signal at each pixel. As previously shown in Figure 42 and Figure 43, the intensity is highest in the center of the field and decreases towards the edges. This is corrected by scaling the intensity of the image with the background-corrected bright field. This correction is described in Equation 14.

$$Scaled\ Image = \ln\left(\frac{average\ image - background\ image}{bright\ feild - background\ image}\right) \quad (14)$$

The scaled image is the natural log of the difference between the averaged image and the background or dark field image divided by the difference between the bright and background images.

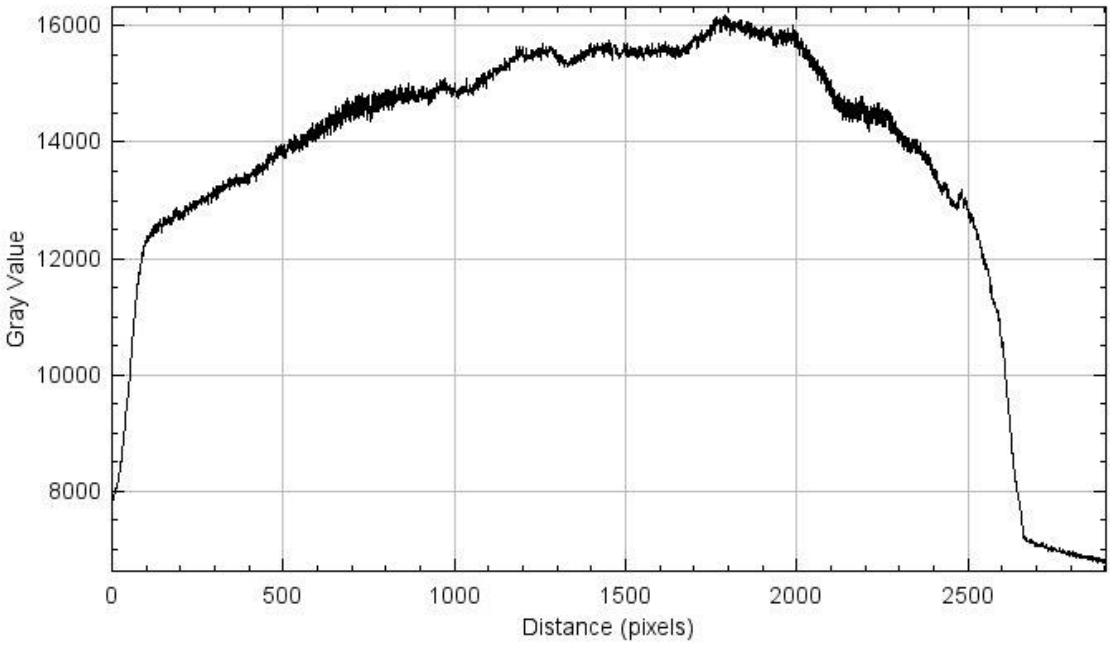

Figure 44. A line profile is taken from the center of Figure 42 to show the relative intensity along the central axis. This profile shows that the dynamic range of the panel is adequate not to lose signal intensity or “clip” the pixel data with the highest output.

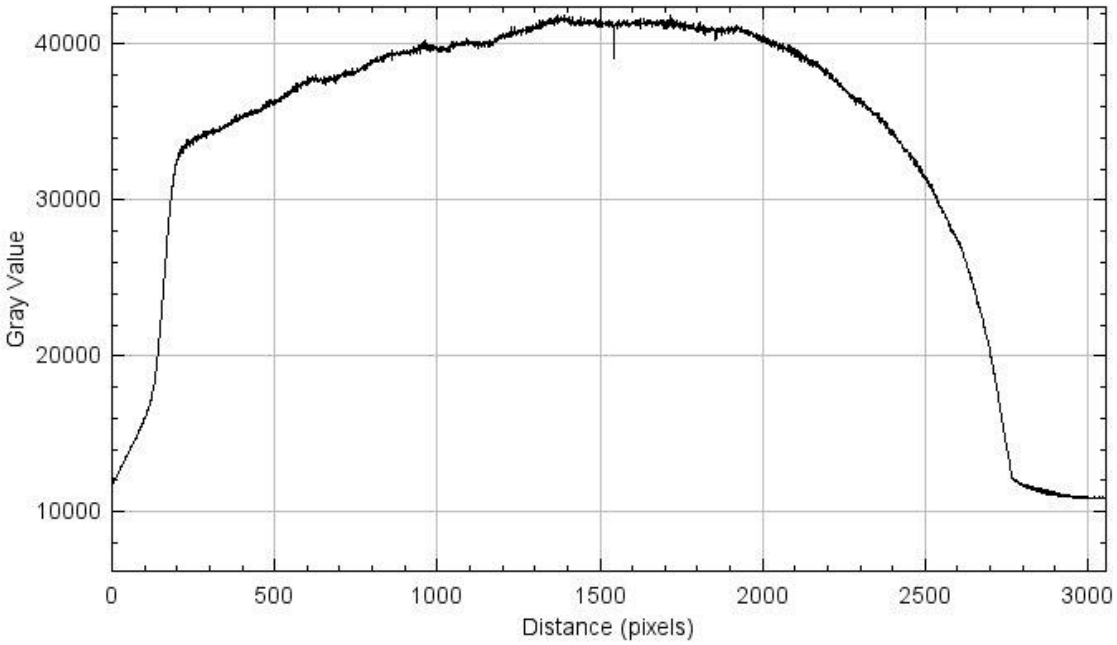

Figure 45. A line profile of the central axis of Figure 43. This shows that the bright field's relative intensity is within the imaging plate's dynamic range. Notice the much higher intensity of the 300 kVp field of ~40,000 compared to ~16,000 of the 120 kVp fields in Figure 42.

By dividing the corrected image by the corrected bright field and taking the natural log, the scaled image is proportional to the attenuation along the path to that pixel location. The average and scaled images at 120 kVp and 300 kVp can be seen in Figure 46 and Figure 47, respectively. The horizontal line in all images is due to how the phantom is constructed. The layers were slightly separated, leading to a horizontal line with minimal attenuation. The cadmium filter feature is also present. At 120 kVp, it shows up much lighter than the surrounding material and suggests that the attenuation correction does increase the differentiation of this dense feature compared to its surroundings. At 300 kVp, the cadmium feature is still noticeable but much less differentiated than its surroundings. The average beam energy of the 120 kVp beam is estimated to be between 70 and 80 keV, whereas, with the 300 kVp beam, the average is 151 keV. The higher average energy of the spectrum would cause less attenuation and would be less reliant on differences in the Z number. This explains why the entire image shows less contrast when compared to the 120 kVp images. This lower average beam energy is firmly in the diagnostic range where attenuation differences between human tissue Z numbers are maximized. This is why the cadmium feature with a higher density and Z number stands out greatly at 120 kVp.

In order to compare the images taken at different energies, the window and leveling of each image are changed independently to improve the features that can be distinguished visually. The color scale is also inverted so that bony features would appear white to resemble a traditional X-ray image more closely. These changes visually improved both images; however, the 300 kVp image seems slightly more blurred and with less overall contrast. This difference is expected since diagnostic X-ray energies do not exceed 150 kVp.

Overall the image quality of the Comet EVO300D is better than expected. This X-ray tube is marketed as an industrial radiography device, but diagnostic imaging has a few key differences. Usually, with a purpose-built X-ray system for diagnostic imaging, the focal spot size on the anode is small, usually less than 1 mm. This ensures that the X-rays are generated in a small area, and as they diverge, their path lengths overlap as little as possible. This improves the sharpness and quality of the final image.

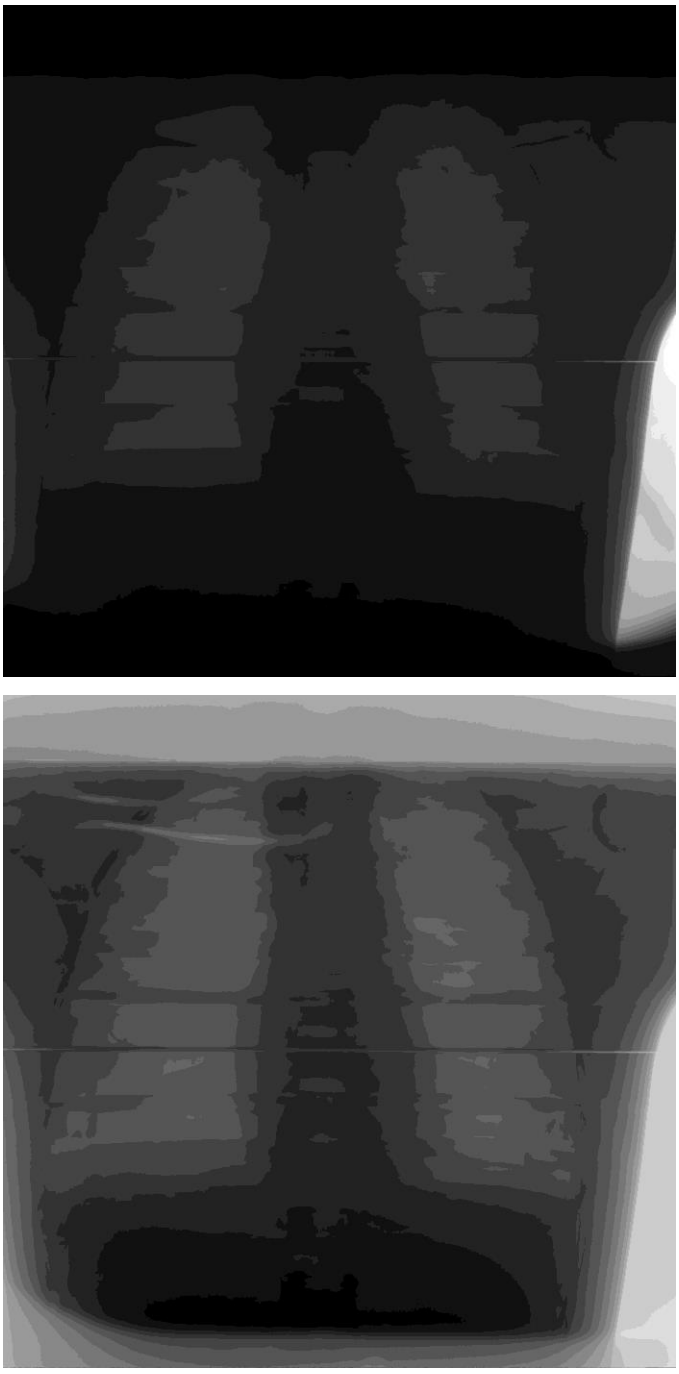

Figure 46. A comparison of the image average on the top with the attenuation-corrected image on the bottom at 120 kVp. The attenuation-corrected image shows a more uniform contrast and better differentiation, especially toward the edges of the field.

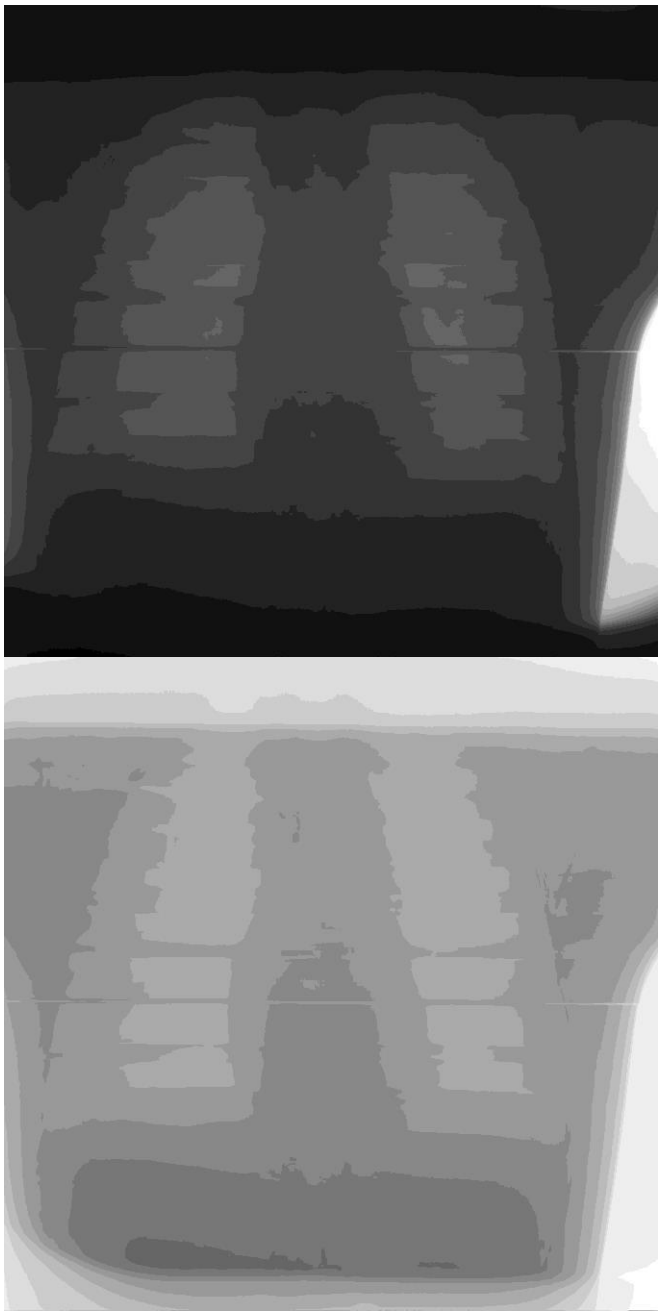

Figure 47. A comparison of the image average on the top with the attenuation-corrected image on the bottom at 300 kVp. The same trends as the 120 keV corrected image. The attenuation-corrected image is more washed out than the 120 keV images suggesting that the higher energy X-rays are less attenuated through the body resulting in less contrast.

With this X-ray tube, the focal spot size is 4 mm, by medical imaging standards quite large. This limits the resolution obtainable by this system. Another detractor is the proximity at which the source, object, and imaging panel are located. The source-detector distance for a typical chest X-ray is around 6 ft or 1.8 m. With an SSD of 35 cm and a source-detector-distance of ~50 cm, there is substantially more beam divergence along the path length than a typical imaging system. This is noticeable in the uncorrected images where the perimeter of the image is darker than the center where the intensity is highest. The attenuation correction removes most of the $1/r^2$ dependence due to path length differences; however, the longer attenuation path through the body cannot be accounted for at larger angles and is a source of error and blurring in the image. This issue is apparent in the layers between each RSD phantom section in Figure 48 and Figure 49. The horizontal line in the center of the image appears to run perpendicular with very little width. Above and below this line, the visible lines separating each layer of the phantom appear more oblique as the distance from the isocenter increases.

These images show that even with an X-ray source with less-than-ideal medical imaging features, it is still possible to produce high-quality images. The large spot size, close SSD, and short source-detector-distance do introduce some artifacts and issues with the image quality. This setup may not have the quality necessary for diagnostic imaging; however, the image quality is more than adequate for patient set-up and alignment for identifying structures of interest. The upper and lower bounds of the lungs and the width of the ribcage are important to identify and align in the field. From these images alone, we found that the lung's estimated isocenter is lower than the true isocenter. This resulted in the upper pinnacle of each lung being cut off by the collimator and not included in the field. Due to this imaging study, we found that the true isocenter should be moved about two inches higher for the phantom dosimetry experiment.

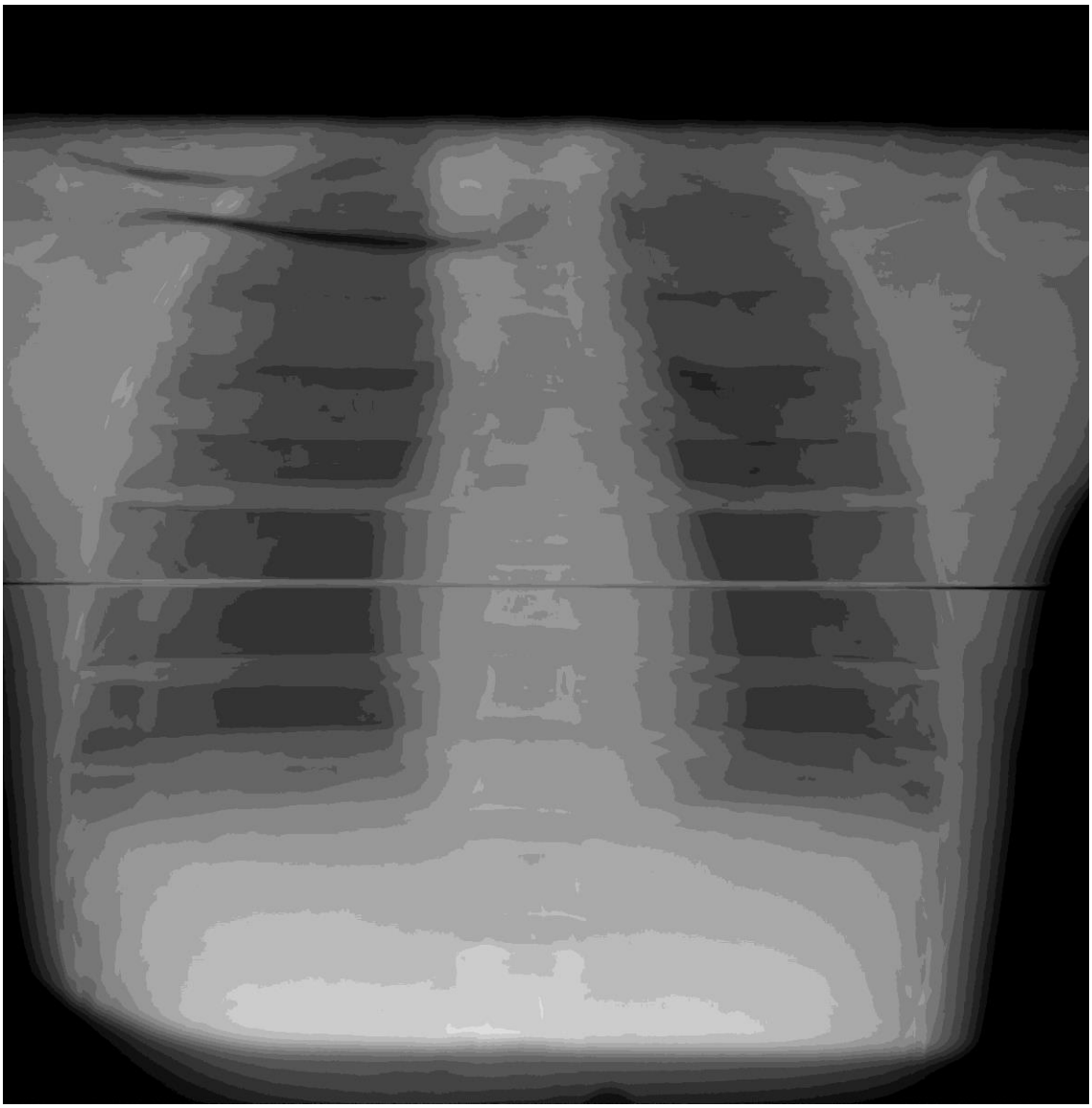

Figure 48. 120 kVp attenuation corrected image with the color scale inverted to show bony features (higher density) in white. The window and level is set to show the best contrast in the phantom visually. The cadmium feature in the top left appears dark because the value in this region is above the window threshold.

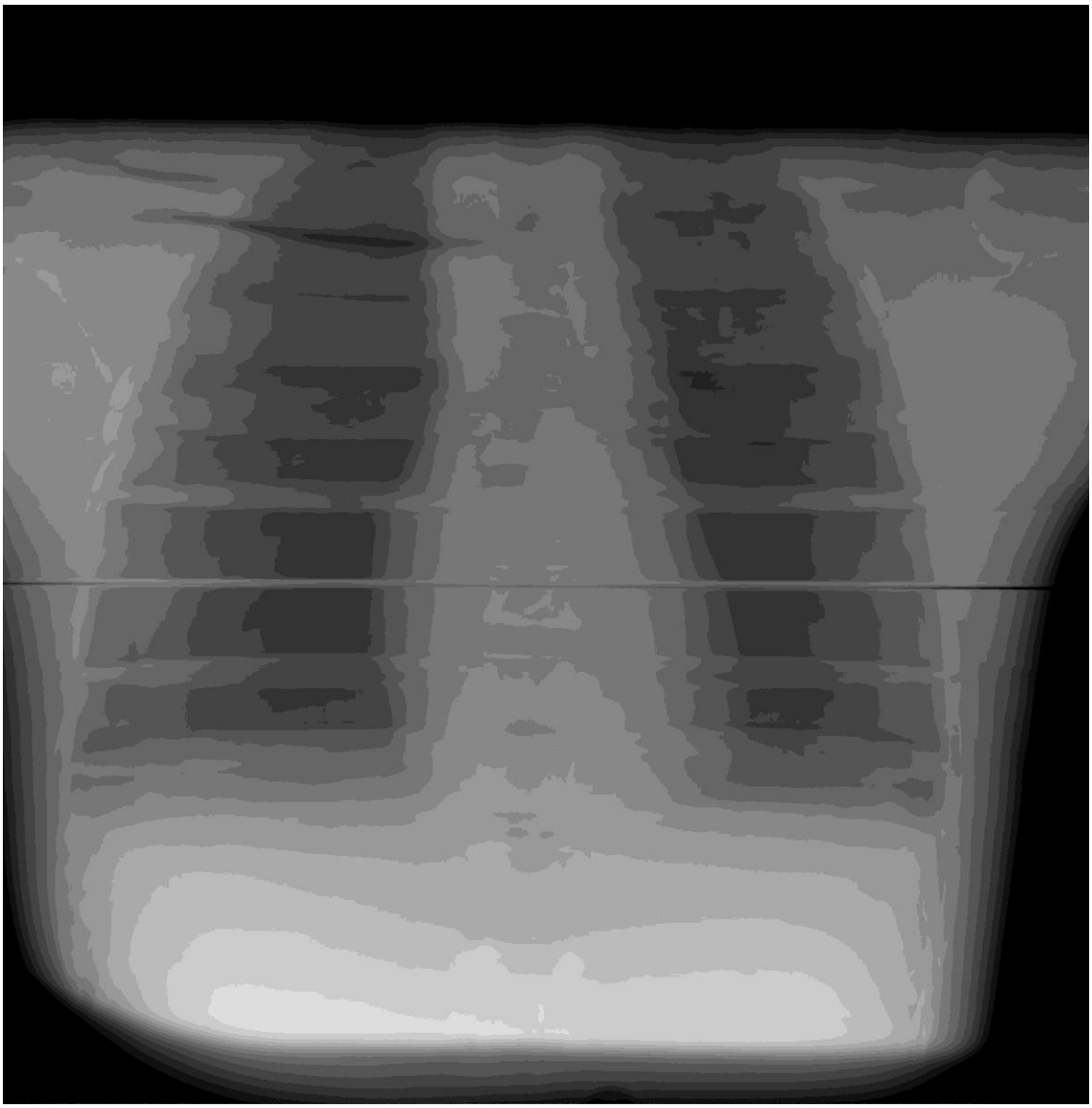

Figure 49. 300 kVp attenuation corrected image with the color scale inverted to show bony features (higher density) in white. The window and level is set to show the best contrast in the phantom visually, like in Figure 48. The cadmium feature and the image show less contrast due to the higher energy and fewer attenuation differences for different Z-number materials.

CHAPTER SEVEN
PHANTOM DOSIMETRY

7.1. In-situ Dosimetry

Experimental verification of the dose delivered with the COMET EVO300D X-ray tube is carried out using the RSD phantom seen in Figure 50. Landauer nanoDots are again used and the dosimeter locations within the phantom are chosen to show the dose uniformity of the lungs and the dose to other regions of interest. This includes the skin, heart, thyroid, and spine, as well as out-of-field dose rates. To accurately convey the location of the dosimeters, a CT scan of the phantom was conducted at the University of Tennessee Medical Center before inserting the nanoDots. The Philips CT scanner used is equipped with a flat, carbon fiber couch as this machine is used for CT simulations for radiotherapy. The output CT is a 512 by 512 voxel array with 320, 4 mm slices in the axial direction, and the scan be seen in Figure 51.

The nanoDots were placed into the phantom using a Dremel to cut a slot the same dimensions as the dosimeter. They were placed in the slot and covered with a small piece of masking tape to ensure they did not move when the phantom layers were reassembled, shown in Figure 52. To determine the skin dose, masking tape is used to attach dosimeters to the surface of the phantom at other key locations like the surface under the isocenter, the left and right sides, the surface of the trachea, and one on the surface of the abdomen just outside of the X-ray field. Another nanoDot is placed on the backside at the isocenter. The location of each dosimeter can be seen in Figure 53, Figure 54, Figure 55, Figure 56, Figure 57, Figure 58, and Figure 59. These images also report the nanoDot dose rate in cGy/s.

The cone beam modeling in Chapter Three suggested that the field weighting should be higher with the PA beam than with the AP beam. In the exposure study, we elected to weight each field, AP and PA, equally to understand how the dose is distributed without other variables such as weighting.

Figure 50. Images of the Radiology Support Devices phantom placed on the couch of a Varian TrueBeam linac. The cone beam CT was used to take radiographs of the phantom for comparison with the 300 keV X-ray tube imaging.

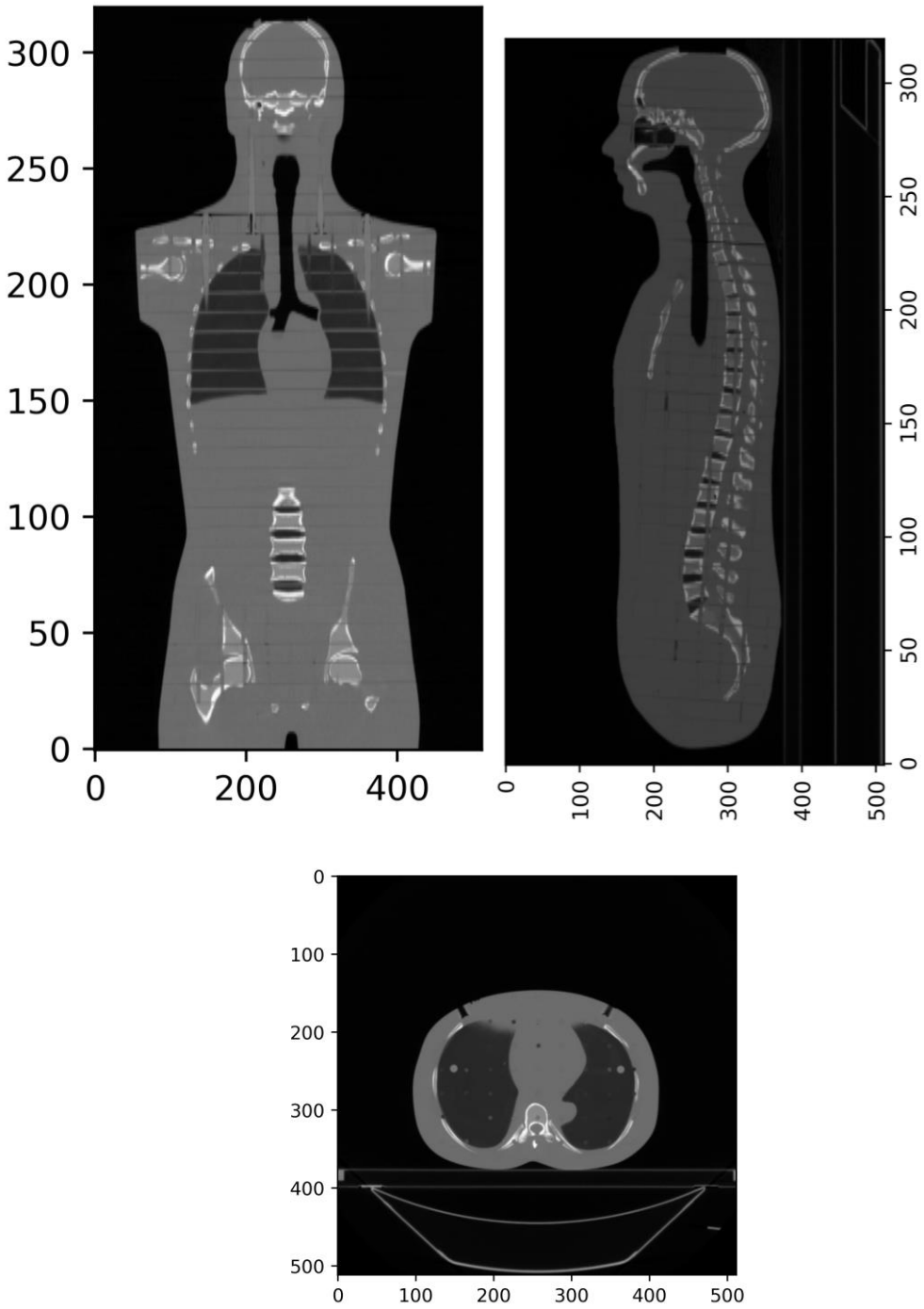

Figure 51. The phantom's axial, sagittal, and coronal images show different lung, bone, heart, and trachea tissues. This is used to show the location of the nanoDot dosimeters.

Figure 52. A cross-sectional layer of the RSD phantom with the nanoDots embedded in the plastic at different locations. They are covered in tape so they do not fall out when the layer is placed back on the main body of the phantom in the background of the picture.

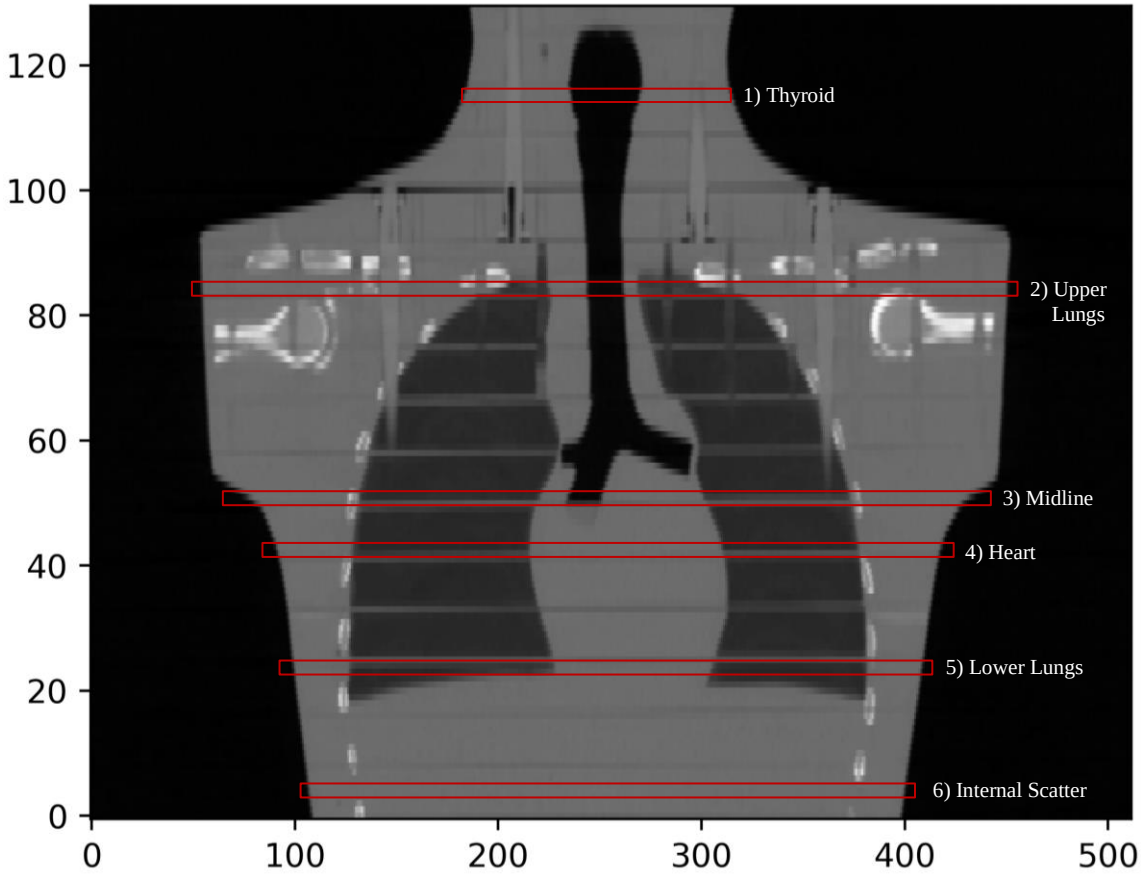

Figure 53. The coronal plane of the CT zoomed in on the lung region. The red boxes show the axial locations where dosimeters are located. Each numbered box corresponds to the axial image showing the dosimeters' depth in the following figures.

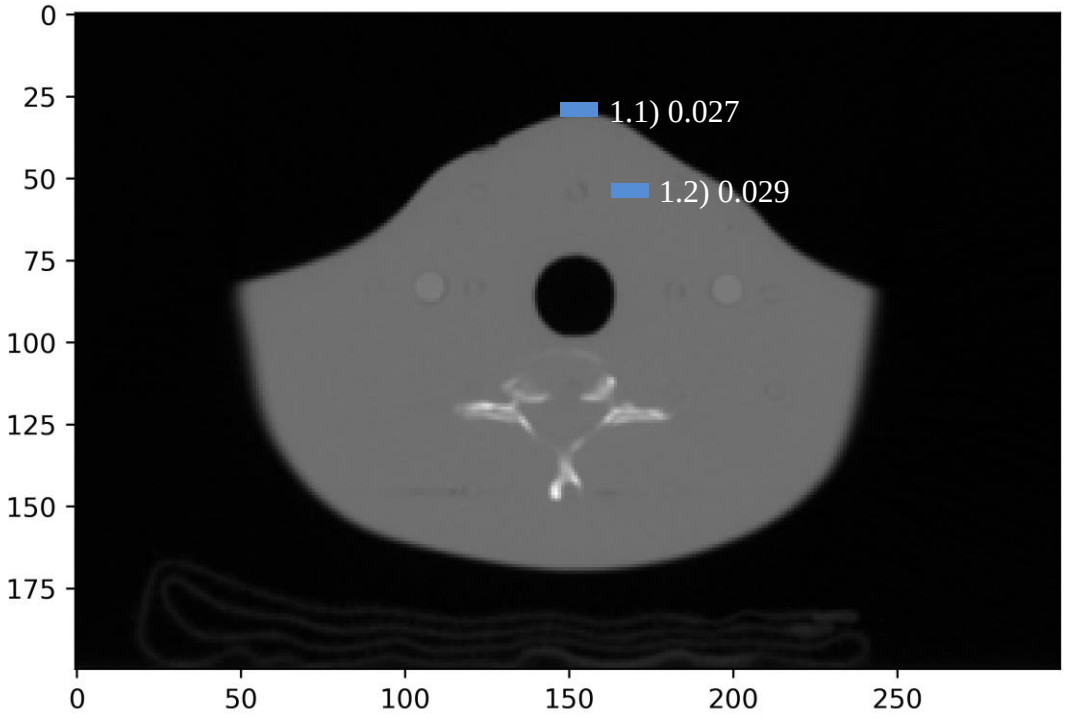

Figure 54. The axial image of the 1st box of image Figure 53 corresponds to the thyroid location. The dosimeter locations in blue represent the surface skin dose on the trachea and the dose to the thyroid. The number represents the dosimeter ID in Table 4 and the dose rates in cGy/s

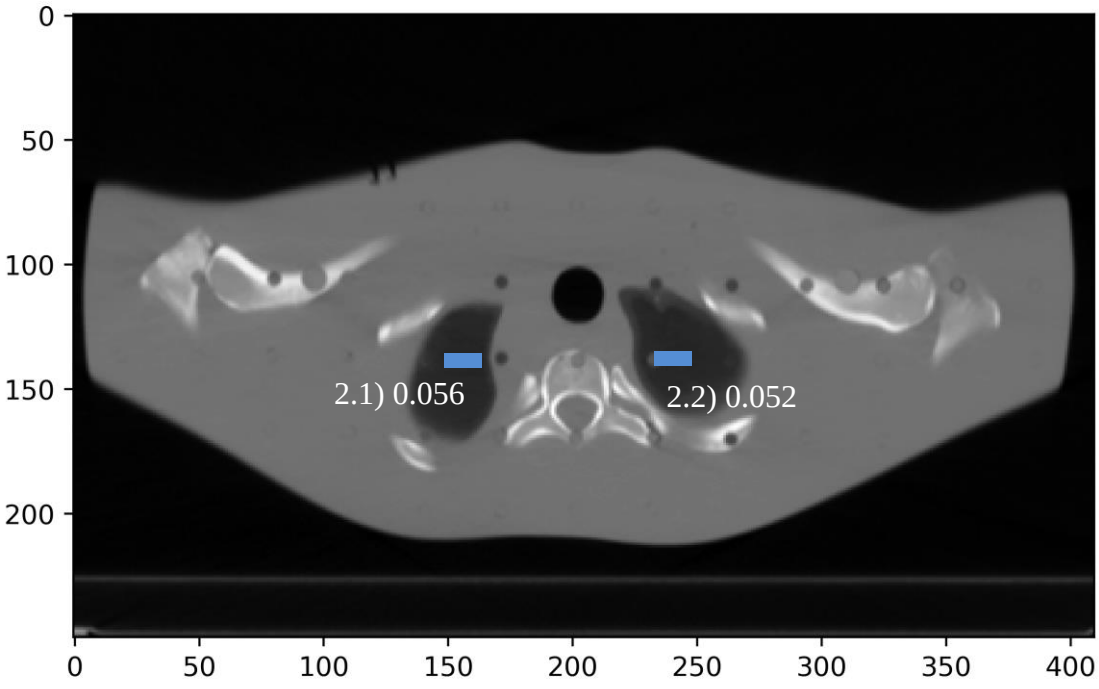

Figure 55. This axial projection corresponds to the region labeled 2) upper lungs in Figure 53. The value beside the label is the dose rate in cGy/s.

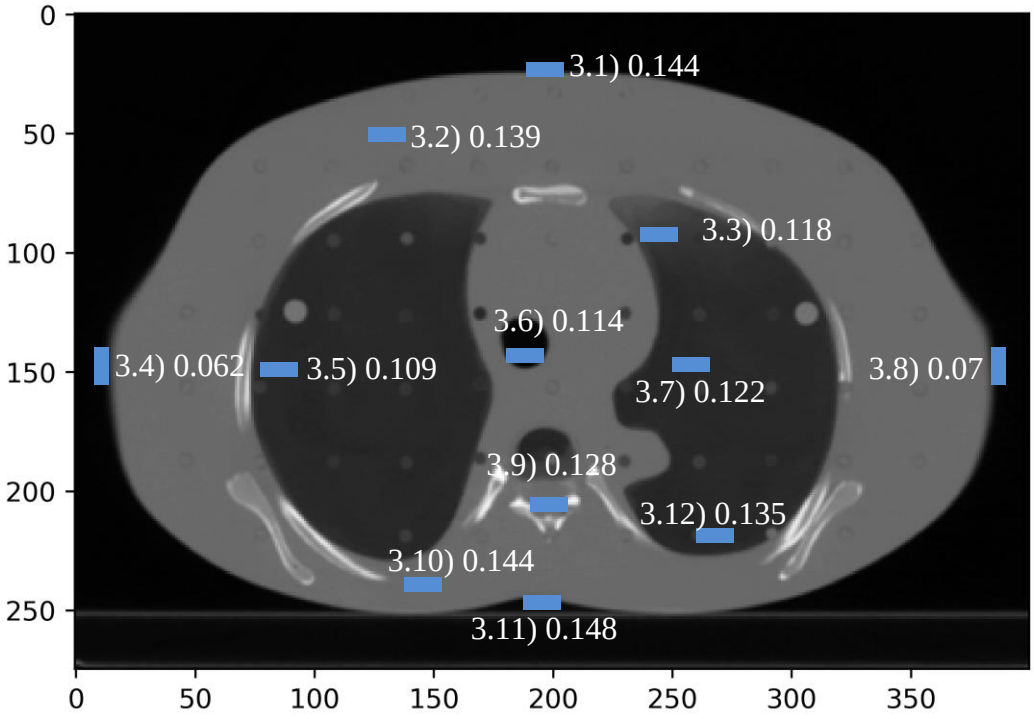

Figure 56. This image shows an axial view of the region labeled 3) Midline in Figure 53. This region is in the middle of the lungs and contains an isocenter. The value beside the label is the dose rate in cGy/s.

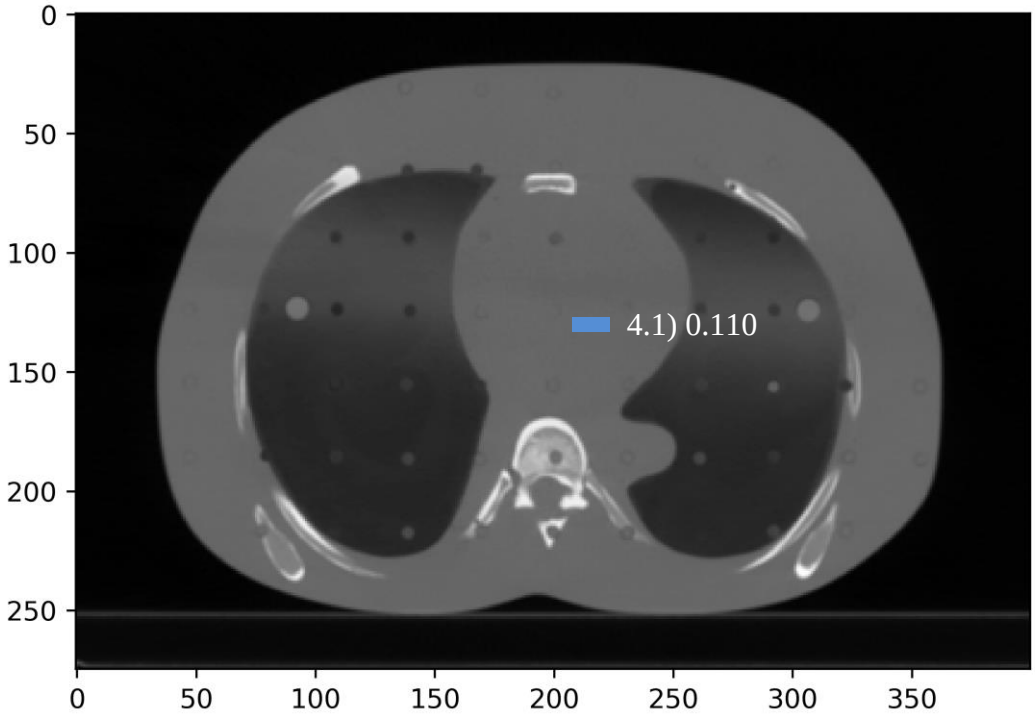

Figure 57. This image shows an axial image of the region labeled 4) Heart in Figure 53. The value beside the label is the dose rate in cGy/s.

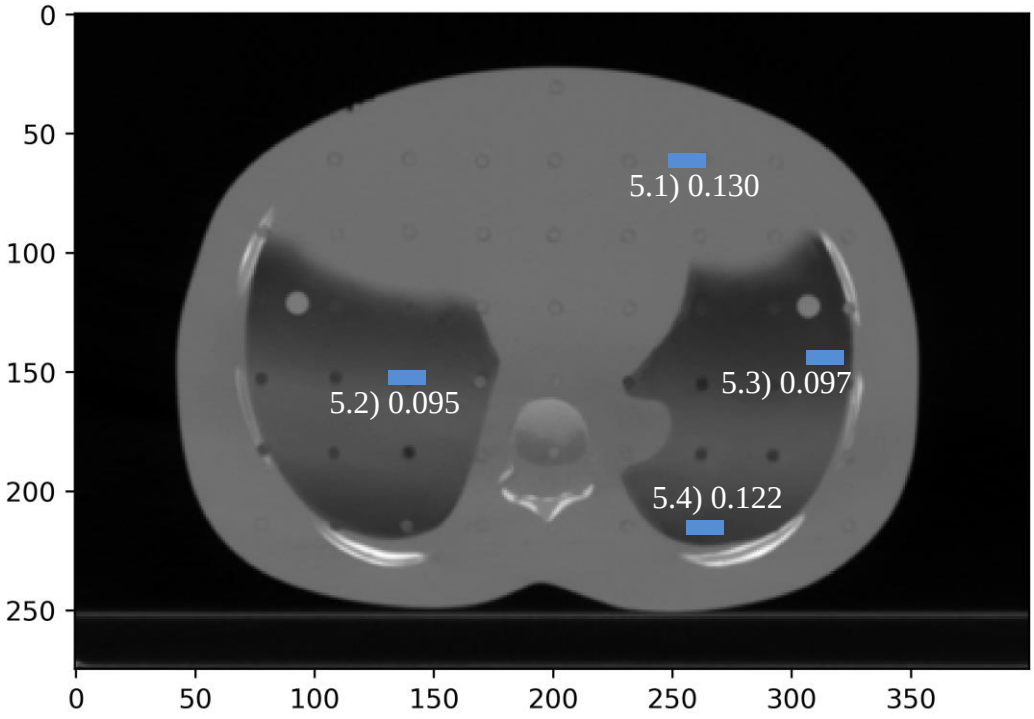

Figure 58. This image shows an axial image in the region labeled 5) Lower Lungs in Figure 53. The value beside the label is the dose rate in cGy/s.

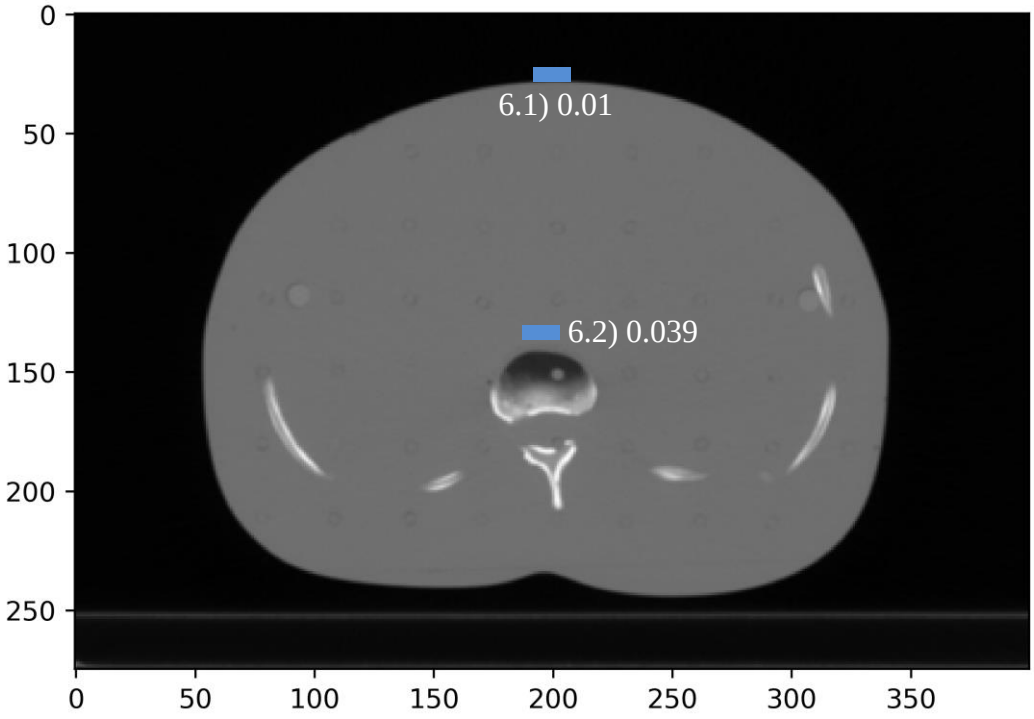

Figure 59. This image shows an axial projection of the region labeled 6) Internal Scatter in Figure 53. The value beside the label is the dose rate in cGy/s.

The isocenter identified from the imaging conducted in Chapter Six is marked on the front and back of the phantom, placed inside the X-ray enclosure, and aligned for the AP exposure first. A two-minute exposure is set inside the comet control panel to automatically ramp to 300 kVp @ 3 mA and stop after the set time. The same process is repeated for the PA, exposing it for two more minutes. The two phantom setups are shown in Figure 60. The time of two minutes was chosen arbitrarily to ensure that each nanoDot, even those in the center of the lungs or outside of the field, would receive enough dose to give a reliable reading.

Following the irradiation of the phantom, the nanoDots were carefully removed and sent back to Landauer via overnight mail for reading. Again, the 120 kVp CT calibration standard is chosen for consistency with the nanoDot verification results in Chapter Five. Table 4 has the nanoDot results, serial id number, and a location number corresponding to the previous CT images to understand their location in the body.

7.2 VIP-man Simulations

With the new beam model accurately reproducing the beam heel and other non-uniformities of the X-ray beam, new dose maps are made like those seen in Chapter Three. These are made by inserting the nested cone photon beam into the VIP-man simulation space at 35 cm SSD. A 1 cm thick lead cylinder surrounds the beam source to approximate the X-ray tube head. The new filter made of 1 mm of cadmium, 0.25 mm of copper, and 1 mm of aluminum is modeled, covering the beam opening of the lead cylinder. As discovered in Chapter Three, a two-field AP-PA setup is required to provide the best coverage of the lung tissue and limit the entrance dose. This is done in two simulations, with the tube head, filter, and source placed in front and behind the phantom.

Scaling by the conversion factor discussed in Chapter Five, the dose rate in each voxel is reported in cGy/s. The dose map is given a color scale and overlaid onto the approximated CT image, as seen in Figure 61 and Figure 62. Each shows an axial plane of the phantom at the isocenter with the AP and PA beam setups, respectively.

Figure 60. The left image is the AP field setup, and the right image is the PA field setup. The wooden board acts as a spacer to ensure the SSD is 35 cm. The beam's central axis is underneath the blue tape, containing the surface dose nanoDots.

Table 4. Results of the nanoDot exposure with the dose rate reported in cGy/s. The location number corresponds to the numbers in Figure 54 through Figure 59.

Location Number	Serial ID Number	Dose (cGy/s)
Region 1		
1.1	00077-361644	0.027
1.2	00071-36105V	0.029
Region 2		
2.1	00054-37371Q	0.056
2.2	00055-477906	0.052
Region 3		
3.1	00072-36337M	0.144
3.2	00061-36701Q	0.139
3.3	00058-36129K	0.118
3.4	00075-37335M	0.062
3.5	00060-36850L	0.109
3.6	00063-362291	0.114
3.7	00057-489068	0.122
3.8	00074-476891	0.070
3.9	00062-490715	0.128
3.10	00059-37348F	0.144
3.11	00073-42804K	0.148
3.12	00056-489654	0.135
Region 4		
4.1	00064-36122Y	0.110
Region 5		
5.1	00067-476776	0.130
5.2	00065-36522Q	0.095
5.3	00066-37462N	0.097
5.4	00068-37381P	0.122
Region 6		
6.1	00076-36535J	0.010
6.2	00069-477287	0.039

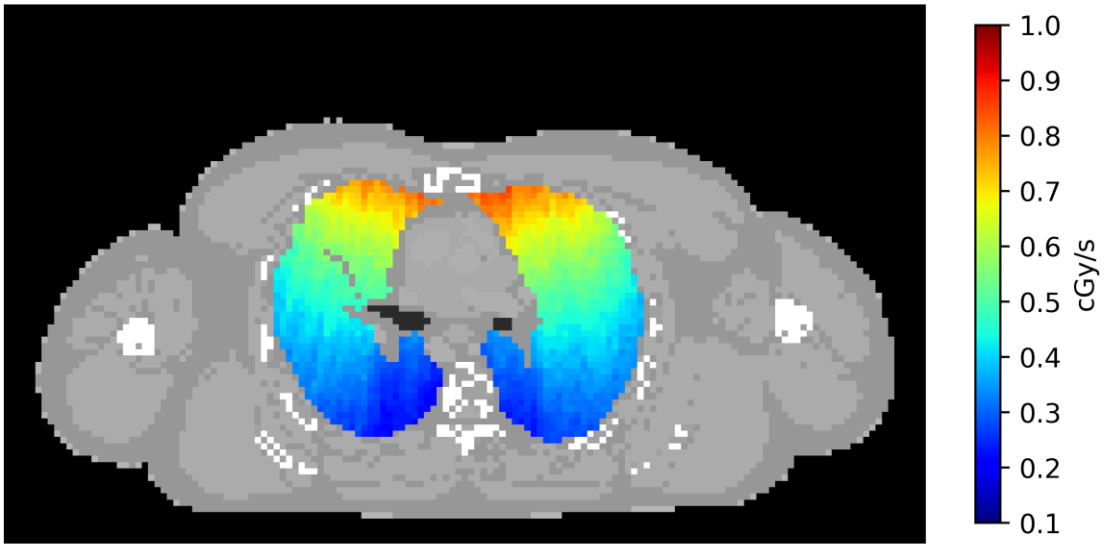

Figure 61. The AP field in the axial plane at the isocenter with the nested cone photon simulation. The dose reduction from the front of the lungs to the back is substantial, ~75%.

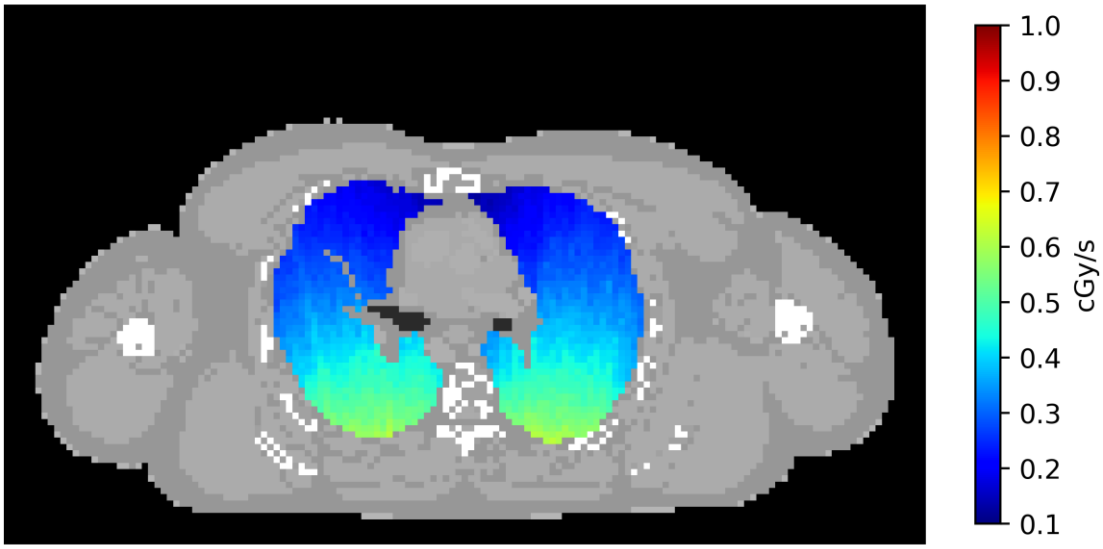

Figure 62. The PA field in the axial plane at the isocenter with the nested cone photon simulation. The dose reduction from the front of the lungs to the back is substantial, ~70%.

Due to the equal beam weighting used in the RSD phantom experiment, the combined fields shown in Figure 63 have equal weighting between the two beams. Figure 64 and Figure 65 are coronal and sagittal plane dose overlays with equal beam weighting between the two fields. The skin and heart doses are tracked for the combined AP-PA overlays to determine the dose to these structures. Unfortunately, the construction method used to build the VIP-man phantom did not cover the entire surface with skin voxels, so the data points are sparse. There were no skin voxels placed on the back. Several skin voxels are on the chest at the centerline, so this region's entrance and exit dose is calculated. Because the SSD for the AP and PA beams are the same and equally weighted, the skin dose rate on the front of the chest can be estimated to be the same for the back.

Figure 63 shows that the dose coverage along the central axis in the axial plane is very uniform. The dose from the front and back of the lungs to the center decreases from 0.46 to 0.40 cGy/s for most of the lungs. This is also represented in Figure 64, showing that the dose rate is fairly uniform at the centerline in the coronal plane. The peripheral of the lungs in the axial and coronal planes are lower at ~0.3 cGy/s due to beam divergence and path length differences through the chest wall and surrounding tissue, further attenuating the beam.

From Figure 65, the sagittal plane shows a decrease in dose towards the top of the lungs from ~0.40 cGy/s at the centerline to ~0.28 cGy/s at the apex. This is due to multiple factors. The first is the difference in path length as a function of $1/r^2$ and attenuation length through the chest wall as described with the peripheral coronal plane. The second reason, and for a larger effect, is the heel of the beam. As described in Chapter Five with the profile measurements, the beam's intensity decreases as the X-ray emission angle becomes closer to parallel with the anode face. This feature is also present in the X-ray images shown in Chapter Six with the line profile plots. The beam's intensity begins to decrease towards the top of the image. In X-ray imaging, this heel effect is leveraged, especially with chest X-rays, to limit the dose to the top of the chest, which is thinner than the bottom of the lungs.

With orthovoltage X-ray treatment, the goal is to deliver as much dose as possible with uniformity; therefore, the heel decreases performance at the top of the lungs.

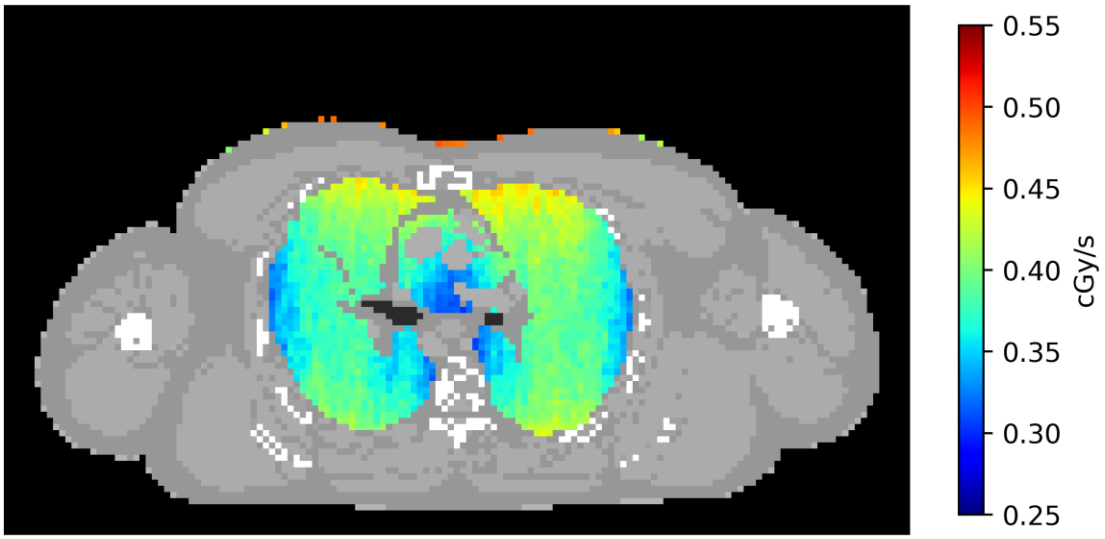

Figure 63. The AP-PA dose fields are equally weighted in the axial plane with the nested cone photon simulation. The dose reduction from the front and back of the lungs to the isocenter is ~13% greatly improving dose coverage. The maximum heart dose is 0.42 cGy/s. The maximum skin dose is ~0.51 cGy/s.

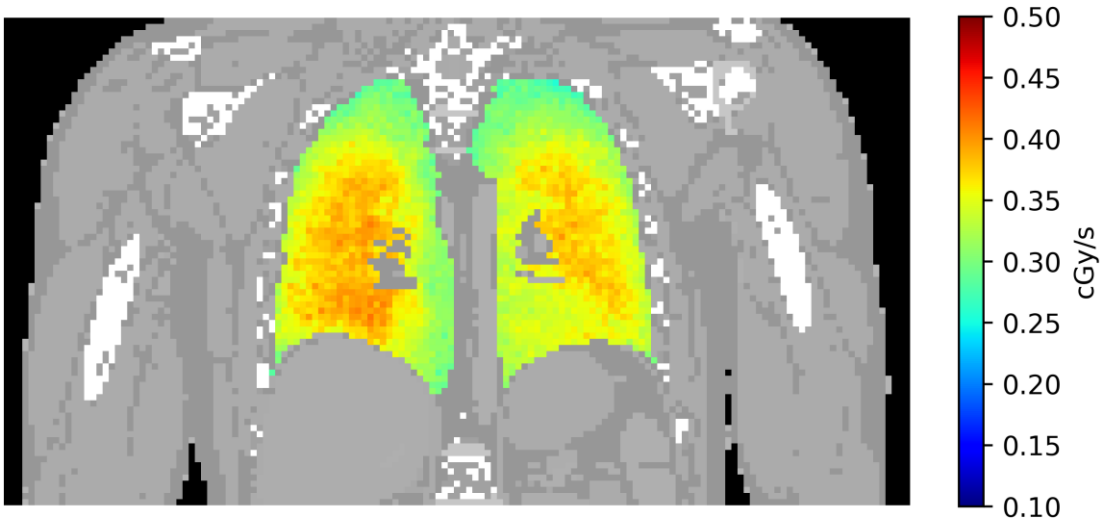

Figure 64. The AP-PA dose fields are equally weighted in the coronal plane at the isocenter. This image shows good coverage to most of the lungs while the dose drops off towards the top of the lungs, around the perimeter, and in the bottom center toward the patient's left due to the heart. The variation in dose is ~41%, with most of the drop-off at the top of the lungs.

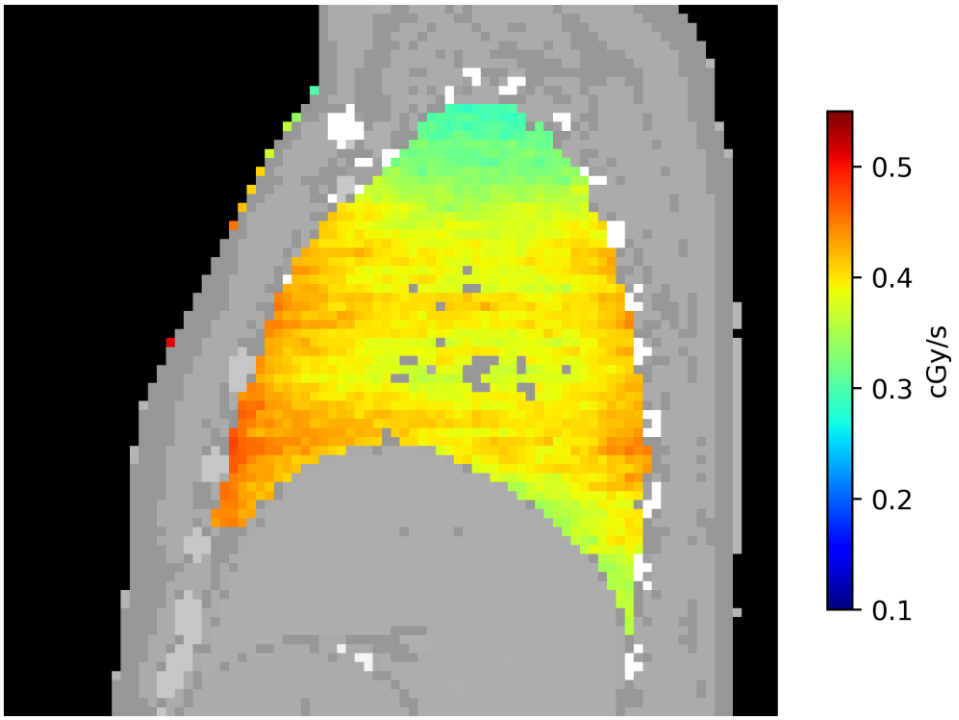

Figure 65. AP-PA dose fields are equally weighted in the sagittal plane, 5.6 cm right of the isocenter, to display most of the right lung. The dose reduction from the isocenter to the top of the lungs is ~41% due to the heel effect. The dose to the bottom back of the lungs is also low due to attenuation through abdominal organs. Notice the increased dose along the paths between ribs.

These simulations show that an AP-PA field setup would reach the prescribed dose at the isocenter of 150 cGy in 357 seconds or about six minutes. This is about the same amount of time described in Chapter Three with the photon cone simulations. Skin dose would reach a maximum of 179 cGy at the beam's central axis on the patient's front and back. It is clear from Figure 65 that the skin dose would decrease at locations away from the central beam axis.

While the photon cone simulation gave similar results, adding the beam heel reducing coverage to the top of the lungs suggests a slight alteration to the beam setup could improve uniformity in this area. Moving the isocenter higher in the lungs may result in better coverage but with an increased dose to the neck and thyroid area while sacrificing coverage of the lower lungs. Additional collimation of the heel, creating a sharper dose fall off, could save the dose to the thyroid, alleviating this issue.

Not shown in these images is the dose to the lateral areas of the field to the left and right of the lungs. Since the lateral collimator opening is 60°, much of the chest wall, arms, and shoulder region are receiving beam. Also, because the width of the lungs at the top is narrower than the bottom, there is excess dose to the upper chest. A custom collimator design that closely contours the lungs laterally would reduce the dose to healthy tissue in these regions.

7.3 Experimental versus Simulated Results

When comparing the nanoDot measurements to the simulation results, the issue of the nanoDot response discussed in Chapter Five makes the direct comparison challenging. The main goal of the nanoDot measurements is to experimentally verify the dose uniformity of the X-ray tube and the filter design used. Importantly, the calibrated dose response of the nanoDots can validate the X-ray tube model to ensure that the model has no serious errors such as output. The discussion in Chapter Six summarizes the steps taken to ensure that the tube model output and profile are modeled correctly and why the nanoDot response is lower than expected.

We found that the dose rate at 35 cm SSD is 4 times lower than the simulation. With this in mind, the nanoDot values in section 7.1 are scaled to this location, represented as a percentage of this point. The dose normalization is overlaid onto the simulated X-ray output in section 7.2. The measured dose cannot be taken as an absolute dose measurement in this case. However, it does allow for the relative dose between each nanoDot location and the simulation results to be compared. Further, since the IC profiler measurements proved the beam model matches, in the unlikely chance the simulation's output is off by some factor, the relative dose between the nanoDots and the simulations would still hold true. In this comparison, inherent differences exist between the RSD phantom and the VIP-man simulation phantom. The RSD phantom has slightly different overall dimensions and material types, with only tissue-equivalent plastic representing skin/muscle/organs, lung-equivalent plastic, and bone-equivalent plastic. VIP-man has much more tissue differentiation leading to more complex X-ray transport through the body.

Figure 66, Figure 67, and Figure 68 are axial, coronal, and sagittal views of the simulated dose maps, as shown in section 7.2. With these images, the dose map is scaled to represent the dose as a percentage of d_{max}, which in the simulation, is the dose scaling point between the bremsstrahlung simulation and nested photon cones simulation at 35cm SSD. The nanoDot results are scaled to the dosimeter at the same location, 35 cm SSD on the front of the chest (nanoDot 3.1).

The comparison between the simulated dose maps and the nanoDot exposure shows good agreement when normalized to d_{max}. The dosimeters along the centerline of the right lung show a relatively flat dose, from 82% at the front, 84% at the middle, and 92% at the back. The dose map results, especially at the middle and back locations, match this distribution closely. The location at the front of the lungs is within 10% of the nanoDot reading. This could be caused by local material deviation and differences between the VIP-man and RSD phantom. The chest wall in the phantom may be slightly thicker than in the simulation. It can also be attributed to the intrinsic error of the nanoDot reading. Other readings, like those at the bottom of the lungs, match the dose map very well, within a few percent.

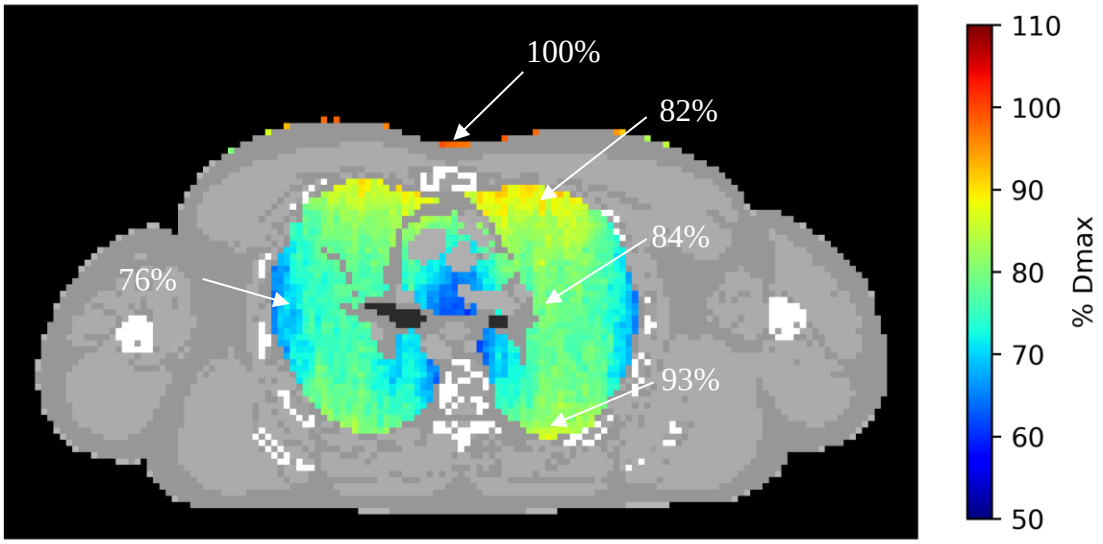

Figure 66. Axial slice at isocenter with the simulated dose map normalized as a percentage of D_{max}, the dose scaling point at 35 cm SSD. The white text and arrows point to the location of nanoDot dosimeters in their approximate location during the experiment. The dosimeter values are normalized to D_{max}, nanoDot 3.1 at 35 cm SSD in the experiment.

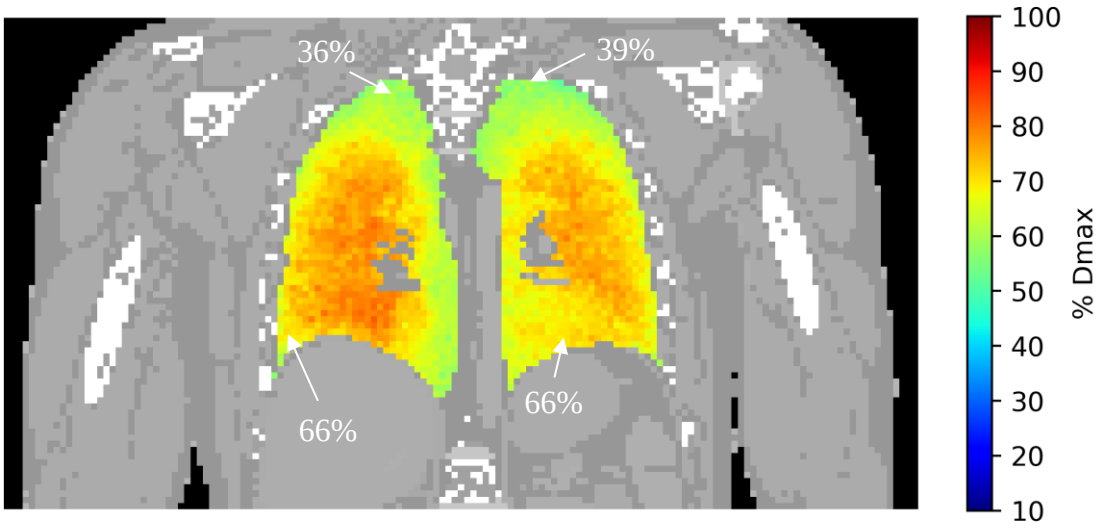

Figure 67. Coronal slice at isocenter with the simulated dose map normalized as a percentage of D_{max}, the dose scaling point at 35 cm SSD. The white text and arrows point to the location of nanoDot dosimeters in their approximate location during the experiment. The dosimeter values are normalized to D_{max}, nanoDot 3.1 at 35 cm SSD in the experiment.

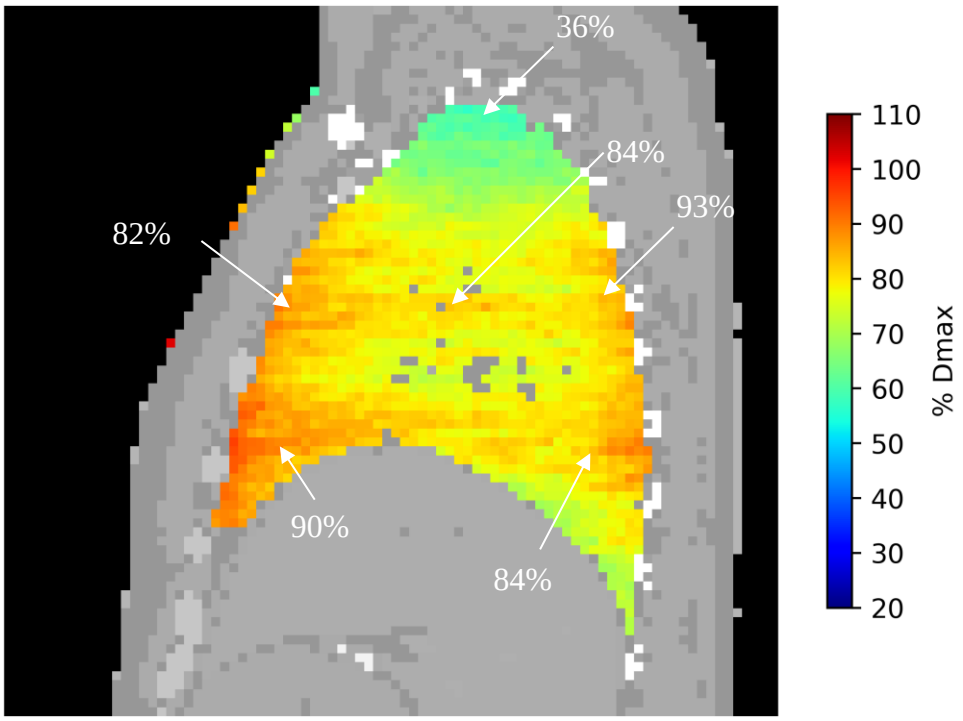

Figure 68. Sagittal slice at 5.6 cm right of isocenter with the simulated dose map normalized as a percentage of D_{max}, the dose scaling point at 35 cm SSD. The white text and arrows point to the location of nanoDot dosimeters in their approximate location during the experiment. The dosimeter values are normalized to D_{max}, nanoDot 3.1 at 35 cm SSD in the experiment.

One location that does not show good agreement between the nanoDot exposure and the dose map is at the top of the lungs. The percent d_{max} of the dose map suggests this region should be ~60%; however, the nanoDot is ~36%. The dosimeter result, roughly half that of the simulation, suggests that the beam heel significantly affects the dose rate in this region. The two-inch shift of isocenter towards the top of the lungs discussed in the imaging study in section 6.2 and in section 7.2 is made so that the heel in this region did not cause this dose drop-off. Evidently, this is not enough, and a greater shift is needed.

It is clear from the dose map and nanoDot overlays that the beam model and experimental results agree in most areas of interest. The upper lung region is affected more than expected with the experimental data, but this is due to a setup error. The different chest wall thicknesses and the position of bones between the VIP-man simulation and the RSD phantom can explain other deviations, like the dose rate at the front of the lungs.

CHAPTER EIGHT
CONCLUSIONS

8.1 Results Achieved

Intending to treat ARDS-type illness with LD-RT, this work provides both computation and experimental results proving the viability of such a system. MCNP-based models have shown that a 300 kVp @ 3 mA X-ray tube can deliver the prescribed dose of 1.5 Gy to the lung isocenter. Including a multilayer filter has been shown to harden the beam, increasing the average X-ray energy to approximately 150 keV and improving the dose uniformity with depth. The dose uniformity with depth is improved by utilizing a two-field setup, AP-PA, at 35 cm SSD. This results in a central lung dose of ~80% D_{max} at the skin surface. With the current model and X-ray tube, the treatment time to deliver 1.5 Gy at the isocenter is ~6 minutes with 3 mA of tube current.

Dose overlays with the VIP-man phantom suggest the peak skin dose at the central beam axis does not exceed 1.8 Gy, and with the short SSD, the $1/r^2$ dependence reduces this towards the beam edge. The distribution in the coronal and sagittal planes also suggests good dose coverage in these dimensions. According to the model, care must be taken to properly align the heel of the beam to avoid an area of low dose at the top of the chest.

A testing enclosure was built to validate the beam models and perform actual dosimetry, given the predicted performance of the X-ray tube. NCRP and MCNP calculations determined the necessary shielding to operate the COMET EVO 300D X-ray tube safely. Modification of an existing radiation cabinet was performed to save time and total effort. Adding 1/4 to 3/8 in. of lead to the cabinet reduced the exposure rate to the public below the necessary design limits. These modifications allowed for testing the X-ray tube and data collection of many beam parameters. This enclosure also allowed for dosimetry verification of the treatment protocol with an RSD human phantom.

Experimental results with nanoDot dosimeters embedded in the RSD phantom show that dose coverage and uniformity match the simulations. With the same filter, SSD,

and two-field weighting, the isocenter dose rate was experimentally measured to be ~80 % of D_{max}, the surface of the phantom. Imaging of the phantom, which aided in the alignment of the X-ray field, suggests that the beam heel resulted in the same under-dosing at the top of the lungs as predicted with the MCNP model. This result further verifies that the beam model is correct and can accurately model results that are repeatable in experimentation.

8.2 Future Work

Following this initial proof of concept, the next step would be incorporating CT scan data into the MCNP model space. The VIP-man phantom is developed for general human dosimetry but is not specific to any individual patient or phantom. Further studies can be conducted with more patient variation by developing a program that can convert CT voxel data to a voxelated phantom, similar to VIP-man. Conversion of CT scan data into MCNP would also allow for the RSD phantom to be used in simulation to model the expected dose rate at each detector accurately. Using real CT data would also allow for improved simulation times by limiting the simulation space to the chest region.

Further studies involving preclinical or clinical research with LD-RT for ARDS-type illness would determine the dose necessary to induce the desired clinical response. This study used a dose of 1.5 Gy to the isocenter of the lungs; however, it is possible that lower dose could achieve the same outcome. Clinical data would further guide the development of the X-ray system by quantifying the dose uniformity necessary for treatment.

The lack of a calibrated dosimetry standard for a 300 kVp orthovoltage tube means that the X-ray output has not been directly measured. Developing a calibrated dosimetry standard and verifying the true dose rate with the X-ray tube is vital for accurate dose calculations. While this study provided relative measurements with the nanoDots, a true calibrated dose rate must be calculated. To account for tube output changes, this calibration standard must be reproducible to verify the dose rate across time. The calibrated output is also vital for patient treatment, where the dose rate and dose delivered must be known with small margins for error to prevent over or under-dosing the patient.

Collimator and filter designs can be improved or customized to different setups and patient sizes depending on either X-ray imaging or CT scan data. This can limit the total dose for areas outside the lungs and protect organs out of the field. Non-homogeneous filters with variable thickness can also be investigated to increase or decrease X-ray transmission to different chest regions. This can change the dose profile, shifting the dose and coverage to different areas of the lungs.

Finally, developing a dose computation algorithm that does not rely on MCNP or other Monte Carlo simulations can improve treatment planning times. Utilizing analytical calculations with radiographs or CT scan data can drastically reduce the time and effort involved in developing a treatment per individual. This is the standard treatment planning method in radio-oncology and would also greatly benefit low-dose treatment planning.

LIST OF REFERENCES

1. Gianfaldoni, S., et al., *An Overview on Radiotherapy: From Its History to Its Current Applications in Dermatology.* Open Access Maced J Med Sci, 2017. **5**(4): p. 521-525.
2. Hess, C.B., et al., *Low-Dose Whole-Lung Radiation for COVID-19 Pneumonia: Planned Day-7 Interim Analysis of an Ongoing Clinical Trial*. medRxiv, 2020: p. 2020.06.03.20116988.
3. Hess, C.B., et al., *Immunomodulatory Low-Dose Whole-Lung Radiation for Patients with Coronavirus Disease 2019-Related Pneumonia.* Int J Radiat Oncol Biol Phys, 2021. **109**(4): p. 867-879.
4. Lara, P.C., J. Burgos, and D. Macias, *Low dose lung radiotherapy for COVID-19 pneumonia. The rationale for a cost-effective anti-inflammatory treatment.* Clinical and Translational Radiation Oncology, 2020. **23**: p. 27-29.
5. Matthay, M.A., L.B. Ware, and G.A. Zimmerman, *The acute respiratory distress syndrome.* The Journal of Clinical Investigation, 2012. **122**(8): p. 2731-2740.
6. Assmus, A., *Early history of X rays.* Beam Line, 1995. **25**(2): p. 10-24.
7. Grubbé, E.H., *Priority in the therapeutic use of X-rays.* Radiology, 1933. **21**(2): p. 156-162.
8. Becquerel, H. and P. Curie, *Action physiologique des rayons du radium.* Compt. Rend. Acad. Sci, 1901. **132**: p. 1289-1291.
9. Musser, J. and D. Edsall, *A study of metabolism in leukaemia, under the influence of the x-ray.* Tr A Am Physicians, 1905. **20**: p. 294-323.
10. Quimby, A.J. and W.A. Quimby, *Unresolved pneumonia: successful treatment by Röngen Ray*. 1916: AR Elliott.
11. Lawrence, E.O. and M.S. Livingston, *The production of high speed light ions without the use of high voltages.* Physical Review, 1932. **40**(1): p. 19.
12. Heidenhain, L. and C. Fried, *Röntgenstrahlen und Entzündung.* Klinische Wochenschrift, 1924. **3**(25): p. 1121-1122.
13. Calabrese, E.J. and G. Dhawan, *How radiotherapy was historically used to treat pneumonia: could it be useful today?* Yale J Biol Med, 2013. **86**(4): p. 555-70.
14. Muller, H.J., *The production of mutations by X-rays.* Proceedings of the National Academy of Sciences, 1928. **14**(9): p. 714-726.
15. Coutard, H., *Principles of x ray therapy of malignant diseases.* The lancet, 1934. **224**(5784): p. 1-8.
16. Tsien, K. and R. Robbins, *A Comparison of a Cobalt-60 Teletherapy Unit and a 2-MEV Van de Graaff X-ray Generator on the Basis of Physical Measurements.* Radiology, 1958. **70**(4): p. 486-502.
17. Pereira, G.C., M. Traughber, and R.F. Muzic, Jr., *The role of imaging in radiation therapy planning: past, present, and future.* Biomed Res Int, 2014. **2014**: p. 231090.
18. Van Dyk, J., J.J. Battista, and P. Almond, *A retrospective of Cobalt-60 radiation therapy:"The atom bomb that saves lives".* Med. Phys Int J, 2020. **4**.

19. Thwaites, D.I. and J.B. Tuohy, *Back to the future: the history and development of the clinical linear accelerator.* Physics in medicine & biology, 2006. **51**(13): p. R343-R362.
20. Martins, P.N., *A brief history about radiotherapy.* International Journal of Latest Research in Engineering and Technology (IJLRET), 2018. **4**: p. 08-11.
21. Do Huh, H. and S. Kim, *History of radiation therapy technology.* Progress in Medical Physics, 2020. **31**(3): p. 124-134.
22. Thompson, B.T., R.C. Chambers, and K.D. Liu, *Acute Respiratory Distress Syndrome.* New England Journal of Medicine, 2017. **377**(6): p. 562-572.
23. Bellani, G., et al., *Epidemiology, Patterns of Care, and Mortality for Patients With Acute Respiratory Distress Syndrome in Intensive Care Units in 50 Countries.* JAMA, 2016. **315**(8): p. 788-800.
24. Auld, S.C., et al., *ICU and Ventilator Mortality Among Critically Ill Adults With Coronavirus Disease 2019.* Crit Care Med, 2020. **48**(9): p. e799-e804.
25. Calabrese, E.J., et al., *Nrf2 activation putatively mediates clinical benefits of low-dose radiotherapy in COVID-19 pneumonia and acute respiratory distress syndrome (ARDS): Novel mechanistic considerations.* Radiotherapy and Oncology, 2021. **160**: p. 125-131.
26. Ameri, A., et al., *Low-Dose Whole-Lung Irradiation for COVID-19 Pneumonia: Short Course Results.* Int J Radiat Oncol Biol Phys, 2020. **108**(5): p. 1134-1139.
27. Sanmamed, N., et al., *Low-Dose Radiation Therapy in the Management of Coronavirus Disease 2019 (COVID-19) Pneumonia (LOWRAD-Cov19): Preliminary Report.* Int J Radiat Oncol Biol Phys, 2021. **109**(4): p. 880-885.
28. Meziani, L., et al., *Low Doses of Radiation Increase the Immunosuppressive Profile of Lung Macrophages During Viral Infection and Pneumonia.* International Journal of Radiation Oncology*Biology*Physics, 2021. **110**(5): p. 1283-1294.
29. Thwaites, D.I. and J.B. Tuohy, *Back to the future: the history and development of the clinical linear accelerator.* Physics in Medicine & Biology, 2006. **51**(13): p. R343.
30. Molina, J.R., et al., *Non-Small Cell Lung Cancer: Epidemiology, Risk Factors, Treatment, and Survivorship.* Mayo Clinic Proceedings, 2008. **83**(5): p. 584-594.
31. Sale, C. and P. Moloney, *Dose comparisons for conformal, IMRT and VMAT prostate plans.* Journal of Medical Imaging and Radiation Oncology, 2011. **55**(6): p. 611-621.
32. Ballas, L.K., et al., *Radiation therapy facilities in the United States.* Int J Radiat Oncol Biol Phys, 2006. **66**(4): p. 1204-11.
33. Dracham, C.B., A. Shankar, and R. Madan, *Radiation induced secondary malignancies: a review article.* Radiat Oncol J, 2018. **36**(2): p. 85-94.
34. Armstrong, G.T., et al., *Late mortality among 5-year survivors of childhood cancer: a summary from the Childhood Cancer Survivor Study.* J Clin Oncol, 2009. **27**(14): p. 2328-38.
35. Berrington de Gonzalez, A., et al., *Second Solid Cancers After Radiation Therapy: A Systematic Review of the Epidemiologic Studies of the Radiation*

Dose-Response Relationship. International Journal of Radiation Oncology*Biology*Physics, 2013. **86**(2): p. 224-233.
36. Boice Jr, J.D., et al., *Introduction to the special issue on the US Million Person Study of health effects from low-level exposure to radiation.* International journal of radiation biology, 2022. **98**(4): p. 529-532.
37. Boice Jr, J.D. and L.T. Dauer, *Million Person Study of Low-Dose Radiation Health Effects.* Nuclear Science and Engineering, 2022.
38. Nrc. *Gray (Gy)*. 2022 [cited 2022 11/10]; Available from: https://www.nrc.gov/reading-rm/basic-ref/glossary/gray-gy.html.
39. Einstein, A., *The photoelectric effect.* Ann. Phys, 1905. **17**(132): p. 4.
40. jfk. *II X-rays for Diagnosis*. 1995 [cited 2022 10/7]; Available from: http://img.chem.ucl.ac.uk/www/kelly/medicalxrays.htm.
41. Britannica, T.E.o.E., *"Compton effect"*, in *Encyclopedia Britannica*. 2022, @britannica.
42. Sia, J., et al., *Molecular Mechanisms of Radiation-Induced Cancer Cell Death: A Primer.* Frontiers in Cell and Developmental Biology, 2020. **8**.
43. Borek, C., *Antioxidants and Radiation Therapy.* The Journal of Nutrition, 2004. **134**(11): p. 3207S-3209S.
44. Hubbell, J.H., *Photon mass attenuation and energy-absorption coefficients.* The International Journal of Applied Radiation and Isotopes, 1982. **33**(11): p. 1269-1290.
45. *NIST: X-Ray Mass Attenuation Coefficients - Water, Liquid*. 2022 [cited 2022 10/3]; Available from: https://physics.nist.gov/PhysRefData/XrayMassCoef/ComTab/water.html.
46. Nadrljanski, M.M., *X-ray tube | Radiology Reference Article | Radiopaedia.org.* 2022.
47. McCollough, C.H., *The AAPM/RSNA physics tutorial for residents. X-ray production.* RadioGraphics, 1997. **17**(4): p. 967-984.
48. Hahn, C., et al., *First observation of signals due to KAERI's 10 MeV electron beam by using GEM detectors.* Journal of The Korean Physical Society - J KOREAN PHYS SOC, 2007. **50**.
49. Omar, A., P. Andreo, and G. Poludniowski, *A model for the energy and angular distribution of x rays emitted from an x-ray tube. Part I. Bremsstrahlung production.* Medical Physics, 2020. **47**(10): p. 4763-4774.
50. *Bremsstrahlung Radiation - PhysicsOpenLab.* 2022.
51. *X-ray_tube*. 2022 [cited 2022 11/14]; Available from: https://www.bionity.com/en/encyclopedia/X-ray_tube.html.
52. Allard, D., *WE-H-204-01: William D. Coolidge, Inventor of the Modern X-Ray Tube.* Medical Physics, 2016. **43**(6Part42): p. 3838-3839.
53. Shaik, A. *Thermionic emission*. 2022; Available from: https://www.physics-and-radio-electronics.com/electronic-devices-and-circuits/electron-emission/thermionicemission.html.

54. Rana, N., et al., *Evaluation of external beam hardening filters on image quality of computed tomography and single photon emission computed tomography/computed tomography.* J Med Phys, 2015. **40**(4): p. 198-206.
55. Trout, E., J. Kelley, and A. Lucas, *Evaluation of Thoraeus filters.* The American journal of roentgenology, radium therapy, and nuclear medicine, 1961. **85**: p. 933-939.
56. Ahnesjö, A., M. Saxner, and A. Trepp, *A pencil beam model for photon dose calculation.* Medical Physics, 1992. **19**(2): p. 263-273.
57. Starkschall, G., et al., *Beam-commissioning methodology for a three-dimensional convolution/superposition photon dose algorithm.* Journal of Applied Clinical Medical Physics, 2000. **1**(1): p. 8-27.
58. Ahnesjö, A. and M.M. Aspradakis, *Dose calculations for external photon beams in radiotherapy.* Phys Med Biol, 1999. **44**(11): p. R99-155.
59. Reynaert, N., et al., *Monte Carlo treatment planning for photon and electron beams.* Radiation Physics and Chemistry, 2007. **76**(4): p. 643-686.
60. Rogers, D. and A. Bielajew, *Monte Carlo techniques of electron and photon transport for radiation dosimetry.* The dosimetry of ionizing radiation, 1990. **3**: p. 427-539.
61. Shultis, J.K. and R.E. Faw, *An MCNP primer*. 2011.
62. Xu, X.G., T.C. Chao, and A. Bozkurt, *VIP-MAN: AN IMAGE-BASED WHOLE-BODY ADULT MALE MODEL CONSTRUCTED FROM COLOR PHOTOGRAPHS OF THE VISIBLE HUMAN PROJECT FOR MULTI-PARTICLE MONTE CARLO CALCULATIONS.* Health Physics, 2000. **78**(5).
63. Berger, M.J., *ESTAR, PSTAR, and ASTAR: Computer programs for calculating stopping-power and range tables for electrons, protons, and helium ions.* 1992.
64. Schneider, U., E. Pedroni, and A. Lomax, *The calibration of CT Hounsfield units for radiotherapy treatment planning.* Physics in Medicine & Biology, 1996. **41**(1): p. 111.
65. Kase, K.R., *Radiation protection principles of NCRP*. Health physics, 2004. **87**(3): p. 251-257.
66. NCRP, *Report 49 Structural Shielding Design and Evaluation for Medical Use of X-rays and Gamma Rays of Energies Up to 10 MeV: Recommendations of the National Council on Radiation Protection and Measurements*. 1976.
67. *NCRP Report 151 Structural shielding design and evaluation for megavoltage x- and gamma-ray radiotherapy facilities*. 2006.
68. NCRP, *Structural shielding design for medical x-ray imaging facilities*. 2004: NCRP.
69. OncologyMedicalPhysics. *Linear Accelerator Basics | Oncology Medical Physics*. 2022; Available from: https://oncologymedicalphysics.com/introduction-to-clinical-linear-accelerators/.
70. Leal, A., et al., *MLC leaf width impact on the clinical dose distribution: a Monte Carlo approach.* International Journal of Radiation Oncology*Biology*Physics, 2004. **59**(5): p. 1548-1559.

71. Sterzing, F., et al., *Image-guided radiotherapy: a new dimension in radiation oncology.* Dtsch Arztebl Int, 2011. **108**(16): p. 274-80.

APPENDIX

Linac Operational Features

Modern linacs use the same principles as X-ray tubes, accelerating electrons into a high-Z target to produce bremsstrahlung radiation. However, linacs use a different method of accelerating electrons to reach much higher energies. They are heavily optimized for cancer therapy and tumor coverage at various depths, which is why high energies are an important feature of their design. They are much more complex devices; therefore, this section only discusses the key differences in their design.

Linacs use a different method of electron acceleration involving microwave resonances. By using a klystron or magnetron, high-frequency electromagnetic waves (microwaves) are produced [69]. These microwaves are then directed into a waveguide, a metal tube with many chambers for the microwaves to resonate. Electrons are introduced into this tube by an electron gun which uses thermionic emission, like in the X-ray tube, to produce free electrons. The electrons "ride" these resonance waves inside the waveguide to accelerate to very high speeds, anywhere from 2-18 MeV, depending on the design. They then strike a dense high-Z target to produce bremsstrahlung radiation like an X-ray tube. However, linacs are designed to have their X-ray beam port in line with the electron beam to take advantage of the hugely forward-directed radiation in the MeV energy ranges [48, 69]. This design requires multiple target thicknesses for different energies, complex cooling systems, and electron beam steering to ensure proper output. Today, complex multi-leaf collimators are used to manipulate the X-ray beam to nearly any shape imaginable for the purposes of target tissue coverage [70]. One other feature not present with X-ray tubes is the ability to remove the X-ray target and allow the electron beam to be used for treatment.

With multileaf collimator (MLC) leaves and the ability to adapt the X-ray output in real-time, advanced forms of treatment are possible such as IMRT and VMAT [31]. Advanced algorithms can modulate the MLC configuration and beam output to create highly conformal dose distributions around the target structures. With the addition of

IGRT, onboard imaging can track specified locations to automatically gate the beam output [71]. These specialized features have made linacs effective at delivering high-dose rate therapy to precise locations inside the body.

VITA

Thomas “Heath” Davis was born in Asheville, North Carolina, on February 1st, 1998. They graduated from North Buncombe High School with honors in May 2016. The following August, they entered The University of Tennessee and, in 2020, received a Bachelor of Science in Nuclear Engineering. They stayed at the University of Tennessee to pursue a Master of Science Degree in Medical Physics in December 2022. In the spring of 2023, he earned his Doctor of Philosophy in nuclear engineering at the University of Tennessee.